Schweizerische Eidgenossenschaft
Confédération suisse
Confederazione Svizzera
Confederaziun svizra

Federal Department of the Environment, Transport, Energy and Communications DETEC

Swiss Federal Office of Energy SFOE
Energy Research and Cleantech Division

Final report dated 29 February 2024

High-pressure biogas methanation kinetics for energy conversion processes

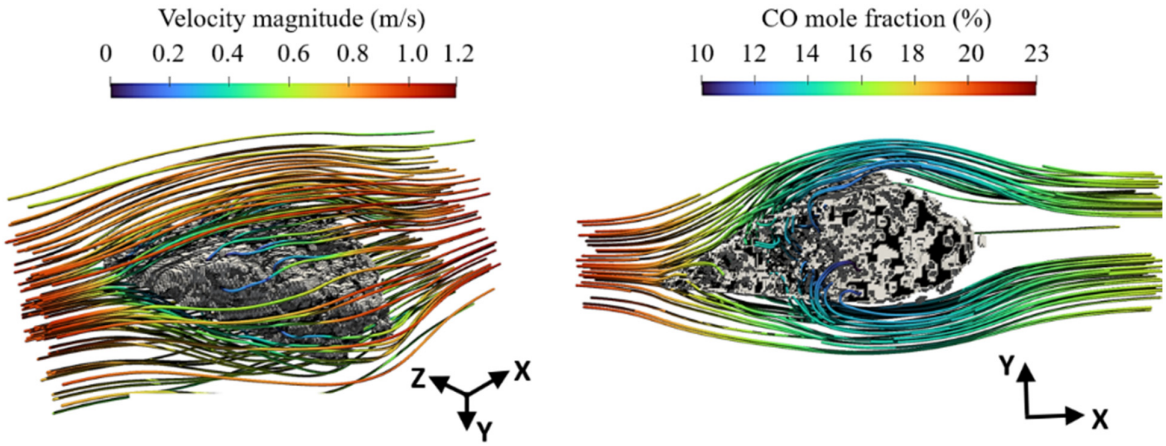

Methanation simulations of a real catalytic Ni/Al_2O_3 particle

Source: ©XY 2024

Date: 29 February 2024

Location: Bern

Publisher:
Swiss Federal Office of Energy SFOE
Energy Research and Cleantech
CH-3003 Bern
www.bfe.admin.ch

Co-financing:
-

Subsidy recipients:
Paul Scherrer Institute
Forschungsstrasse 111
5232 Villigen PSI

Authors:
Ioannis Mantzaras, ioannis.mantzaras@psi.ch
Meysam Khatoonabadi, seyyed-meysam.khatoonabadi@psi.ch
Tilman J. Schildhauer, tilman.schildhauer@psi.ch
Andreas Gantenbein, andreas.gantenbein@psi.ch

SFOE project coordinators:
Dr. Sandra Hermle, sandra.hermle@bfe.admin.ch

SFOE contract number: SI/501976-01

Zusammenfassung

Die Hauptarbeit des Projekts umfasste eine kombinierte experimentelle und numerische Untersuchung mit dem Ziel, In-situ-Methanisierungsexperimente durchzuführen und durch geeignete Vergleiche mit Simulationen die Kinetik der katalytischen Methanisierung bei Drücken bis zu 10 bar zu extrahieren. Für die Methanisierungsexperimente wurde der optisch zugängliche Versuchsstand am PSI umgebaut. Mittels einer angepassten Methode FeCr-Legierungsplatten wurden mit Ni/Al_2O_3-Katalysator beschichtet. Nach erfolgreicher Beschichtung wurden anschließend In-situ-Messungen der CO_2-Methanisierung durchgeführt, einschließlich Gaschromatographie und Raman-Messungen der Konzentrationen der wichtigsten Gasphasenspezies im Querschnitt des katalytischen Kanal. Insgesamt wurden 15 Versuchspunkte mit Variation des H_2:CO_2-Verhältnisses (6, 5 und 4) und des Drucks (1.5, 3, 5, 8 und 10 bar) analysiert.

Alle Methanisierungsfälle wurden mit einem proprietären Code simuliert. Zunächst wurde ein detaillierter Literaturmechanismus verwendet und dann skaliert, um bei hohen Drücken eine gute Übereinstimmung zu erzielen. Anschließend wurde ein am PSI entwickelter zweistufiger Methanisierungsmechanismus für Atmosphärendruck erweitert, um gute Vorhersagen bei Drücken bis zu 10 bar zu ermöglichen. Abschließend wurde ein theoretischer Vergleich der CO_2-Methanisierung auf Rh und Ni durchgeführt; dieser zeigte die Überlegenheit von Ni-Katalysatoren.

Außerdem wurde eine numerische Arbeit im Zusammenhang mit einem SNF-Begleitprojekt zur Entwicklung eines partikelaufgelösten Lattice-Boltzmann-Modells (LB) für die Biogasmethanisierung durchgeführt. Darin wurden hochpräzise Simulationen mit einem LB-Solver durchgeführt, um die Konvektions-Diffusions-Reaktionsprozesse innerhalb und um katalytische poröse Partikel herum zu untersuchen, die in Methanisierungswirbelschichten verwendet werden. Es wurde ein neues katalytisches Modell entwickelt, das für beliebige Damköhler-Zahlen, für äquimolare oder stark nicht-äquimolare Reaktionen und unter Einbeziehung von Geschwindigkeits- und Konzentrationssprüngen (endliche Knudsen-Zahl-Effekt) gültig ist. Anschließend wurde das Modell auf einen realen porösen Partikel angewendet, dessen Geometrie anhand der Röntgentomographiebilder rekonstruiert wurde. Die Geometrie der porösen Partikel und die numerischen Simulationen zeigten, dass die Porenverteilung im Gegensatz zu der in hochskalierten Modellen üblichen Annahme nicht räumlich homogen ist. Abschließend wurden Simulationen an sphärischen porösen Partikeln mit einer künstlichen Makropore durchgeführt, um den Einfluss der räumlichen Porositätsinhomogenität und der Damköhler-Zahl zu bewerten. Es zeigte sich, dass der Einfluss der äußeren Oberfläche des Partikels nicht vernachlässigbar war und die Variation der Spezies um das Partikel herum nicht symmetrisch war, selbst wenn das katalytische Partikel kugelförmig war.

Wichtige Schritte in der Weiterentwicklung der Wirbelschichtmethanisierung und beim Technologietransfer in die Industrie wurden erreicht. Die GanyMeth-Pilotanlage (TRL 6) wurde erfolgreich für reaktive Experimente mit bis zu 200 kW eingesetzt und bestätigte die Ergebnisse der TRL 4/5-Anlage, d. h. die Technologie ist sicher skalierbar. Im Rahmen des EU-Projekts HyFuelUp wird der Industriepartner AlphaSYNT mit Hilfe von PSI eine 500-kW-Methanisierungseinheit entwerfen und bauen, die in einen TRL-7-Demonstrator in Portugal integriert werden soll. Diese deckt die Wertschöpfungskette von minderwertiger Biomasse über Vergasung, Gasreinigung und Methanisierung ab einschliesslich Verflüssigung zu Bio-LNG für den Schwertransport.

Summary

The main work comprised a combined experimental and numerical investigation, with the goal of carrying out in situ methanation experiments and extracting, via suitable comparisons with simulations, catalytic methanation kinetics at pressures up to 10 bar. The optically accessible test rig at PSI was modified for the methanation experiments. A new method was adapted to coat FeCr-alloy plates with Ni/Al_2O_3 catalyst. After successful coating, in situ measurements of CO_2 methanation were subsequently performed, involving Raman measurements of major gas-phase species concentrations across the catalytic channel and gas-chromatograph (GC) exhaust gas analysis. In total 15 cases were analyzed by varying the H_2:CO_2 volumetric ratio (6, 5, and 4) and the pressure (1.5, 3, 5, 8, and 10 bar).

All methanation cases were simulated with a proprietary CFD code. A detailed literature mechanism was initially used and then scaled to obtain good agreement at high pressures. Subsequently, a two-step methanation mechanism developed at PSI for atmospheric pressure was extended to provide good predictions at pressures up to 10 bar. Finally, a theoretical comparison of CO_2 methanation on Rh and Ni was performed and showed the superiority of Ni catalysts.

A numerical work was also conducted, related to a companion SNSF project for the development of a particle-resolved Lattice Boltzmann (LB) model for biogas methanation. Therein, high-fidelity simulations were conducted using an LB solver to study the convection-diffusion-reaction processes inside and around catalytic porous particles used in methanation fluidized beds. A new catalytic model was developed, valid for arbitrary Damköhler numbers, for either equimolar or strongly non-equimolar reactions, and with the inclusion of velocity and concentration jumps (finite Knudsen number effects). The model was subsequently applied to a real porous particle whose 3D geometry was reconstructed with the X-ray tomography measurements. The geometry of the porous particles and the simulations indicated that the pore distribution is not spatially homogenous, in contrast to the common assumption used in up-scaled models. Finally, simulations were performed for spherical porous particles having an artificial macropore to evaluate the impact of spatial porosity inhomogeneity and Damköhler number. It was shown that the impact of the particle's outer surface was non-negligible, and the species concentration distributions at the particle's outer surface were non-symmetric even when the catalytic particle was an ideal sphere.

Important steps in the further development of fluidized bed methanation and the technology transfer to industry were achieved. The GanyMeth pilot plant (TRL 6) was successfully used for reactive experiments at up to 200 kW and confirmed the results of the TRL 4/5 plant, i.e. the technology can be scaled in a safe way. Within the European Union Project HyFuelUp, the industrial partner AlphaSYNT will design and build with the help of PSI a 500 kW methanation unit to be integrated in a TRL 7 demonstrator in Portugal, covering the value chain from low grade biomass via gasification, gas cleaning, methanation and liquefaction to Bio-LNG for heavy transport.

Main findings

- CO_2 methanation kinetics were assessed with detailed measurements at pressures up to 10 bar, revealing a pressure dependence $p^{0.41}$ for the production of methane. This finding allows for the efficient design of upscale high-pressure methanation plants, which can facilitate Switzerland's energy policy towards the use of renewable biogas fuels.

- The pilot methanation plant GanyMeth has been commissioned with successful biogas methanation experiments at pressures up to 10 bar. This is a crucial demonstration, opening the road for commercialization of the process.

Contents

Abbreviations

BET	Brunauer–Emmett–Teller
CFD	Computational Fluid Dynamics
FB	Fluidized Bed
GC	Gas Chromatograph
GDL	Gas Diffusion Layer
IPA	Isopropyl Alcohol
LB	Lattice Boltzmann
LNG	Liquefied Natural Gas
MGT	Micro Gas Turbine
PEFC	Polymer Electrolyte Fuel Cell
PLA	Polylactic acid
PTFE	Polytetrafluoroethylene
SEM	Scanning Electron Microscopy
SNG	Synthetic Natural Gas
SOFC	Solid Oxide Fuel Cell
SPSR	Surface Perfectly Stirred Reactor
TFM	Two Fluid Model
XTM	X-ray Tomography

1 Introduction

1.1 Background information and current situation

Fluidized beds (FBs) are two-phase flows of particulate solid material and fluid, which are used in many industrial applications for the efficient implementation of various physicochemical processes relevant to energy conversion. FBs are extensively used for the reforming and cracking of hydrocarbon oils, gasification of coal and biomass, solid and waste combustion, and methanation of biogas-derived synthesis gas. The latter is of special interest for Paul Scherrer Institute, whereby the conversion of biomass feedstock to Synthetic Natural Gas (SNG) is investigated as a viable pathway to produce a clean and CO_2-neutral fuel [1-4].

Above a minimum fluidization velocity, bubbles are formed such that FBs can be treated as consisting of two phases: a) gaseous bubbles, inside which there are practically no particles, and b) a particulate solid phase termed dense or emulsion phase. Bubbles forming at the bed bottom (distributor plate) rise upwards, grow and coalesce, creating larger bubbles that subsequently break up into smaller ones. This is shown in the simulation results of Figs. 1.1(a1, a2) [5], providing instantaneous 3D bubble distributions for PSI's large methanation fluidized bed [3, 4]. Two configurations are depicted, for a bed without cooling tubes in Fig. 1.1(a1) and for a bed with vertical cooling tubes in Fig. 1.1(a2). On the bed surface (the irregular surface demarcating the bed height, see Fig. 1.1(a1)), bubbles burst and eject particles. This process creates an intense particle circulation manifested by the particle patterns in Figs. 1.1(c1, c2)). The fluid above the bed surface is typically free of particles (see e.g. the gas fraction distributions in Figs. 1.1(b1, b2)). In the trailing wake of the bubbles the particles move upwards, while around and in-between the bubbles (and especially near the walls) the particles move downwards.

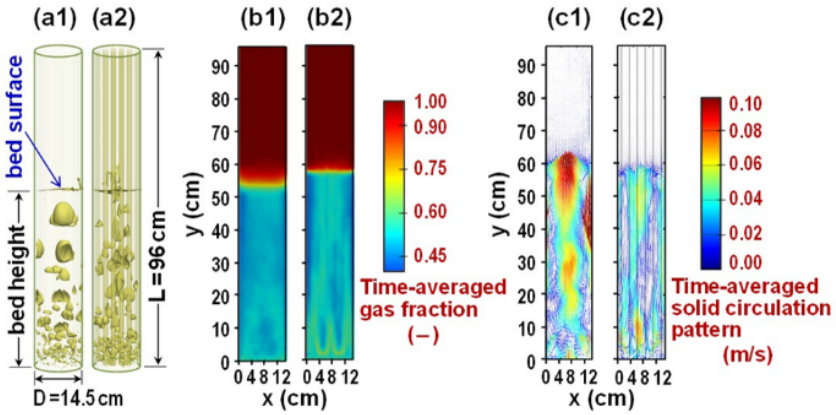

Fig. 1.1. Simulations in a fluidized bed without embedded vertical cooling tubes (a1, b1, c1) and with embedded vertical cooling tubes (a2, b2, c2). The configurations in (a1, a2) are used at PSI for biogas methanation. (a1, a2) instantaneous 3D bubble contours, (b1, b2) time averaged porosity (gas fraction), and (c1, c2) time averaged circulation patterns of the solid (color denotes the solid velocity magnitude). The ratio of the superficial gas velocity to the minimum fluidization velocity is 4.5. Adapted from [5].

Gas-solid fluidized bed reactors are used for the methanation of biogas. Typically, methanation on Ni (which, for cost reasons, is the preferred catalyst in industrial systems) is performed between 250 and 450 °C. The key chemical reactions for CO methanation are:

$3\ H_2 + CO \leftrightarrow CH_4 + H_2O$ ΔH_R^o = - 206.28 kJ/mol, (R1)

$CO + H_2O \leftrightarrow CO_2 + H_2$ ΔH_R^o = - 41.16 kJ/mol, (R2)

$2\ CO \leftrightarrow C + CO_2$ ΔH_R^o = - 172.54 kJ/mol, (R3)

A similar process occurs for CO_2 methanation, governed by the overall reaction:

$4\ H_2 + CO_2 \leftrightarrow CH_4 + 2H_2O$ ΔH_R^o = - 165.0 kJ/mol, (R4)

For CO methanation, R1 is the main reaction, R2 is the water gas-shift and R3 the Boudouard reaction, the latter being important only at low H_2/CO ratios. The exothermicity of the three reactions necessitates efficient removal of heat and this can be achieved with vertical cooling tubes, as shown in Fig. 1.1(a2). For CO_2 methanation, there is one controlling reaction (R4) with negligible contributions from R3 and with R2 becoming important above 600 K. R4 is also an exothermic reaction, requiring cooling arrangements similar to the CO methanation.

Measurements at PSI, pertaining not to the large FBs shown in Figs. 1.1(a1, a2) but to a smaller unit (diameter 52 mm and height 145 mm [3]) are typically used for modeling and kinetic validation. An axially-traversable sampling probe/thermocouple measures the species compositions and temperature along the bed height. Commercial Ni/γ-Al_2O_3 catalytic particles are used (50 wt% Ni/Al_2O_3, BET area 183 m^2/gr). The catalytic particles are of Geldart B type, with internal porosity around 50%. The particle size distribution and morphology measured with laser diffraction and SEM, respectively, of bare γ-Al_2O_3 particles without Ni used for fluid dynamic research is depicted in Fig. 1.2.

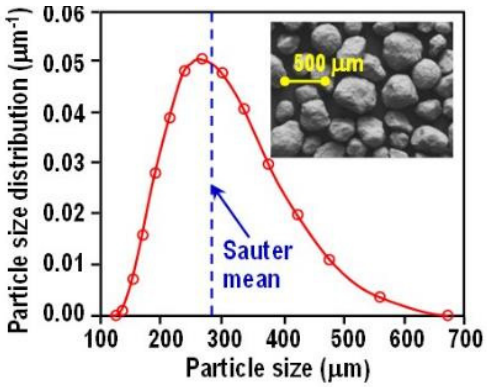

Fig. 1.2. Size distribution of γ-Al_2O_3 particles used for fluid dynamic research (Sauter mean diameter of 290 mm) and particle morphology (adapted from [2]).

Increased pressures lead to process intensification and hence to reduced FB sizes, which is highly desirable for practical applications such as coupled biogas methanation FBs and SNG-fired power generation systems. Moreover, the volumetric reduction in the main methanation reaction R1 (CO methanation) or R4 (CO_2 methanation) thermodynamically favors elevated pressures. This is illustrated in Fig. 1.3, showing thermodynamic calculations carried out at PSI for CO and CO_2 methanation. Higher pressures allow for more efficient methanation (higher CO or CO_2 conversions and higher CH_4 selectivities).

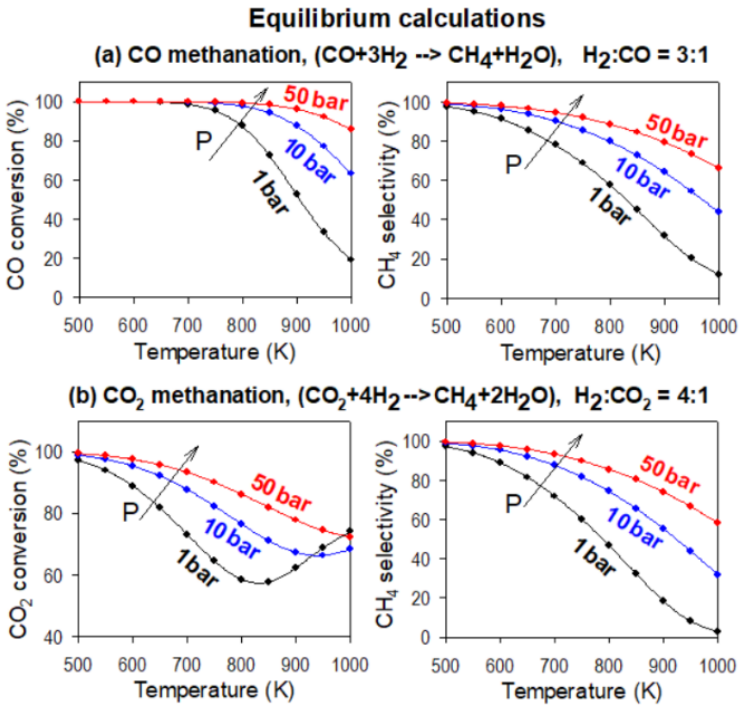

Fig. 1.3. (a) CO methanation and (b) CO_2 methanation equilibrium calculations at various pressures and temperatures. Stoichiometric compositions are used in both cases. Calculations of the present work.

With funding from *Swiss Electric Research*, the GanyMeth high-pressure test rig has been built at PSI, to facilitate research on biogas methanation FBs at pressures up to 10 bar and thus directly address commercialization aspects of this technology. However, until now there have been no reliable measurements of the CO or CO_2 methanation kinetics (e.g. reaction R1 or R4) at industrially-relevant pressures up to 10 bar. Suitable high-pressure experiments could help to identify the rate expression that represents best the reaction kinetics (R1 or R4) over a wide range of operating conditions. To our knowledge, catalytic kinetic schemes for biogas (CO/H_2 or CO_2/H_2) methanation valid at wide pressure ranges (e.g. 1 to 10 bar) have not yet been reported in the literature.

Experiments at PSI pertaining not to a smaller unit (diameter 52 mm and height 145 mm) are shown in Fig. 1.4. An axially-traversable sampling probe/thermocouple was used to measure the species compositions and temperature.

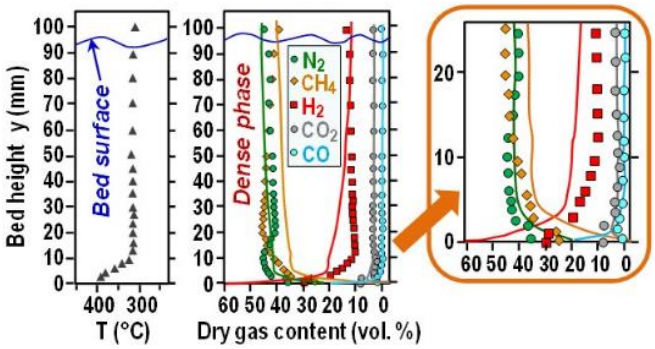

Fig. 1.4. Temperature and vol. composition along the bed (symbols: measurements, lines: predictions) for a case with 100 gr catalyst and inlet flow 10 nL/min (adapted from [2]).

Measured and predicted (using a macroscopic numerical model) chemical compositions as well as measured temperatures are shown in Fig. 1.4 for a case with 100 gr catalyst, inlet flowrate 10 nL/min and pressure 1.3 bar. The CO methanation reaction is largely completed in the first 20 mm.

The macroscopic methanation models of PSI used in Fig. 1.4 belong to the Two-Fluid-Model (TFM) class. Main simplifications include steady-state and one-dimensionality. Key model assumptions are [2]:

a) The gas chemical composition in the emulsion phase is the same as that inside the porous particles.
b) The bubble (gas) and emulsion phases are treated as plug flows (axial dispersion is not considered).
c) Methanation and water-gas-shift reactions are included, while the measured temperature profile (see Fig. 1.4(b)) is used as input to the model, negating solution of the energy equation.
d) The gas flow rate through the dense phase is constant. Because of volume contraction in the dense phase due to the methanation reaction, an extra convective mass transfer (bulk flow) from the bubble phase into the dense phase has been introduced.

For high-pressure operation, there is lack of a reliable kinetic information that can be fed to the TFM model.

1.2 Purpose of the project

The main purpose is to develop a catalytic reaction mechanism for the methanation of biogas over Ni/Al_2O_3, catalysts, valid over the industrially-relevant pressure range 1 to 10 bar. To this direction, the optically accessible catalytic reaction test rig available at PSI has to be adapted to carry out biogas methanation tests, using in situ laser-based measuring techniques as well as exhaust gas analysis (gas chromatography). Furthermore, numerical simulations with PSI's proprietary reactive CFD code will model the aforementioned experiments and thus facilitate the extraction of high-pressure kinetics. Ultimate goal is to provide a simple algebraic expression for the pressure dependence of the methane yields, which can be used for design purposes. This part comprises the main Workpackages WP1 and WP2 of the BfE project.

1.3 Objectives

Develop high-pressure kinetics for biogas methanation (main Workpackages WP1 and WP2). In addition

to the main tasks of the BfE project, a mesoscopic lattice Boltzmann (LB) code has been developed within the parallel-running SNSF project 200021_179019, aiming at studying interactions between external and internal particle diffusion, convection and reaction in catalytic Ni/Al_2O_3 particles. Such microscopic understanding is crucial in optimizing the macroscopic hydrodynamics/reacting code of PSI for the entire FB. The progress in the LB code development of the SNSF will also be reported (WP5).

In terms of the GanyMeth activities, the commissioning of the GanyMeth at pressured up to 10 bar will be reported (WP3 and WP4) along with the implementation of the new kinetics into PSI's macroscopic model (WP6) and a cost assessment analysis (WP7).

2 Description of facility

The GanyMeth pilot-scale biogas methanation facility (see Fig. 2.1) has been built during the last seven years from funding outside the current BfE project (mainly *Swiss Electric Research* and SCCER BIOSWEET). The plant comprises a TRL 6 fluidized bed reactor with an inner diameter of 22.4 cm. Catalyst can be filled up to 2 m high in the reactor that covers conditions up to 11 bar and 400°C. The gas is supplied from tanks (CO_2, H_2 from electrolysis) or from gas bottles and can be heated and saturated with steam. This way, typical gas mixtures for CO_2 methanation, biogas methanation and conversion of gasification-derived producer gas can be investigated experimentally.

The reactor design and the cooling system (thermos-oil in heat exchanger tubes) are chosen such that the results can be scaled-up and realistic tests with respect to part load and reactor dynamics are possible. The reactor is equipped with an axial sampling probe allowing for measurement of temperature and gas concentration profiles. Further, optical probes can be inserted radially to enable investigation of the fluid-dynamics.

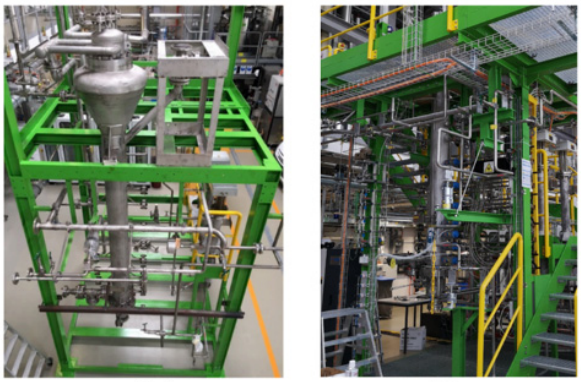

Fig. 2.1. GanyMeth test-rig at PSI: (a) High-pressure Fluidized Bed reactor, (b) complete setup.

3 Procedures and methodology

3.1 High-pressure test rig

The channel-flow reactor comprised two 3-mm-thick horizontal plates made of FeCr-alloy, each having length (-x), width (-z) and vertical separation (-y) of 300 mm, 104 mm and 7 mm, respectively. The two FeCr-alloy plates were affixed via eight screws onto two 6-mm thick steel plates, with the latter having the same length and width as the FeCr-alloy plates. The steel plates provided the needed rigidity and flatness for the FeCr-alloy plates during high pressure and high temperature operation. The FeCr-alloy plates served as a suitable high-surface support material for the Ni/Al_2O_3 catalyst (Ni/Al_2O_3 could not be applied directly on the steel plates). Furthermore, all previous experimental atmospheric-pressure methanation kinetic studies at PSI have been carried out on Ni/Al_2O_3 supported on FeCr-alloy [3, 6], thus allowing for direct transfer of the expected results. The reactor enclosure was finally completed by two 5-mm-thick vertical quartz windows (see Fig. 3.1(a)).

The reactor was affixed in an insulated Inconel frame and the integrated assembly was positioned inside a high-pressure cylindrical steel vessel with an internal diameter of 26 cm. Optical access to both 300×7 mm^2 reactor sides was facilitated by two 350 mm long and 35 mm thick quartz windows on the vessel (Fig. 3.1(a)). The surface temperatures were monitored by 12 (for each plate) S-type thermocouples, situated along the x-y symmetry plane and affixed 0.9 mm beneath the catalyst through 1.2 mm diameter and 5.1 mm deep holes drilled from the outside steel surfaces. The inside surfaces of the FeCr-alloy plates were coated with Ni/Al_2O_3 catalyst, as will be described in the next section.

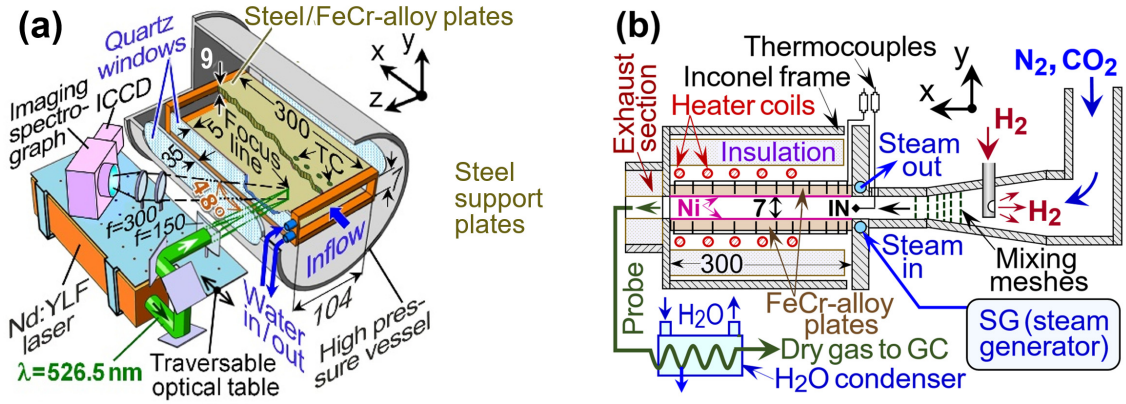

Fig. 3.1. (a) Test rig, Raman optical setup, (b) reactor details and GC gas analysis (all dimensions are in mm).

Attaining the desired catalyst temperatures for kinetic investigation (up to 750 K) is quite demanding, despite the exothermicity of the methanation reaction. This was due to the large thermal inertia of the thick FeCr-alloy and steel plates and the ensuing heat conduction losses to the supporting Inconel frame. To compensate for the heat losses, the front FeCr-alloy/steel faces (104×9 mm^2) were heated by a superheated steam circuit inside the Inconel frame (see Fig. 3.1(b)); the steam was produced by a dedicated steam generator (60 g/min at 620 K, supplied by a Cellcraft E-Series steam generator). Furthermore, the downstream parts of the reactor ($100 < x < 300$ mm) were heated with two resistive coils (Fig. 3.1(b)). The combination of these heating arrangements allowed catalyst surface temperatures up to 750 K.

Batteries provided H_2, CO_2 and N_2, with three Brooks mass flow meters regulating the individual gas flowrates. N_2/CO_2 premixtures were injected counterflow into the H_2 stream (Fig. 3.1(b)), and final mixing of the two steams was achieved in a 200 mm long steel conical unit (Fig. 3.1(b)). Good mixing and uniform exit velocities were obtained, as confirmed with Planar Laser Induced Fluorescence (PLIF) measurements of NO (100 ppmv of NO doped into the H_2 stream) and hot-wire velocimetry measurements, respectively (see Fig. 3.2). A K-type sheathed thermocouple, marked "IN" in Fig. 3.1(b) measured the inlet (x = 0) gas temperature.

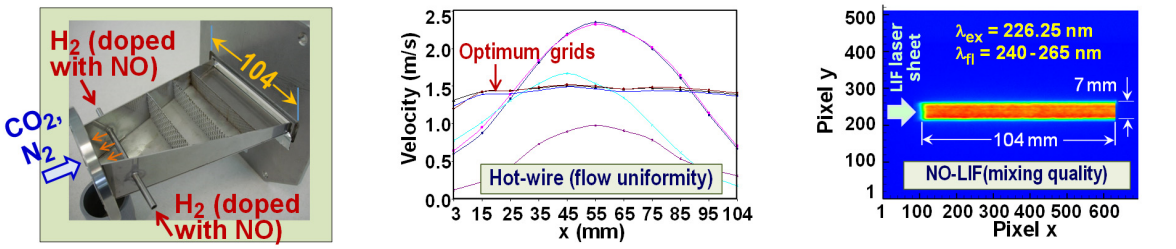

(a) Conical mixing section

(b) Verification of uniform exit velocity

(c) Verification of good mixing

Fig. 3.2. (a) Conical section used for mixing of $H_2/CO_2/N_2$ gases, (b) assessment of uniform exit velocity using hot wire velocimetry and (c) assessment of good mixing quality using PLIF of NO (doped into the H_2 stream).

3.2 Measuring techniques

For the assessment of the catalytic reactivity, workhorse was the Raman spectroscopy technique that provided transversely resolved major species profiles at selected axial positions. Excitation for the Raman measurements was achieved by a frequency doubled Nd:YLF laser beam at 526.5 nm (Quantronix Darwin Duo 80, 2 kHz repetition rate, pulse energy and duration of 40 mJ and 120 ns, respectively). The beam was focused by an f = 150 mm cylindrical lens into a 0.3 mm thick vertical line, which spanned the full 7 mm channel height (Fig. 3.1(a)). The focus line was offset 15 mm (in -z) from the x-y symmetry plane, to enhance the signal collection angle and diminish thermal beam steering. The collecting optics included two spherical lenses (f = 300 mm, f/4) that focused the scattered light into a 25 cm spectrograph (Chromex-250i) supplied with an ICCD camera (Princeton-Instruments PI MAX1024GIII, 640×255 pixels, pertaining to spectral shift and y-distance, respectively). The 7 mm channel height was resolved with 220 pixels, which were subsequently binned to 64 pixels.

A tilted holographic notch filter (Kaiser-Optical-Systems 532 nm) and a glass filter (OG550 Schott) in front of the ICCD lens suppressed interferences from the excitation beam. A traversable optical table housed all optics (including the Nd:YLF laser and the spectrograph), while the 48° angle between the sending and collecting optical paths (see Fig. 3.1(a)) allowed Raman measurements over the axial extent 8 mm ≤ x ≤ 139 mm. Since all experiments were performed at steady operating conditions, scattered light from 180,000 to 360,000 laser pulses (increasing number with decreasing pressure) was integrated on the detector chip to increase the signal to noise ratio.

The effective Raman cross sections were assessed by recording signals from pressurized CO_2, H_2, N_2, CH_4 and the actual reactive mixtures. For species with volumetric contents > 3% the measurement accuracy was ±3%, whereas for volumetric contents down to 0.3% the accuracy dropped to ±8%; lower contents could not be effectively resolved. Owing to low signal to noise ratios, data within 0.5 to 0.7 mm from the catalytic walls were not considered.

In the Raman measurements, apart from Dr. Ioannis Mantzaras, the Technician Mr. Jürgen Theile and the PSI laser diagnostician Dr. Ulrich Doll, a PhD student from our group (Mr. Vinoth Arumugam, supervisor: Ioannis Mantzaras) was actively involved. Mr. Arumugam is funded by an EU Horizon-2020 project (Project title: NextMGT – Next Micro-Gas-Turbines) and the topic of his PhD Thesis is the investigation of hetero-/homogeneous combustion methodologies for low-calorific-value Solid Oxide Fuel Cell (SOFC) off-gases. The products of the SOFC off-gas combustion can be then used to drive a Micro Gas Turbine (MGT), leading to a hybrid SOFC/MGT energy conversion system. The SOFC off-gases comprise H_2, CO, H_2O, CO_2 (and in certain cases CH_4) and given the similarity of these species to those in the methanation project, Mr. Arumugam was fully involved in the experiments such that he could gain valuable expertise on Raman spectroscopy and then apply it to his own project.

In In addition to the Raman measurements, the concentrations of all major species in the exhaust were assessed by gas analytics. A cylindrical exhaust section was attached to the reactor (Fig. 3.1(b)). In the exhaust section and 200 mm downstream of the reactor outlet, gas was sampled by a water-cooled probe. After condensing the water vapor in a dedicated water-cooled heat exchanger, the dried gas was directed to a GC (Gas Chromatograph). A Varian Micro-GC CP 4900 Quad with four channels was used, whereby each channel consisted of a micro-injector, a pre-column for backflush and a main column, as well as a thermal conductivity detector (TCD). Two molecular sieve columns (channels 1 and 3) separated five components, He, H_2, N_2, CH_4 and CO. Two PoraPlot U columns (channels 2 and 4) retained hydrocarbons and CO_2, while He, H_2, N_2 and CO passed rapidly and unresolved. GC measurements were averaged over ~2.6 min, while successive ~2.6 min long records were stored in a dedicated PC during each ~60 min long steady state experimental run. The GC elemental balances were within 3%.

The exhaust gas measurements offered an additional kinetic validation tool, since the optical collection setup limited the Raman measurements to x ≤ 139 mm, while numerical simulations could be carried out over the full 300 mm channel length.

3.3 Catalytic plates

This task took more than 6 months to complete, as the coating procedure proved very challenging. First, a few unsuccessful attempts are described and finally the successful coating procedure is outlined.

a) In the first approach, a 10 mm thick steel plate was used along with a 100 μm thick FeCr-alloy foil, which was glued onto the steel plate. However, after thermal pre-treatment of the steel/FeCr-alloy assembly (still without Ni/Al_2O_3 coating) at 950°C, the FeCr-alloy foil was detached from the steel plate due to different thermal expansion coefficients of the two glued materials (see Fig. 3.3(b)).

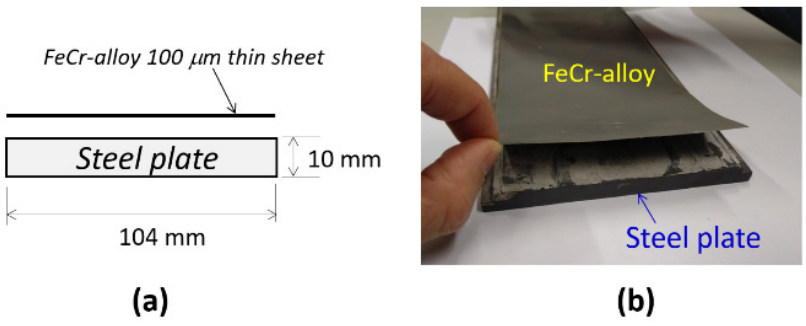

Fig. 3.3. First unsuccessful coating approach. (a) Dimensions of steel plate and FeCr-alloy foil. (b) The glued FeCr-alloy foil detaches from the steel plate after calcination at 950°C.

b) To avoid detachment of the FeCr-alloy foil, three grooves were machined on the steel plate to allow for airflow under the FeCr-alloy foil (anticipating better adhesion, since the glue binder requires air for solidification), see Fig. 3.4. Despite these improvements, the glued FeCr-alloy foil still detached from the steel plate after calcination of the assembly at 950°C. Furthermore, internal thermal stresses caused the foil to become corrugated after thermal treatment. Hence, this design was also abandoned.

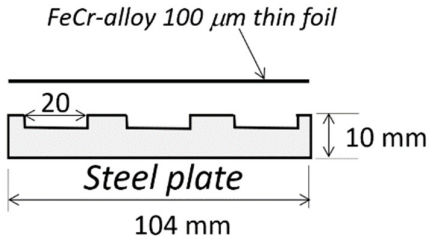

Fig. 3.4. Second unsuccessful design. Three 20-mm-long and 2-mm-deep grooves on the steel plate.

c) The third and final attempt involved bolting (instead of gluing) a 3 mm thick FeCr-alloy plate on a 6 mm thick steel plate. The schematic is shown in Fig. 3.5(a) and photographs of the FeCr-alloy plate with its attached screws and the entire steel/FeCr-alloy assembly are depicted in Fig. 3.5(b). This assembly was thermally pre-treated to 950°C without any visible deformations.

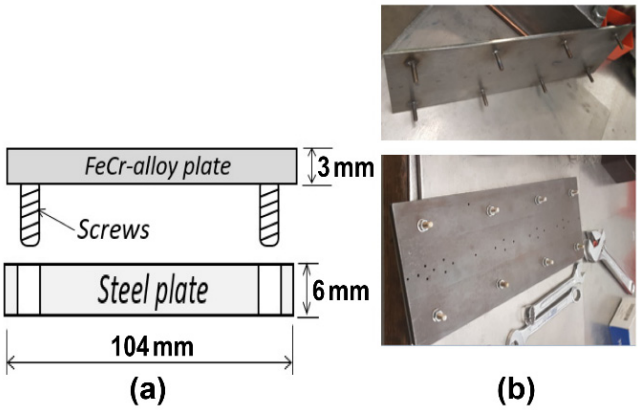

Fig. 3.5. Third, successful design: (a) 3 mm thick FeCr-alloy plate with screws on it and 6 mm thick steel plate. (b) Top photograph: FeCr-alloy plate with welded screws. Bottom photograph: FeCr-alloy and steel plate assembly held together by eight screws.

3.4 Coating procedure

The FeCr-alloy top surface was coated with catalyst powder using an alumina-based binder. This methodology was already used at PSI in a kinetic study on the same catalyst material by Kopyscinsky et al. [3]. It requires the preparation of a slurry from the binder and the catalyst powder, which then has to be applied on the support material.

Several methods are available to apply catalytic coatings on support materials. Common techniques to apply slurries are briefly reviewed in order to find the most suitable method.

Spin coating: After applying a defined amount of slurry to the surface the sample is spun, such that the slurry forms an even layer on the support material. This method is used in Kopyscinsky [3] in their kinetic study. Due to the sheer size and mass of the plates to be coated, this method seemed unfeasible due to technical reasons and it was not further considered.

Spray coating: The slurry is sprayed evenly on the surface. This procedure was not further considered, as obtaining a uniform layer by a manual coating procedure proved difficult to achieve. Furthermore, safety concerns were raised since a Nickel-containing aerosol would be produced, requiring appropriate safety protection measures.

Dip coating: A catalyst slurry is prepared and the support structure is dipped into this liquid. This method is often used in the coating of monolithic support structures. Since the goal is to coat a single surface and quantification of the catalyst deposited on the surface would have been difficult, this method was also not considered. Furthermore, a large amount of catalyst slurry would have had to be prepared, which would raise safety concerns (Ni is carcinogenic) and pose a waste of ground catalyst material.

Brush coating uses a brush or doctor blade to spread a certain amount of slurry across the surface to be coated. The technique was applied by Kopyscinski et al. [3]. In their work, they discuss the uneven distribution of catalyst material along the reactor plates. They had to compensate this by determining the thickness of the deposited catalyst layer. Because in the current project much larger plates need to be coated, the problem of uneven distribution of catalyst may be worse. Furthermore, the quantification of the amount of deposited slurry is difficult.

Frame coating requires a removable frame around the support structure, where a defined amount of slurry is poured in. This methodology is using a 3D-printed polylactic acid (PLA) frame. Since the amount of deposited catalyst material can be simply determined by mass balancing and the size of the frame is easily scalable to the size of the plates in the current project, it was decided to use the frame coating technique. Furthermore, the Ni-containing slurry could be handled by pipetting and syringes.

Pre-tests for frame construction and slurry preparation:

In the method used by Kopyscinsky et al. [3], mixtures of water and isopropanol (IPA) were used as solvents. As a binder, both studies use the alumina-based material Disperal P2 (Sasol, Germany). At least in the study of Kopyscinsky et al. [3], the same catalyst material was used as in the current project. It is therefore assumed that no fundamentally new development of the coating procedure is required and the methods of the two studies can be adapted.

The pre-tests were performed with the focus on three aspects: 1) the catalyst loading, 2) the construction and stability of the frame, and 3) the scalability of the procedure to the full-scale plates.

The pre-tests were performed on two different scales. The small-scale tests were performed using a circular PTFE frame with a rubber sealing, which was mechanically pressed onto a thermally pre-conditioned (1000°C, 24 h in air) FeCr-alloy foil or aluminium plates as support. The medium-scale tests were performed using rectangular aluminium plates (150x100x3 mm, ½ length of full-scale plate) as support. Aluminium plates were chosen, as they provide a very similar aluminium oxide surface structure as the thermally pre-treated FeCr-alloy. It also allowed us to test the frame construction and dismantling at a relevant scale using inexpensive material. Prior to use, the aluminium plates were roughened with sand paper and washed with water and isopropanol.

Due to the safety hazards posed by the Nickel catalyst, part of the pre-tests were performed using γ-Al_2O_3 powder, which corresponds to the support material of the catalyst. Several small-scale tests were performed, testing different loadings of aluminium powder. Initially, high loadings of catalyst material were targeted in order to achieve a high conversion in the plate reactor and facilitate gas-phase

analytics. Nevertheless, the small-scale pre-tests with alumina powder showed that high loadings of catalyst material lead to spalling of the layer. It was decided that the loadings to be used for coating should be kept in the range used already by Kopyscinsky et al. [3] (around 0.05 kg/m^2).

In several pre-tests, the construction of the frame was evaluated and optimized. Importantly, the materials used for the frame construction and the sealing had to be resistant to the solvents used in the slurry. For the sidewalls of the frame, polycarbonate slabs were used, which are resistant to IPA (see Fig. 3.6). To seal and attach the slabs to the support plate, taking a standard sealing solution was not possible, especially in the corners, achieving leak tightness would have been difficult. It was decided that using a plastic material as a flexible sealant and glue. As a suitable material polycaprolactone could be identified. This polymer has a melting point of around 60°C to 80°C and is insoluble in isopropanol and water. Due to the pandemic situation and limited access to lab facilities, the pre-tests for frame construction were performed at home, as only harmless materials were involved.

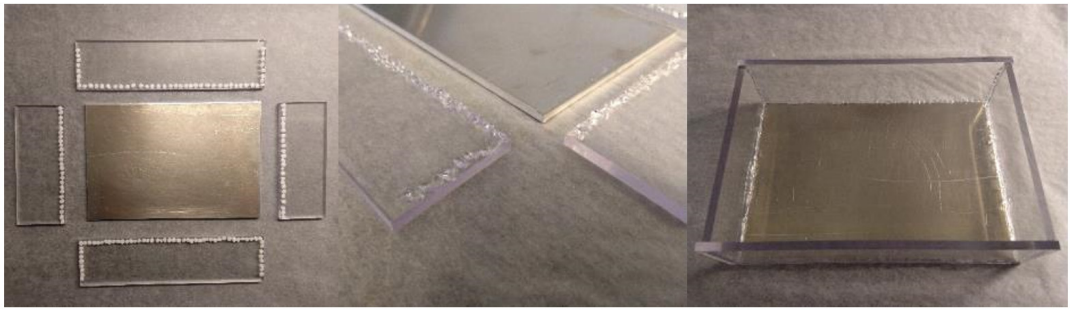

Fig. 3.6. Various constructed frames.

In order to test the scalability of the coating method, especially the slurry preparation, small- and medium-scale pre-tests were performed using a catalyst loading of 0.08 kg/m2. With these tests, we could see that a uniform layer on FeCr-alloy could be achieved (small-scale test), and that the slurry preparation procedure could be scaled up to half of the full scale (medium-scale test). Since also on medium-scale a uniform coating could be achieved, an influence of the materials used for the frame construction (polycarbonate and polycaprolactone) could be excluded.

Full-scale coating

After having established a working procedure in the first pre-tests, the full-scale coating of the two reactor plates was tackled. The two plates were thermally pre-treated in a high temperature oven (1000°C, 24 h, slow heating rates) in air. In order to have an identical composition of the coatings of both plates, it was decided to prepare only a single slurry. The appropriate volume of slurry was transferred to each plate. According to the pre-tests, the plates were left to dry overnight. After dismantling of the frame, the plates were calcined at 375°C for 5 h, using a slow heating rate of 5 K/min. On both plates, the coating showed a greyish discolouring. Furthermore, the mechanical integrity of the coating was insufficient: even slight touching or gas flow caused the catalyst powder to be carried away. The coating was therefore considered to be insufficient for use in the experimental set-up. Subsequently, the coating was removed from both plates. It remained unclear why the mechanical stability was low. Although the FeCr-alloy surface was thermally pre-treated to form alumina whiskers on its surface, the surface area might have been still too low to properly bind the catalyst powder. It was then decided to sandblast the surface of the FeCr-alloy plates to increase their roughness. Again, the two plates were thermally pre-treated in a high temperature oven (1000°C, 24 h) to form alumina whiskers on the surface. Since it was further

assumed that the high catalyst loading might have decreased the integrity of the coating, it was reduced from 0.08 kg/m2 to 0.04 kg/m2. Two additional coatings on small and medium scale were successfully performed to test the new recipe. Since the scaling of the slurry preparation might have been a further cause for errors, in this repetition of the coating procedure the slurry for each plate was prepared separately, but using the identical procedure.

After pouring the prepared slurry into the frame, the plates were dried overnight in the laboratory. In the hope to slow down the drying process and obtain a more uniform coating, as well as protecting the plates from dust, they were covered with a sheet of paper. The paper was placed on plastic bars, leaving a gap of around 2 cm between the frame and the paper. Interestingly, after drying only one plate showed a homogeneous coating suitable for the kinetic experiments (Plate A). The coating of the second plate (Plate B) showed severe flaking along the whole surface. It was decided that Plate A can be calcined and be used for the experiments. Plate B on the other hand was cleaned again by washing with water and isopropanol. As the identical procedure in the preparation of the plates and the slurry was used, it is unclear where the different outcome originated. We assumed that a too low binder content might have had an influence; therefore, it was decided to double the binder content in the coating relative to the catalyst mass. It furthermore was assumed that fast drying could have led to internal stresses in the catalyst layer. The next slurry was then only prepared using deionised water.

This coating of the Plate B was also not successful: during drying severe blistering of the coating was observed. The catalyst layer completely detached from the surface and rolled up in spider-web-like structures. It could be seen that, for our purposes, isopropanol was a crucial component of the slurry, which increased its stability. The catalyst layer was removed again and the plate washed with isopropanol and deionised water. The frame was not removed.

Based on previous experiences, the slurry preparation was changed again: As lower catalyst loadings may lead to more stable coatings, the loading was reduced from 0.04 kg/m2 to 0.016 kg/m^2. Furthermore, the liquid content per catalyst mass was increased in the hope to achieve a better spreading of the slurry and thus a more uniform coating. The changes in the procedure were successful and a uniform, stable coating was obtained. Subsequently, the frame was removed and the plate calcined (375°C, 5 h, heating rate: < 5 K/min).

Both plates were coated with catalyst, but each one had a different loading. In order to facilitate the optical measurements and simplify data evaluation, it was decided to adjust the catalyst loading on Plate B to the loading of Plate A. A frame was again attached to Plate B (see Fig. 3.7) and a slurry was prepared by applying the recipe of the previous coating. The amount of catalyst used for the coating corresponded to the difference required to adjust the loadings of Plate A and Plate B. The slurry was simply poured on top of the existing coating. The new coating showed sufficient uniformity and only minor blistering. The frame was removed and the plate calcined. As already a catalyst layer was present on the plate, it was decided to use a very low heating rate of 1.94 K/min. Again, the maximum temperature of 375°C was kept for 5 h.

(a)
Application of Ni/Al_2O_3 slurry on FeCr-alloy plate using a Plexiglas frame

(b)
Dried Ni/Al_2O_3 slurry on FeCr-alloy, after removal of Plexiglas frame

(c)
Catalyst coated on FeCr-alloy after calcination at 375 °C for 5 hr.

Fig. 3.7. General coating procedure with Ni/ Al_2O_3/carbon-slurry of the FeCr-alloy plates.

The final and successful catalyst coating was used for all subsequent methanation experiments.

Hence, Task 1.1 and Milestone 1 (reactor and coated plates ready) have been fulfilled.

3.5 Experimental conditions

The selected experimental conditions for CO_2 methanation are summarized in Table 3.1 below.

Case	P (bar)	H_2:CO_2 (-)	T_N (K)	H_2 (vol%)	N_2 (vol%)
A1	1.5	6	309	68.6	20
A2	3.0	6	311	68.6	20
A3	5.0	6	311	68.6	20
A4	8.0	6	311	68.6	20
A5	10.0	6	311	68.6	20
B1	1.5	5	310	66.7	20
B2	3.0	5	311	66.7	20
B3	5.0	5	313	66.7	20
B4	8.0	5	311	66.7	20
B5	10.0	5	308	66.7	20
C1	1.5	4	311	64.0	20
C2	3.0	4	311	64.0	20
C3	5.0	4	313	64.0	20
C4	8.0	4	311	64.0	20
C5	10.0	4	310	64.0	20

Table 3.1: Experimental conditions for methanation tests.

Given the stoichiometry of the methanation reaction ($4H_2 + CO_2 \rightarrow CH_4 + 2H_2O$), three H_2:CO_2 volumetric ratios were investigated: 4:1 (stoichiometric), 5:1 and 6:1. Ratios larger than the

stoichiometric value (= 4) were studied for two reasons: a) to facilitate the ensuing kinetic studies by providing a larger database, and b) to minimize coking (carbon deposition) onto the Ni/Al_2O_3 catalyst. It is noted, however, that coking is not of great concern for CO_2 methanation (as opposed to CO methanation).

Fifteen cases were investigated, with pressures of 1.5, 3.0, 5.0, 8.0 and 10 bar and H_2:CO_2 volumetric ratios of 6 (Group A), 5 (Group B) and 4 (Group C). The $H_2/CO_2/N_2$ mixtures volumetrically comprised 20% N2, while H_2 ranged from 64.0% to 68.6%. Nearly constant inlet temperatures were established with T_{IN} = 311 - 315 K; this small preheat was a result of upstream heat conduction through the solid walls of the mixing section. The inlet velocities (U_{IN}) were constant at a given pressure. For p = 1.5 bar the velocity was U_{IN} = 0.70 m/s and for higher pressures the velocities were scaled as $U_{IN,p} = [(p^* = 1.5 \text{ bar})/p] \times U_{IN,p^*=1.5}$, in order to keep the same inlet Reynolds number (and also the same mass throughput) in the five cases of each group. The flows were laminar with inlet Reynolds numbers (based on the channel height) of 208-240.

3.6 Raman data processing

The methanation process is investigated using simultaneous Raman measurements of major gas-phase species concentrations. The 1D distribution of the major species concentrations across a catalytic channel was measured from the Raman spectra at various axial positions, at steady operating conditions. In this section, the experimental data reduction procedure is briefly described.

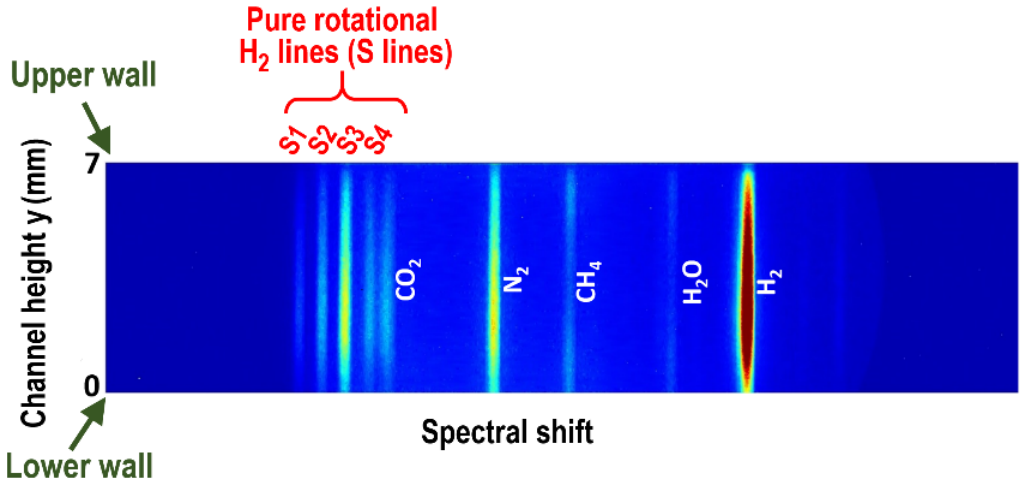

Fig. 3.8. Raw Raman data at a given axial position. The horizontal axis is the vibrational shift of the probed molecules and the vertical axis is the physical distance along the channel's height (upper wall y = 7 mm, lower wall y = 0 mm).

In Fig. 3.8, the vibrationally shifted radiation of all major gaseous species is shown, as recorded in the ICCD camera (see Fig. 3.1(a)), without any data processing. Due to the high amounts of H_2 (> 64%, see Table 3.1) the pure rotational H_2 lines are also visible (S lines) in Fig. 3.8. Note, the simple methanation reaction $4H_2 + CO_2 \rightarrow CH_4 + 2H_2O$ leads to major species with non-overlapping spectra, thus greatly facilitating the subsequent data analysis. The intensity of each species line (y-profile in Fig. 3.8) is an indicator of the local concentration. However, suitable processing is needed to extract quantitative information, such as transverse profiles of all species (mole fraction profiles $X_i(y)$, i = H_2, CO_2, H_2O, CH_4,

and N_2). Even without any processing, it is evident from Fig. 3.8 that H_2 and CO_2 are the reactants (since their intensity drops near the upper and lower catalytic walls) and CH_4 and H_2O are the products (since their intensity is highest near the upper and lower catalytic walls and drops towards the channel center).

As a first step, a noise background subtraction is performed. Fig. 3.9(a) shows the intensity variation at the channel half-height, y = 3.5 mm (centerline). A polynomial fit of the background signal accounts for the contribution from spectrally-varying stray light. The fitted background signal (purple line in Fig. 3.9(a)) is then subtracted from the raw spectra. The process of curve-fitting and subtraction is applied row-wise in the entire image matrix to account for non-uniformities of the background across the channel height. The background-subtracted image is depicted in Fig. 3.10. Further, areas within 0.5 mm from the catalytic walls have been removed due to low signal-to-noise ratios (originating from optical vignetting). The background-subtracted images in Fig. 3.10 are inputs to the next processing step in the data reduction.

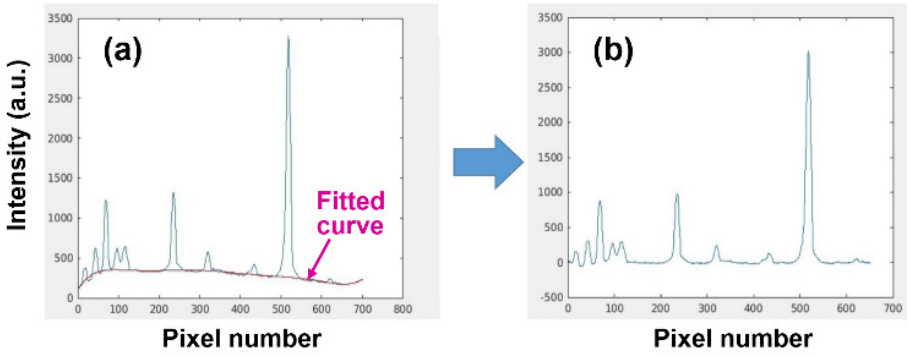

Fig. 3.9: (a) Intensity profiles at half-height (y = 3.5 mm) of the raw data and fitted background signal (line). (b) Intensities after background subtraction.

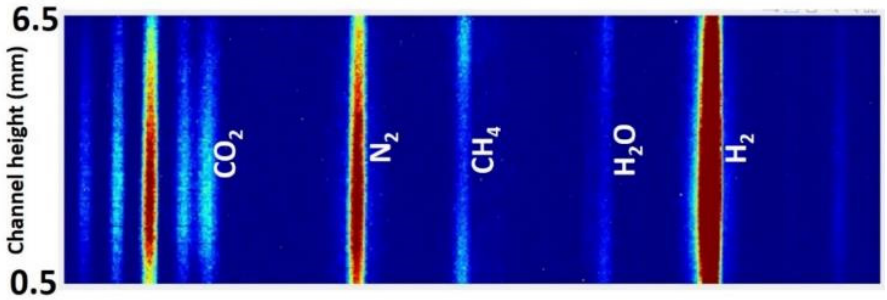

Fig. 3.10. Background-subtracted image with Raman spectra of all major species.

In order to obtain species concentration profiles from background subtracted images, firstly an intensity profile is obtained by integrating the Raman spectral line signals of each specific species over its spectral bandwidth. Then the smooth curves of integrated profiles are obtained using polynomial curve fitting (8^{th} order). The variation in intensity profiles also includes variation due to laser sheet non-uniformity and variation of temperature (higher temperature → lower density → lower species number density → lower signal). The wall temperatures (where exothermic catalytic reactions occur) are higher and the bulk channel temperatures are lower. For all species, these variations in intensities are corrected using

transfer functions obtained from the N_2 Raman spectral line at all axial locations. The corrected intensity profiles of all species are finally shown in Fig. 3.11. The N_2-profile is flat, due to the fact that the transfer function was obtained (by construction) from the N_2 Raman spectral line itself. Simulations show that the y-variation of N_2 is less than 3%, which is acceptable for the present analysis.

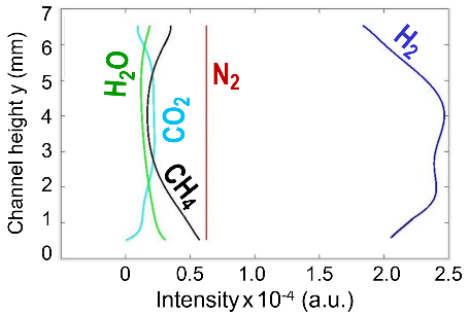

Fig. 3.11. Corrected integrated Intensity profiles of all species at a selected axial location.

The major species concentrations $[X_i]$, are determined directly from the integrated Intensity signal ratios I_i/I_{N2}, using Eq. (3.1) below. The mole fractions of species *i,* at any x-location are then calculated from Eq. (3.2).

$$[X_i] = \frac{I_i}{I_{N_2}^{cl}} \cdot \frac{1}{\sigma_i} \cdot [X_{N_2}]^{cl} \tag{3.1}$$

$$\frac{X_i^L}{X_{N_2}^*} = \frac{[X_i]^L}{[X_{N_2}]^*} \cdot \frac{T_{cl}^L}{T_{cl}^*} \tag{3.2}$$

The effective relative Raman cross-sections σ_i, which include transmission efficiencies (i.e. windows, lenses, optical filters, spectrometer and camera), were evaluated experimentally with known compositions of gas mixtures of major species.

Here $[\boldsymbol{X}_{N_2}]^*$ and $[\boldsymbol{X}_{N_2}]^{cl}$ are the inlet N_2 concentration (used as reference), the superscripts "*" and *"L"* in Eq. (3.2) denote the inlet and a particular downstream location, respectively. The superscript and subscript ***"cl"*** in Eqs. (3.1) and (3.2) indicate the channel half-height (or centerline) location.

The temperature ratios in Eq. (3.2) are obtained from our CFD simulations, whereby as wall boundary conditions the thermocouple-measured axial temperature profiles from the experiment are used. It is worth noting that although the gas temperatures can also be deduced from the Raman data (using as relevant parameter the sum of all species concentrations), the simulations are more accurate in providing gas temperature information. We have shown that the extent of the catalytic reaction changes only modestly the gas thermal conductivity, such that the predicted gas temperature profiles are largely independent (within 10 K) of the progress of the methanation reaction. The temperature ratios are in turn used to compute the mole fraction of every species *i* from Eq. (3.2).

As the signal intensity is directly proportional to the number density of the probed species, the Raman measurements are favored at elevated pressures. Hence, the quality of the data (signal-to-noise ratio) improves with increasing pressure. It is noted, however, that too high pressures (typically > 10 bar) have

the disadvantage of enhanced laser beam steering, which in turn deteriorates the data quality. Details on the Raman experiments have been given in our past works [9-12].

Finally, the CO_2 methanation tests did not lead to noticeable catalyst coking issues, in agreement to past literature studies that have shown that the presence of H_2O in the products mitigates coking.

Hence, Task 1.2 and Milestone 2 (Ni/Al_2O_3 tests completed) have been fulfilled.

3.7 Numerical procedure

The 300×7 mm^2 area along the reactor's *x*-*y* symmetry plane (see Fig. 3.1(a)) was simulated with a 2D steady Navier-Stokes CFD code (code details in Refs. [7, 8]). 840×74 grids in -*x* and -*y*, respectively, yielded grid-independent results. The temperatures at the lower wall (*y* = 0) and upper wall (*y* = 7 mm) were imposed as energy boundary conditions by fitting curves through the 12 thermocouple measurements on each plate. All inlet (*x* = 0) properties were uniform.

The thermodynamically consistent detailed mean-field mechanism from Schmider et al. [13] (Deutschmann mechanism) was used as an initial attempt to simulate the methanation of CO_2 on nickel (42 reactions, 5 gaseous and 14 surface species, surface site density 2.6×10^{-9} mol/cm^2).

The catalytic reaction rates were evaluated with the Chemkin package [20]. A mixture-averaged transport model with thermal diffusion for H_2 was employed [21]. Finally, the catalyst layer was thin enough to neglect intraporal diffusion. This was verified by calculating the Weisz modulus in our earlier work [6], which used the same Ni/Al_2O_3 catalyst for CO methanation at 1 bar.

4 Results and discussion

4.1 WP2: Simulations of experiments in optically accessible reactor

4.1.1 Comparisons of experiments and predictions

Measured and simulated transverse (-y) profiles of the reactant (H_2/CO_2) and main product (CH_4/H_2O) mole fractions are depicted in Fig. 4.1 for Cases A1, A3 and A5 (H_2:CO_2 = 6) of Table 3.1, at five selected axial locations. Likewise, mole fraction profiles of H_2 and CH_4 for Cases C1, C3 and C5 (H_2:CO_2 = 4) are provided in Fig. 4.2. For reasons of clarity, up to 16 of the total 64 measurement points are displayed over the Raman-resolved channel height $0.6 \lesssim y \lesssim 6.4$ mm. Additional comparisons of species profiles are shown in Fig. 4.3(a) and Fig. 4.3(b) for H_2:CO_2 = 5 and 4, respectively. The thermocouple-measured wall temperatures of all cases are summarized in Fig. 4.4. Over the length $34 \leq x \leq 139$ mm encompassing the profiles in Figs. 4.1, 4.2 and 4.3 (wherein the main kinetic investigation was carried out), the wall temperatures ranged from 502 K to 728 K. However, the exhaust gas analysis allowed for kinetic evaluations at axial positions downstream of the Raman data (i.e., $139 < x \leq 300$ mm), wherein, wall temperatures reached up to 760 K (see Fig. 4.4).

Before comparing simulations and Raman measurements, it is cardinal for the present kinetic study to ensure the absence of transport limitations –at least over the axial extent of the Raman data. To this direction, additional simulations were carried out using a global catalytic step for the reversible methanation reaction $4H_2 + CO_2 = CH_2 + 2H_2O$. To obtain the transport-limited (TL) solution, the reaction rate coefficient of the global step was increased until no change could be observed in the species profiles. Transport limited simulations are compared with detailed chemistry simulations in Fig. 4.5 for Case A5, clearly showing that the latter are away from the TL solution, falling in the mixed transport/kinetically controlled regime. Such an operating regime conveniently allows for the evaluation of kinetics by comparing the measured and predicted transverse species profiles.

The TL simulations indicate that CO_2 is the deficient reactant (its mole fraction vanishes at both walls), not only for H_2:CO_2 = 6 (see Fig. 4.5) but also for the stoichiometric composition H_2:CO_2 = 4.This is a result of the much higher diffusivity of H_2 compared to CO_2, which can profoundly alter the local stoichiometry at the catalytic walls [22]. Downstream of the Raman measurements, the reactant conversion falls again in the mixed transport/kinetic controlled regime as exemplified by the transverse plots at x = 300 mm in Fig. 4.5. Since the deficient reactant CO is well above zero at both walls over the full channel length in the detailed chemistry simulations, kinetic information can be deduced not only from the Raman measurements ($x \leq 139$ mm) but also form the exhaust gas analysis. Figure 4.5 shows also the computed equilibrium compositions (using 35 species) at the mean gas outlet temperature (x = 300 mm). The TL simulations at x = 300 mm yield appreciably higher reactant mole fractions compared to the outlet equilibrium, indicating that the channel length is not sufficient to attain the maximum conversion of reactants. It is noted here that the TL simulations with the reversible one-step reaction and the four involved reactive species (plus N_2) could still adequately capture equilibrium (within 2.2% over the investigated pressures and temperatures).

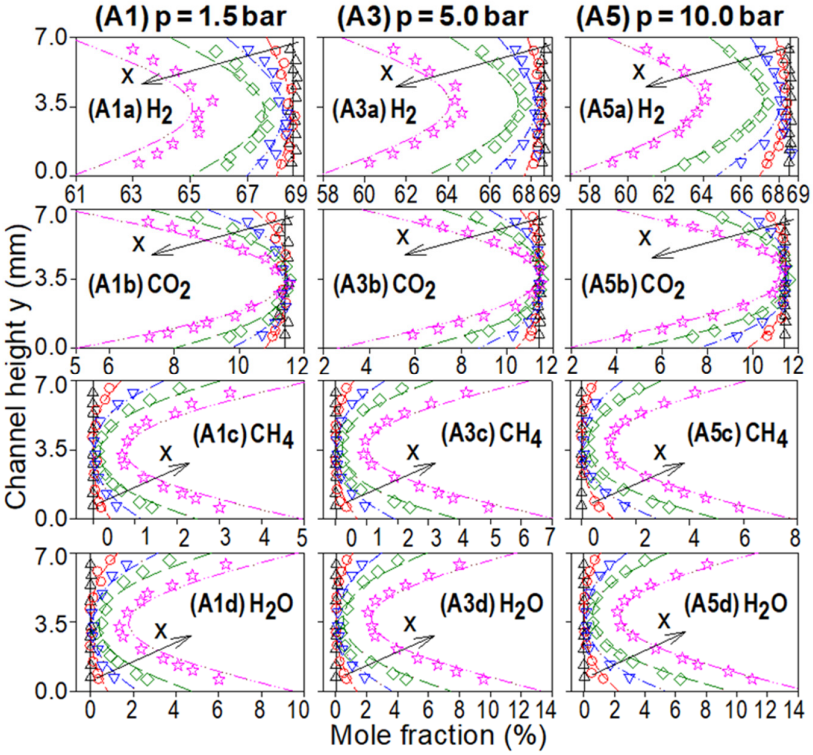

Fig. 4.1. Transverse (-y) profiles of species mole fractions (symbols: Raman measurements, lines: simulations), for Cases A1, A3 and A5, with H_2:CO_2 = 6. The axial locations are: x = 34 mm (upper triangles, solid lines), 80 mm (circles, short dashed lines), 96 mm (lower triangles, dashed dotted lines), 111 mm (diamonds, long dashed lines), 139 mm (stars, dashed double dotted lines).

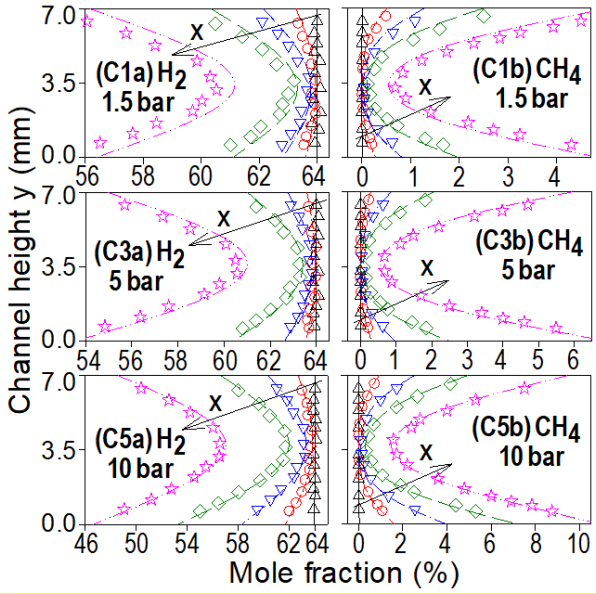

Fig. 4.2. Transverse profiles of species mole fractions), for Cases C1, C3 and C5 with H_2:CO_2 = 4. Symbol and line notations are the same as in Fig. 4.1.

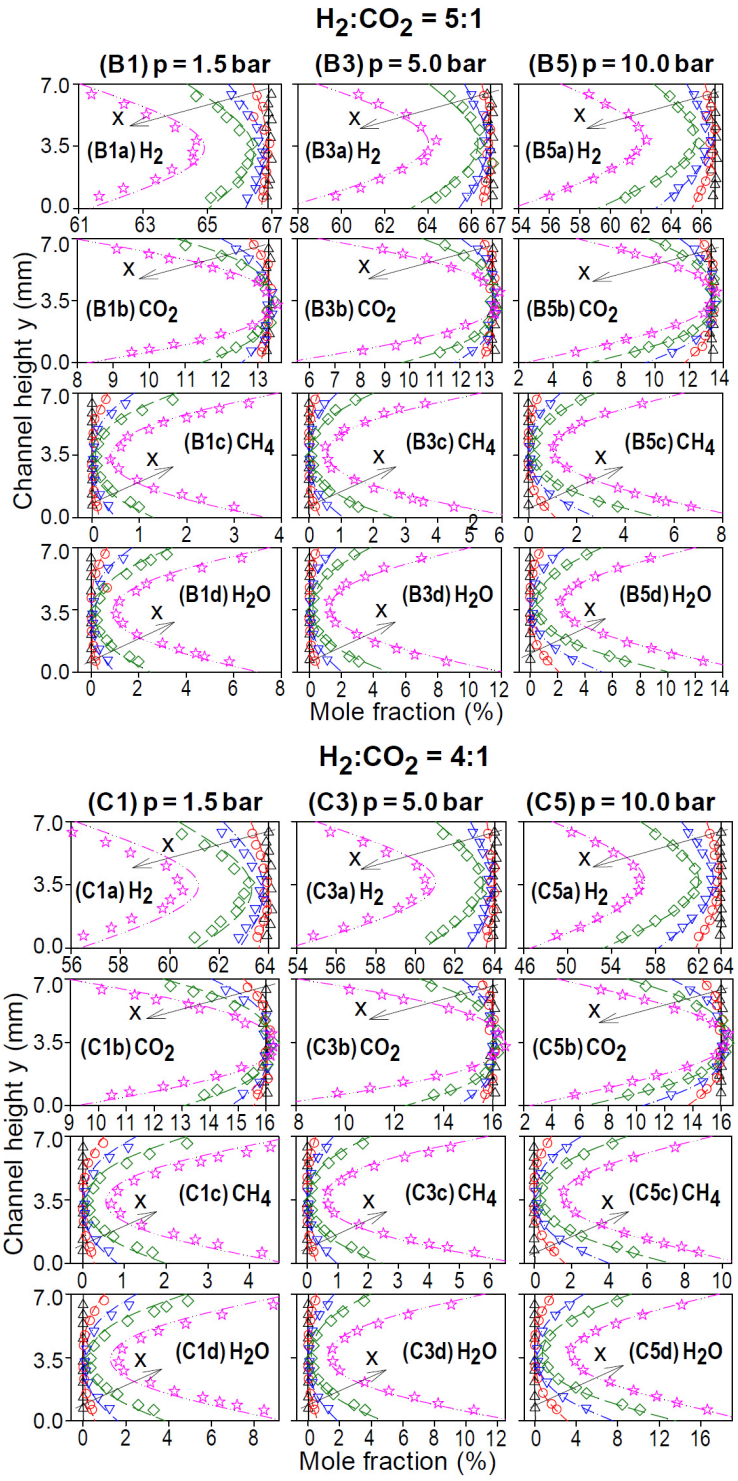

Fig. 4.3. Transverse (-y) profiles of species mole fractions (symbols: Raman measurements, lines: simulations), for: (a) Cases B1, B3 and B5, with H_2:CO_2 = 5, and (b) for Cases C1, C3 and C5, with H_2:CO_2 = 4. The line and symbol notation is the same as in Fig. 4.1.

Raman measurements and simulations at the first axial location x = 34 mm in Figs. 4.1 and 4.2 indicated a diminishing reactivity, manifested by the practically uniform profiles of all species. Hence, positions x < 34 mm, with even lower wall temperatures were not investigated. The measured and predicted species profiles in Figs. 4.1 and 4.2 were slightly asymmetric due to modest differences between upper and lower wall temperatures (see Fig. 4.4). The catalytic reactivity was an increasing function of pressure, as evidenced by the stronger drop (rise) of the reactants H_2/CO_2 (products CH_4/H_2O) at any given x-location in Figs. 4.1 and 4.2 when the pressure increased from 1.5 to 10 bar.

At the highest ratio $H_2:CO_2 = 6$, the simulations underpredicted (overpredicted) moderately the reactant (product) mole fractions. The differences, however, reduced with increasing pressure. Characteristically, the y-averaged H_2 mole fraction was underpredicted at x = 139 mm by 2.0% in Fig. 4.1(A1a) and by 0.68% in Fig. 4.1(A5a). Conversely, the much lower CH_4 mole fractions were overpredicted by 18.8% in Fig. 4.1(A1c) and by 7.4% in Fig. 4.1(A5c). As the ratio H_2/CO_2 decreased, the trend was reversed and the simulations overpredicted (underpredicted) modestly the reactants (products). The CH_4 mole fraction was underpredicted by 16.4% in Fig. 4.2(C1b) and by 4.4% in Fig. 4.2(C5b).

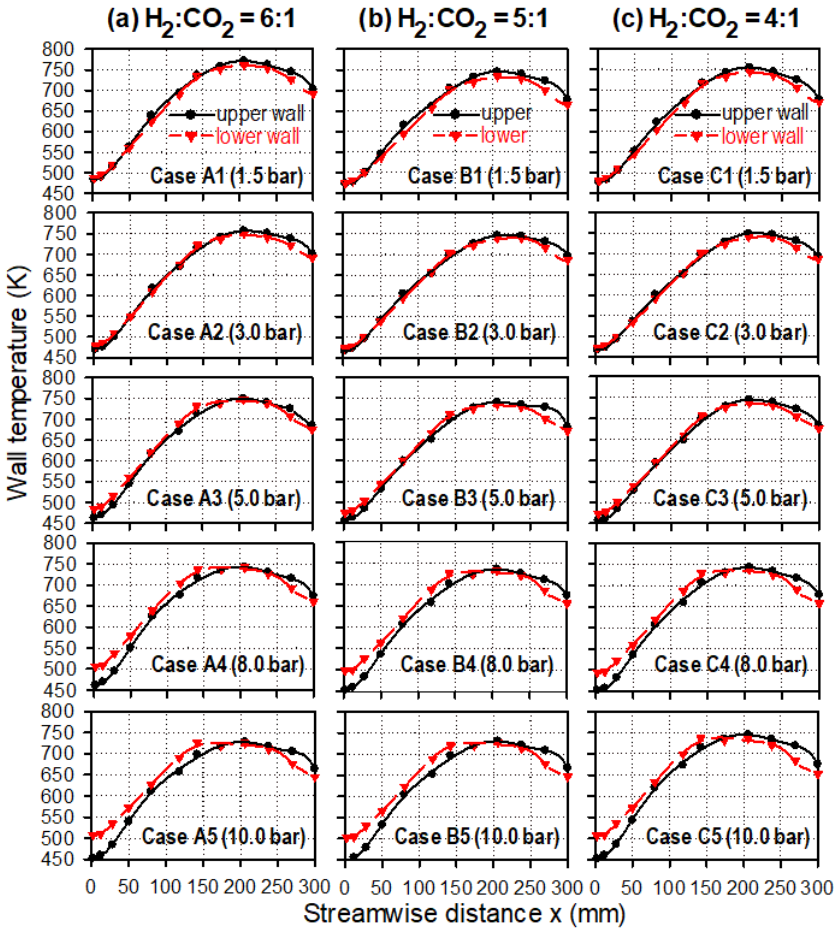

Fig. 4.4. Thermocouple-measured upper wall (circles) and lower wall (triangles) temperatures for all investigated cases in Table 2.

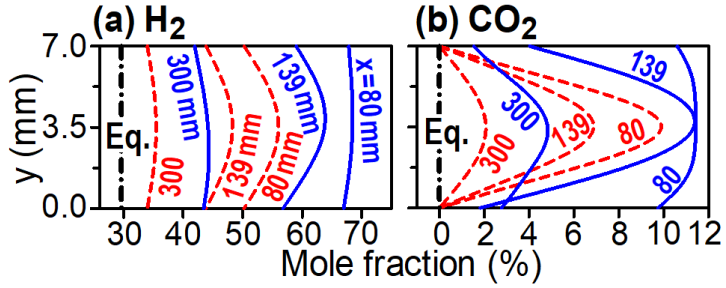

Fig. 4.5. (a) H_2 and (b) CO_2 mole fraction profiles for Case A5 (H_2:CO_2 = 6, p = 10 bar) at x = 80, 139 and 300 mm. Solid lines: detailed chemistry, dashed lines: transport limited (TL) simulations. Vertical lines (marked Eq.) is the computed equilibrium at the outlet.

The differences between Raman measurements and simulations, although modest, were larger at higher inlet H_2:CO_2 ratios and lower pressures. The first factor could be principally attributed to the preferential diffusion of H_2, which substantially altered the local H_2:CO_2 ratio at the catalytic walls. Figure 4.6 shows such ratios at the upper wall (y = 7 mm) for 1.5 bar and 10 bar. Over the Raman measuring extent 34 ≤ x ≤ 139 mm, the local ratios at 1.5 bar were as high as 6.3, 7.8 and 12.9 for Cases C1, B1 and A1, respectively. At 10 bar, the ratios were as high as 14. Farther downstream (x > 139 mm) the wall ratios continued to increase, reaching at 1.5 bar and 10 bar 2-3 times and 5-8 times the inlet ratios, respectively. Hence, the demands for a kinetic scheme become quite high, as it ought to work for effective H_2:CO_2 surface ratios substantially broader than the nominal inlet ones. Therefore, in many kinetic studies the potential presence of non-isothermicity (negating the common isothermal assumption, as discussed in [13]) can be compounded by additional strong preferential diffusion effects. This is because a fully kinetically controlled reactor operation without any transport limitations cannot be easily achieved, especially at elevated catalyst temperatures.

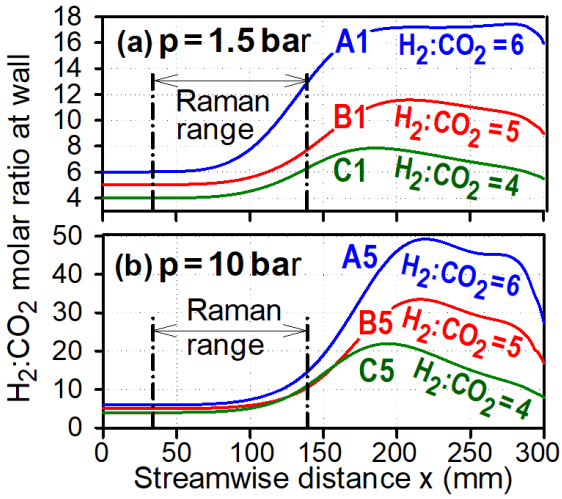

Fig. 4.6. Simulated H_2:CO_2 molar ratios at the upper wall: (a) Cases A1, B1 and C1 and (b) Cases A5, B5 and C5.

Comparisons of GC-measured and simulated methane volumetric contents in the dry exhaust gas are shown in Fig. 4.7, together with the corresponding transport-limited (TL) simulations and the full

equilibrium calculations at the outlet temperature. For all H_2:CO_2 ratios, the methane production increased with increasing pressure. The exception at H_2:CO_2 = 6 between Cases A4 and A5 was due to the consistently lower wall temperatures of the latter case (by up to 19 K, see Fig. 4.4). In agreement to the foregoing comparisons of local Raman measurements and simulations, the methane in the exhaust was overpredicted at H_2:CO_2 = 6, with the deviations decreasing as the pressure increased (up to 16.2% at 1.5 bar and up to 3.2% at 10 bar). CO production was favored at lower H_2:CO_2 ratios and lower pressures. The maximum measured CO in the exhaust was 0.68% for Case C1. Over the Raman measuring axial extent, CO was too low (the maximum in the simulations was 0.28% per volume on a wet basis, for Case C1 at x = 139 mm and only near the walls), such that it was not detectable by the Raman technique.

The chemical pathways for methane production are analyzed with the reaction flux diagram in Fig. 4.8, pertaining to x = 139 mm at the upper wall of Case B3. The main pathways were the same for all cases, irrespective of H_2:CO_2 ratio, temperature, or pressure. Methane was produced from surface carbon C(s) via successive hydrogenation to CH(s), CH_2 (s), CH_3(s), CH_4(s) and desorption of the latter to gaseous CH_4. C(s) was formed by carboxyl COOH(s) via reaction of H(s) with CO_2(s) in S35-S36 (for reaction numbering, see Table 4.2(a)), followed by dissociation of COOH(s) to CO(s) (S37-S38) and finally H assisted dissociation of CO(s) to C(s) (S15-S16). The routes via formyl HCO(s) (S39-S40) and via direct CO_2(s) dissociation (S11-S12) were negligible.

A quantify of key interest is the pressure dependence of the CO_2 methanation. In a first step, the detailed surface reaction mechanism was scaled by multiplying all reaction pre-exponentials of Table 4.2(a) by a given factor such that the simulations best reproduced the Raman measurements and the exhaust gas compositions (the attained agreement was within 12% for all cases). The multiplicative factors for each case are provided in Table 4.1. The scaled detailed mechanisms were then employed in a Surface Perfectly Stirred Reactor (SPSR) [15] model to compute the methane production. The SPSR species conservation equations were:

$$(Y_{k,out} - Y_{k,in}) = (\tau/\rho)(S/V)\dot{s}_k, \tag{4.1}$$

with Y_k and $\dot{s}_k$ the mass fraction and reaction rate of the *k*-th gaseous species, respectively; τ, ρ and *S*/*V* were the residence time, density, and surface-to-volume ratio, respectively. A global power-law methanation reaction was considered, $\dot{s}_k = AT^c exp(-E/RT)[H_2]^a[CO_2]^b$, as in [23]. By using in the simulations: a) a fixed (*S*/*V*), and b) a constant ratio (τ/ρ) when the pressure and H_2/CO_2 compositions were altered, Eq. (4.1) yielded:

$$Y_{CH4,out} \sim T^c exp(-E_a/RT)[H_2]^a[CO_2]^b. \tag{4.1a}$$

Using *S*/*V* = 2.85 cm^{-1} (equal to the channel surface to volume ratio) and τ = 0.44 s for Case A1 (equal to the channel residence time at 1.5 bar), the global step reproduced within 24% the scaled detailed chemistry SPSR results over the temperature range 520-680 K (see Fig. 4.9), when *a* = 0.19 and *b* = 0.22. Moreover, the fitted activation energy was E_a = 68 kJ/mole, a value close to the 61 kJ/mole reported for the higher pressure range 10.5-17.0 bar in [23], while *c* = -0.68. Hence, for the design of practical reactors **a realistic power dependence ~p^{a+b} = $p^{0.41}$** can be used to assess the methane production.

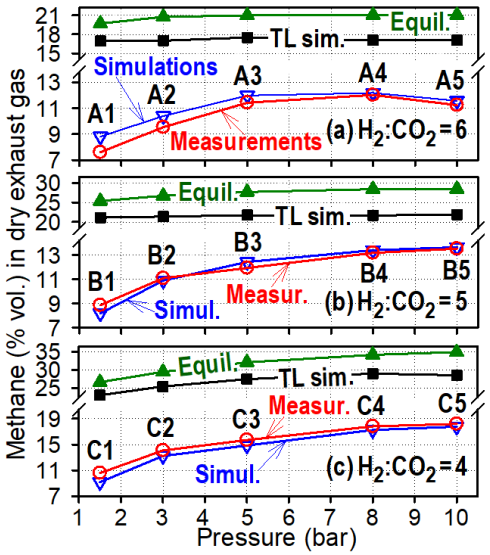

Fig. 4.7. Methane (% vol.) in the dry exhaust gas for all cases. Detailed chemistry (lower triangles) and transport limited TL (squares) simulations, GC measurements (circles) and equilibrium (Equil.) at the outlet temperature (upper triangles).

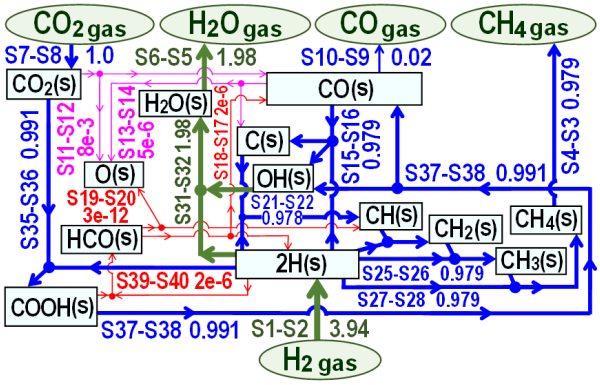

Fig. 4.8. Reaction flux for Case B3 at x = 139 mm and at the upper wall (local wall temperature 690 K). Main pathways are shown, normalized by the net adsorption of CO_2.

Case A1 (H_2:CO_2 = 6, p=1.5 bar)	Case A2 (H_2:CO_2 = 6, p=3 bar)	Case A3 (H_2:CO_2 = 6, p=5 bar)	Case A4 (H_2:CO_2 = 6, p=8 bar)	Case A5 (H_2:CO_2 = 6, p=10 bar)
0.75	0.78	0.85	0.90	0.96
Case B1 (H_2:CO_2 = 5, p=1.5 bar)	Case B2 (H_2:CO_2 = 5, p=3 bar)	Case B3 (H_2:CO_2 = 5, p=5 bar)	Case B4 (H_2:CO_2 = 5, p=8 bar)	Case B5 (H_2:CO_2 = 5, p=10 bar)
1.14	1.05	0.90	0.95	0.97
Case C1 (H_2:CO_2 = 4, p=1.5 bar)	Case C2 (H_2:CO_2 = 4, p=3 bar)	Case C3 (H_2:CO_2 = 4, p=5 bar)	Case C4 (H_2:CO_2 = 4, p=8 bar)	Case C5 (H_2:CO_2 = 4, p=10 bar)
1.28	1.15	1.12	1.10	1.08

Table 4.1. Multiplicative factors for the pre-exponentials in the reaction mechanism of Table 4.2.

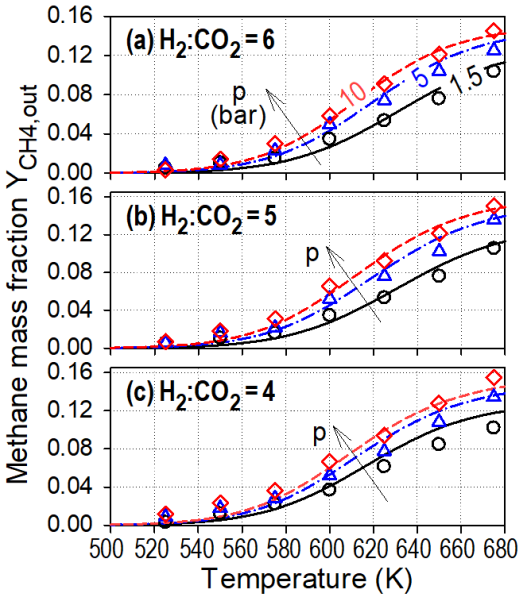

Fig. 4.9. SPSR simulations: comparisons between scaled detailed chemistry simulations (solid lines) and global-step simulations (symbols). Pressures of 1.5 bar (solid lines, circles), 5.0 bar (dashed-dotted lines, upper triangles), 10 bar (dashed lines, diamonds). The differences between the two types of simulations is within 24%, when the methane outlet mass fractions are $Y_{CH4,out} > 0.02$.

4.1.2 High-pressure applicability of PSI's derived methanation mechanism

An atmospheric-pressure, two-step reaction mechanism has been developed in the past at PSI (Witte-Schildhauer et al. [24]). The mechanism consists of the reactions shown in Eq. (4.2) (Water Gas Shift, WGS) and Eq. (4.3) (methanation). A main goal of the BfE project is to test the validity of this mechanism at elevated pressure and to propose (if necessary) corrections for high pressures.

$$r_{WGS}^{BFB} = \frac{k_{WGS}\left(K_a p_{CO} p_{H2O} - \frac{p_{CO2} p_{H2}}{K_{eq,WGS}}\right)}{p_{H2}^{0.5}\left(1+K_c p_{CO}^{d} p_{H2}^{e} + K_{OH} p_{H2O} p_{H2}^{-0.5}\right)^2}, \tag{4.2}$$

and for the methanation reaction

$$r_{Meth}^{BFB} = \frac{k_{Meth} K_c p_{CO}^{a} p_{H2}^{b}\left(1-\frac{p_{CH4} p_{H2O}}{K_{eq,Meth} p_{CO} p_{H2}^{3}}\right)^{c}}{\left(1+K_c p_{CO}^{d} p_{H2}^{e} + K_{OH} p_{H2O} p_{H2}^{-0.5}\right)^2} \tag{4.3}$$

Figure 4.10 provides SPSR simulations in an SPSR for H_2:CO_2 = 4, for temperatures 500-700 K. Simulations are shown for pressures of 1.5, 5 and 10 bar, with two mechanisms: a) the Deutschmann mechanism of the foregoing section (using the scaling factors of Table 4.1) which reproduced the current experiments, and b) the two-step mechanism of PSI by Witte-Schildhauer.

It is evident in from Fig. 4.10 that while the 1.5 bar simulations of both schemes can be matched relatively well, the Witte-Schildhauer mechanism significantly overpredicted the methane production at 5 and 10 bar. This behavior is typical to catalytic reaction mechanisms that were developed for a specific pressure. An extrapolation of these mechanisms to pressures significantly higher than the nominal one,

typically leads to an overprediction of the reaction rates, such that a “restraining” factor is usually needed to ensure satisfactory high-pressure performance [22]. To this direction, and as described in [22], the reaction rate constants k_{WGS} and k_{Meth} in Eqs. (4.2) and (4.3) are multiplied with a pressure-dependent function $F(p)$ (same for both reaction steps). An iterative optimization leads to:

$F(p) = [p/(1.5\ \mathrm{bar})]^{(\alpha p+b)}$ with $\alpha = 0.11$ and $b = -1.31$. (4.4)

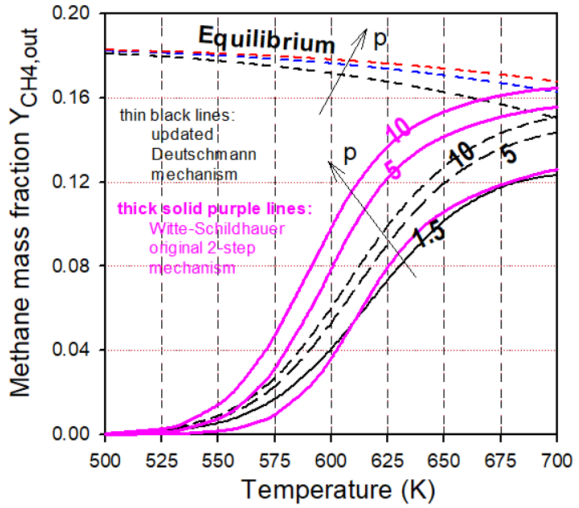

Fig. 4.10. SPSR simulations for H_2:CO_2 = 4 and pressures of 1.5, 5 and 10 bar: comparisons between detailed chemistry simulations of the scaled Deutschmann mechanism (black lines) and the two-step Witte-Schildhauer mechanism (purple lines).

Simulations with the updated two-step Witte-Schildhauer mechanism (Eqs. 4.2-4.4) are shown in Fig. 4.11.

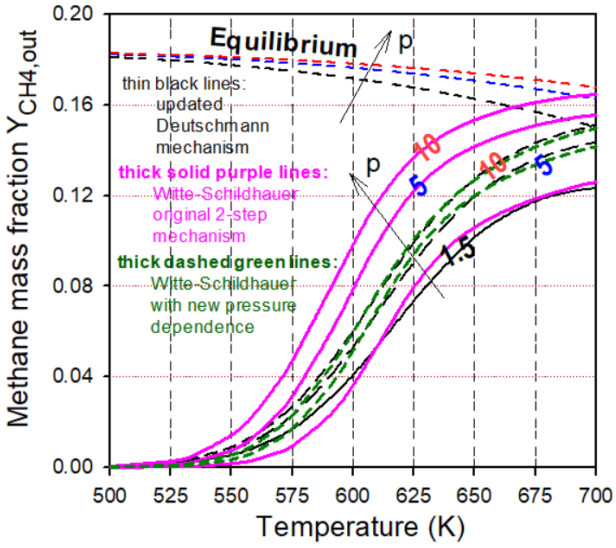

Fig. 4.11. SPSR simulations for H_2:CO_2 = 4 and pressures of 1.5, 5 and 10 bar. Comparisons between detailed chemistry simulations of the scaled Deutschmann mechanism (black lines), the original two-step Witte-Schildhauer mechanism (purple lines) and the updated Witte-Schildhauer mechanism (green lines).

While the p=1.5 bar results remain unchanged, the p=5 and 10 bar new results (dashed green lines in Fig. 4.11) closely match the updated Deutschmann mechanism. Hence, an appropriate two-step mechanism for CO_2 methanation has been developed with the aid of the present experiments and simulations.

Hence, Task 2.1 and Milestone 3 (simulation of experiments, simulation tool tested) have been fulfilled.

Task 2.2 and Milestone 4 (validated catalytic chemistry) have been accomplished. An updated two-step reaction mechanism has been proposed, validated for pressures up to 10 bar.

4.1.3 Task 2.3. Theoretical comparison of Ni/Al_2O_3 and Rh catalysts

Goal of this task is to make basic theoretical comparisons between Ni and Rh catalysts in their capacity to promote CO_2 methanation. For CO_2 methanation on Ni, the catalytic reaction mechanism from Schmider and Deutschmann was used [13], while for CO_2 methanation on Rh a mechanism again from Deutschmann's group was used [14]. It is clarified that the Ni-mechanism [13] was developed for both CO and CO_2 methanation on Ni and has been validated against many experimental data (at least for p = 1 bar). On the other hand, the Rh mechanism [14] has been mainly validated for methane steam/dry reforming and partial oxidation, but not systematically for CO_2 methanation. The two reaction mechanisms are provided in Table 4.2. The Ni mechanism has 42 reactions and 14 surface species, while the Rh mechanism has 46 reactions and 13 surface species.

The simulation tool used for this task is the Surface Perfectly Stirred Reactor (SPSR) of Chemkin [15]. Detailed chemistry simulations were carried out by keeping all parameters the same but changing the reactor temperature (in the range 550 - 800 K, encompassing the experimental temperatures in our plate reactor). The SPSR inlet composition was H_2:CO_2 = 6:1 (no N_2 added) and the pressure was p = 5 bar. The SPSR residence time was fixed to 0.2 s and the surface to volume ratio to 40 cm^{-1}.

Simulation results are shown in Fig. 4.12, providing the SPSR outlet mole fractions of the reactants (H_2 and CO_2), the main products (CH_4 and CO_2) and the by-product CO. The following are the main conclusions from the comparisons in Fig. 4.12:

- Ni has higher CH_4 yields (Fig. 4.12(c)) than Rh. Ni has also higher conversions of H_2 and CO_2 (Figs. 4.12(a, b)), with the exception of the narrow temperature window 550-600 K.
- Rh has higher production of the undesirable by-product CO, which comprises ca. 1% vol. of the exhaust gas, irrespective of pressure.
- Over the investigated temperature range 550-800 K, the H_2 and CO_2 conversions and the CH_4 production are kinetically limited and not equilibrium limited (see also the equilibrium predictions in Fig. 4.12). Hence, a good catalyst is important to accelerate the speed of methanation kinetics.

Overall, Ni is shown superior to Rh for CO_2 methanation over the studied temperature range 550-800 K, as it gives the highest reactant conversions and the highest methane yields.

Hence, Task 2.3 (theoretical comparison of Ni/Al_2O_3 and Rh catalysts) has been fulfilled.

(a) Ni mechanism

```
CKLIB:  Chemical Kinetics Library
        CHEMKIN-II Version 4.5, January 1995
        DOUBLE PRECISION

SPECIES                 MOLECULAR                          ELEMENT COUNT
CONSIDERED              WEIGHT        Density    Nsites    C  H  O  N  Ni

Gas phase species:
  1. H2                  2.01594                          0  2  0  0  0
  2. CH4                16.04303                          1  4  0  0  0
  3. H2O                18.01534                          0  2  1  0  0
  4. CO2                44.00995                          1  0  2  0  0
  5. CO                 28.01055                          1  0  1  0  0
  6. N2                 28.01340                          0  0  0  2  0

SITE: Ni_SURFACE                    0.271E-08 moles/cm**2
  7. Ni(S)              58.71000                1         0  0  0  0  1
  8. CH4(S)             74.75303                1         1  4  0  0  1
  9. H2O(S)             76.72534                1         0  2  1  0  1
 10. CO2(S)            102.71995                1         1  0  2  0  1
 11. CO(S)              86.72055                1         1  0  1  0  1
 12. CH(S)              71.72912                1         1  1  0  0  1
 13. CH2(S)             72.73709                1         1  2  0  0  1
 14. CH3(S)             73.74506                1         1  3  0  0  1
 15. COOH(S)           103.72792                1         1  1  2  0  1
 16. HCO(S)             87.72852                1         1  1  1  0  1
 17. OH(S)              75.71737                1         0  1  1  0  1
 18. H(S)               59.71797                1         0  1  0  0  1
 19. O(S)               74.70940                1         0  0  1  0  1
 20. C(S)               70.72115                1         1  0  0  0  1

     SURFACE REACTIONS CONSIDERED                    (k = A T**b exp(-E/RT))
                                                        A          b          E
  1. H2+2NI(S)=>H(S)+H(S)                           1.66E-02     0.0        0.0
       Coefficients are sticking parameters...
  2. H(S)+H(S)=>2NI(S)+H2                           4.58E+21    -0.1       96.1
  3. CH4+NI(S)=>CH4(S)                              1.06E-02     0.0        0.0
       Coefficients are sticking parameters...
  4. CH4(S)=>NI(S)+CH4                              2.79E+15     0.1       37.0
  5. H2O+NI(S)=>H2O(S)                              1.16E-01     0.0        0.0
       Coefficients are sticking parameters...
  6. H2O(S)=>NI(S)+H2O                              2.04E+12     0.0       61.0
  7. CO2+NI(S)=>CO2(S)                              6.29E-05     0.0        0.0
       Coefficients are sticking parameters...
  8. CO2(S)=>NI(S)+CO2                              4.99E+07     0.0       25.8
  9. CO+NI(S)=>CO(S)                                3.74E-01     0.0        0.0
       Coefficients are sticking parameters...
 10. CO(S)=>NI(S)+CO                                1.14E+12    -0.1      112.0
       Coverage parameters for species CO(S)
         0.000E+00 0.000E+00-5.000E+01
 11. CO2(S)+NI(S)=>O(S)+CO(S)                       1.60E+23    -1.0       89.3
 12. O(S)+CO(S)=>CO2(S)+NI(S)                       5.81E+19     0.0      123.6
       Coverage parameters for species CO(S)
         0.000E+00 0.000E+00-5.000E+01
 13. CO(S)+NI(S)=>C(S)+O(S)                         2.36E+14     0.0      116.2
       Coverage parameters for species CO(S)
         0.000E+00 0.000E+00-5.000E+01
 14. C(S)+O(S)=>CO(S)+NI(S)                         2.54E+18     0.0      148.1
       Coverage parameters for species C(S)
         0.000E+00 0.000E+00-1.050E+02
 15. CO(S)+H(S)=>C(S)+OH(S)                         3.04E+19    -0.2      105.3
       Coverage parameters for species CO(S)
         0.000E+00 0.000E+00-5.000E+01
 16. C(S)+OH(S)=>CO(S)+H(S)                         2.18E+18     0.1       62.8
       Coverage parameters for species C(S)
         0.000E+00 0.000E+00-1.050E+02
 17. CO(S)+H(S)=>HCO(S)+NI(S)                       6.82E+21    -1.0      132.1
 18. HCO(S)+NI(S)=>CO(S)+H(S)                       2.18E+20     0.0        0.2
       Coverage parameters for species CO(S)
         0.000E+00 0.000E+00 5.000E+01
 19. HCO(S)+NI(S)=>CH(S)+O(S)                       5.10E+15     0.0       81.7
 20. CH(S)+O(S)=>HCO(S)+NI(S)                       3.42E+19     0.0      110.2
 21. C(S)+H(S)=>CH(S)+NI(S)                         1.33E+24    -0.5      157.7
       Coverage parameters for species C(S)
         0.000E+00 0.000E+00-1.050E+02
 22. CH(S)+NI(S)=>C(S)+H(S)                         2.63E+22     0.5       22.3
 23. CH(S)+H(S)=>CH2(S)+NI(S)                       3.21E+25    -0.1       81.1
 24. CH2(S)+NI(S)=>CH(S)+H(S)                       6.16E+24     0.1       95.2
 25. CH2(S)+H(S)=>CH3(S)+NI(S)                      7.78E+22     0.0       59.5
 26. CH3(S)+NI(S)=>CH2(S)+H(S)                      6.16E+24     0.0       95.9
 27. CH3(S)+H(S)=>CH4(S)+NI(S)                      3.63E+21     0.0       65.7
 28. CH4(S)+NI(S)=>CH3(S)+H(S)                      6.16E+21     0.0       53.6
 29. O(S)+H(S)=>OH(S)+NI(S)                         3.16E+24    -0.2      104.2
 30. OH(S)+NI(S)=>O(S)+H(S)                         7.70E+19     0.2       29.8
 31. OH(S)+H(S)=>H2O(S)+NI(S)                       2.34E+20     0.1       44.1
 32. H2O(S)+NI(S)=>OH(S)+H(S)                       2.91E+21    -0.1       90.4
 33. OH(S)+OH(S)=>O(S)+H2O(S)                       1.01E+20     0.3       95.1
 34. O(S)+H2O(S)=>OH(S)+OH(S)                       1.89E+25    -0.3      215.8
 35. CO2(S)+H(S)=>COOH(S)+NI(S)                     1.29E+25    -0.5      117.2
 36. COOH(S)+NI(S)=>CO2(S)+H(S)                     1.29E+20     0.5       33.8
 37. COOH(S)+NI(S)=>OH(S)+CO(S)                     6.03E+23    -0.2       54.4
 38. OH(S)+CO(S)=>COOH(S)+NI(S)                     1.45E+21     0.2       97.6
       Coverage parameters for species CO(S)
         0.000E+00 0.000E+00-5.000E+01
 39. COOH(S)+H(S)=>HCO(S)+OH(S)                     4.22E+23    -1.1      104.7
 40. HCO(S)+OH(S)=>COOH(S)+H(S)                     3.25E+19     0.2       16.1
 41. CO(S)+CO(S)=>C(S)+CO2(S)                       6.31E+13     0.5      241.7
       Coverage parameters for species CO(S)
         0.000E+00 0.000E+00-1.000E+02
 42. C(S)+CO2(S)=>CO(S)+CO(S)                       1.88E+21    -0.5      239.3
       Coverage parameters for species C(S)
         0.000E+00 0.000E+00-1.050E+02
```

(b) Rh mechanism

```
CKLIB:  Chemical Kinetics Library
        CHEMKIN-II Version 4.5, January 1995
        DOUBLE PRECISION

SPECIES                 MOLECULAR                          ELEMENT COUNT
CONSIDERED              WEIGHT        Density    Nsites    C  H  O  N  Rh

Gas phase species:
  1. H2                  2.01594                          0  2  0  0  0
  2. CH4                16.04303                          1  4  0  0  0
  3. H2O                18.01534                          0  2  1  0  0
  4. CO2                44.00995                          1  0  2  0  0
  5. CO                 28.01055                          1  0  1  0  0
  6. N2                 28.01340                          0  0  0  2  0

SITE: RH_SURFACE                    0.272E-08 moles/cm**2
  7. Rh(s)              102.90500                1         0  0  0  0  1
  8. H2O(s)             120.92034                1         0  2  1  0  1
  9. H(s)               103.91297                1         0  1  0  0  1
 10. OH(s)              119.91237                1         0  1  1  0  1
 11. CO(s)              130.91555                1         1  0  1  0  1
 12. C(s)               114.91615                1         1  0  0  0  1
 13. CH3(s)             117.94006                1         1  3  0  0  1
 14. CH2(s)             116.93209                1         1  2  0  0  1
 15. CH(s)              115.92412                1         1  1  0  0  1
 16. CH4(s)             118.94803                1         1  4  0  0  1
 17. O(s)               118.90440                1         0  0  1  0  1
 18. CO2(s)             146.91495                1         1  0  2  0  1
 19. COOH(s)            147.92292                1         1  1  2  0  1

BULK: BULK1
 20. Rh(b)              102.90500 0.314E+02 g/cm**3         0  0  0  0  1

     SURFACE REACTIONS CONSIDERED                    (k = A T**b exp(-E/RT))
                                                        A          b          E
  1. H2+Rh(S)+Rh(S)=>H(S)+H(S)                      3.00E-02     0.0        0.0
       Coefficients are sticking parameters...
  2. H2O+Rh(S)=>H2O(S)                              1.00E-01     0.0        0.0
       Coefficients are sticking parameters...
  3. CO2+Rh(S)=>CO2(S)                              4.80E-02     0.0        0.0
       Coefficients are sticking parameters...
  4. CO+Rh(S)=>CO(S)                                4.57E-01     0.0        0.0
       Coefficients are sticking parameters...
  5. CH4+Rh(S)=>CH4(S)                              1.30E-02     0.0        0.0
       Coefficients are sticking parameters...
  6. H(S)+H(S)=>Rh(S)+Rh(S)+H2                      5.57E+19     0.2       69.7
  7. H2O(S)+Rh(S)=>OH(S)+H(S)                       6.96E+14    -0.3       45.0
  8. CO(S)+Rh(S)=>O(S)+C(S)                         1.30E+13     0.3      134.1
       Coverage parameters for species CO(S)
         0.000E+00 0.000E+00-4.700E+01
  9. CO2(S)+Rh(S)=>O(S)+CO2                         3.52E+11     0.3       20.5
 10. CH4(S)+Rh(S)=>H(S)+CH3                         1.52E+13    -0.1       26.0
 11. O(S)+H(S)=>OH(S)+Rh(S)                         8.83E+21     0.0       73.4
 12. OH(S)+Rh(S)=>O(S)+H(S)                         1.00E+21     0.0       48.0
 13. OH(S)+H(S)=>H2O(S)+Rh(S)                       1.74E+22    -0.1       41.7
 14. H2O(S)+Rh(S)=>OH(S)+H(S)                       5.41E+22     0.1       90.2
 15. OH(S)+OH(S)=>O(S)+H2O(S)                       5.74E+20    -0.1      121.6
 16. O(S)+H2O(S)=>OH(S)+OH(S)                       1.57E+23     0.1      203.4
 17. O(S)+C(S)=>CO(S)+Rh(S)                         1.17E+22     0.0       92.1
       Coverage parameters for species C(S)
         0.000E+00 0.000E+00-1.200E+02
 18. CO(S)+Rh(S)=>C(S)+O(S)                         6.39E+21     0.0      174.8
       Coverage parameters for species CO(S)
         0.000E+00 0.000E+00-4.700E+01
 19. O(S)+CO(S)=>CO2(S)+Rh(S)                       6.18E+21     0.0      130.0
       Coverage parameters for species CO(S)
         0.000E+00 0.000E+00-4.700E+01
 20. CO2(S)+Rh(S)=>O(S)+CO(S)+Rh(S)                 5.75E+22    -0.2      106.5
 21. CO(S)+OH(S)=>COOH(S)+Rh(S)                     2.92E+20     0.0       55.3
       Coverage parameters for species CO(S)
         0.000E+00 0.000E+00-4.700E+01
 22. COOH(S)+Rh(S)=>CO(S)+OH(S)                     2.74E+21     0.0       48.4
 23. COOH(S)+Rh(S)=>CO2(S)+H(S)                     1.14E+19     0.2        5.6
 24. CO2(S)+H(S)=>COOH(S)+Rh(S)                     1.14E+20    -0.2       14.5
 25. COOH(S)+H(S)=>CO(S)+H2O(S)                     6.00E+19    -0.2       33.6
 26. CO(S)+H2O(S)=>COOH(S)+H(S)                     2.26E+19     0.1       97.1
       Coverage parameters for species CO(S)
         0.000E+00 0.000E+00-4.700E+01
 27. CO(S)+OH(S)=>CO2(S)+H(S)                       3.07E+19     0.0       92.9
       Coverage parameters for species CO(S)
         0.000E+00 0.000E+00-4.700E+01
 28. CO2(S)+H(S)=>CO(S)+OH(S)                       2.50E+21    -0.3       84.8
 29. C(S)+OH(S)=>CO(S)+H(S)                         4.92E+20     0.1       30.0
       Coverage parameters for species C(S)
         0.000E+00 0.000E+00-1.200E+02
 30. CO(S)+H(S)=>C(S)+OH(S)                         3.24E+21    -0.1      138.3
       Coverage parameters for species CO(S)
         0.000E+00 0.000E+00-4.700E+01
 31. CH4(S)+Rh(S)=>CH3(S)+H(S)                      4.62E+21     0.1       72.3
 32. CH3(S)+H(S)=>CH4(S)+Rh(S)                      2.14E+21    -0.1       46.8
 33. CH3(S)+Rh(S)=>CH2(S)+H(S)                      1.97E+24     0.1      107.6
 34. CH2(S)+H(S)=>CH3(S)+Rh(S)                      1.97E+22    -0.1       39.5
 35. CH2(S)+Rh(S)=>CH(S)+H(S)                       1.27E+24     0.1      115.4
 36. CH(S)+H(S)=>CH2(S)+Rh(S)                       1.07E+22    -0.1       52.6
 37. CH(S)+Rh(S)=>C(S)+H(S)                         1.46E+20     0.1       23.1
 38. C(S)+H(S)=>CH(S)+Rh(S)                         1.12E+23    -0.1      170.7
       Coverage parameters for species C(S)
         0.000E+00 0.000E+00-1.200E+02
 39. CH4(S)+O(S)=>CH3(S)+OH(S)                      3.47E+23     0.1       77.7
 40. CH3(S)+OH(S)=>CH4(S)+O(S)                      1.92E+22    -0.1       96.9
 41. CH3(S)+O(S)=>CH2(S)+OH(S)                      4.79E+24     0.0      116.5
 42. CH2(S)+OH(S)=>CH3(S)+O(S)                      2.86E+21     0.0       20.9
 43. CH2(S)+O(S)=>CH(S)+OH(S)                       4.79E+24     0.0      141.8
 44. CH(S)+OH(S)=>CH2(S)+O(S)                       2.86E+21     0.0       53.4
 45. CH(S)+O(S)=>C(S)+OH(S)                         5.01E+20     0.0       26.8
 46. C(S)+OH(S)=>CH(S)+O(S)                         2.73E+22     0.0      148.8
       Coverage parameters for species C(S)
         0.000E+00 0.000E+00-1.200E+02
```

Table 4.2. CO_2 methanation reaction mechanisms: (a) on Ni (from [13]), and (b) on Rh (from [14]).

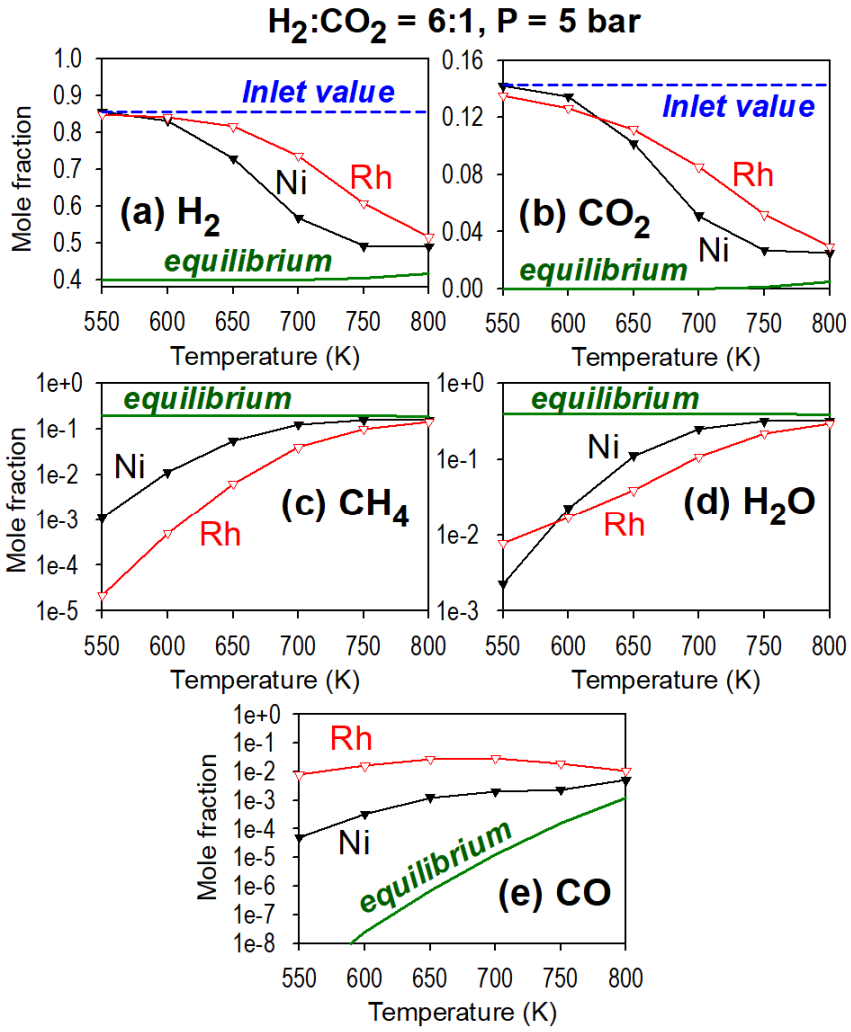

Fig. 4.12. Comparisons of CO_2 methanation on Ni and Rh catalysts, using Surface Perfectly Stirred Reactor (SPSR) simulations. Plots of outlet species mole fractions for an inlet mixture with H_2:CO_2 = 6 and pressure p = 5 bar.

4.2 WP5: Microscopic LB model and simulations

This WP comprises the SNSF-funded PhD Thesis of Mr. M. Khatoonabadi.

4.2.1 Task 5.1. Development of two-phase particle LB model

The biogas methanation occurring inside and around a porous catalytic Ni/Al_2O_3 particle is modeled in detail with the LB (Lattice Boltzmann) method. For this purpose, several developments in the catalytic reaction model are required. A pre-existing catalytic boundary model was further advanced to account for arbitrary reaction-to-diffusion ratios or, in other words, for arbitrary Damköhler numbers (i.e. encompassing kinetic-controlled to transport-controlled regimes). In addition, the old catalytic model failed to accurately predict non-equimolar reactions due to the increase/decrease in velocity after the streaming LB process. This was an important limitation, as the methanation reactions are strongly non-equimolar. A correction term is developed to ensure a constant pressure at the catalytic wall. We show that the correction term is also the corresponding term used in other computational fluid dynamics (CFD) boundary conditions. Finally, the catalytic model is further extended to incorporate velocity slip and concentration jump since the Knudsen number (ratio of the molecular mean free path to the characteristic length) can reach as high as 0.1 in small pores inside particles. The simulation results show that the effect of concentration jump can be neglected under our experimental conditions.

The developed models are then utilized for the three-dimensional simulations of porous catalytic particles. The geometry of a real porous particle obtained from X-ray tomography (XTM) is reconstructed with one-micron resolution. The numerical simulations indicate that the spatial homogeneity of pores, which is a common assumption in continuum modeling, is violated and the small and large pores are distributed inhomogeneously. The macropores, in turn, might considerably alter the flow inside the particle, although no noticeable change in catalytic conversion of the particle is observed. The pore-scale simulation results on artificial spherical porous particles show that the effect of the outer surface is non-negligible under moderate and high Damköhler numbers. Moreover, the distribution of fuel concentration around the particle varies, and this must be considered in continuum models to have accurate predictions. This section structured as follows:

- The multicomponent gas mixture LB model is introduced briefly, followed by the catalytic diffusive boundary condition.
- The catalytic model developments for non-equimolar reactions, high Damköhler numbers, and velocity and concentration jumps at the surface of the catalyst are presented.
- Simulation results using the LB method follow:
    - First, the developed numerical LB code is employed for the simulation of cross-flows in a gas diffusion layer (GDL) of a micro polymer electrolyte fuel cell (PEFC). This gives credence to the 3D complex porous geometry LB model characteristics. This part is non-reactive.
    - Second, the validation of the developed catalytic reaction models against reactive CFD results are presented and discussed.

Having established the LB model, the geometry of a real porous particle in the CO methanation reaction will be simulated.

4.2.1.1 Mathematical model

The kinetic equation for each species is written as follows:

$$\partial_t f_{ji} + c_{ji\alpha}\partial_\alpha f_{ji} = -\frac{1}{\tau_{j1}}\left(f_{ji} - f_{ji}^{*}\right) - \frac{1}{\tau_{j2}}\left(f_{ji}^{*} - f_{ji}^{eq}\right) + \Psi_{ji}, \tag{4.5}$$

where f_{ji} is the population distribution for species j in direction i. Considering a 3D lattice with 27 discrete velocities (D3Q27), i runs from 0 to 26. In addition, for all available simulations, there are four species involved in the chemical reaction, CO, H_2, CH_4 and H_2O ($j = 1,2,3,4$). Two relaxation times $\tau_{j1}$and τ_{j2} are linked to the species' viscosity and diffusion coefficients, respectively. $c_{ji\alpha}$ in Eq. (4.5) is the lattice velocity for species j. Each species has a different molar mass M_j and speed of sound c_j. Ψ_{ji} in Eq. (4.5) is a correction term to recover momentum conservation. The equilibrium functions for species f_{ji}^{*} and the gas mixture f_{ji}^{eq} are calculated as follows:

$$f_{ji}^{*}(\rho_j, u_j) = f_{ji}^{eq}(\rho_j, u_{j\alpha}) = \rho_j \prod_{\alpha=x,y,z} \frac{2c_{Li\alpha}^2 - 1}{2c_{Li\alpha}^2}\left(c_{Li\alpha}^2 - 1 + \sqrt{M_j}c_{Li\alpha}^2 u + M_j u^2 + T\right). \tag{4.6}$$

where $c_{Li\alpha}$ is the speed of sound of the lightest species. The macroscopic properties such as density, velocity, and pressure can be calculated from the distribution function.

The catalytic boundary condition initially introduced earlier in our group by Arcidiacono et al. [16] was constructed based on the diffusive boundary condition. The incoming particle distribution function f_{ji}^{in} (see Fig. 4.13) is obtained as:

$$f_{ji}^{in} = f_{ji}^{eq}(\rho_{jw}, u_\alpha)\frac{\sum_{i=0, f_{ji}c_{ji\alpha}n_\alpha<0}^{i=26}\left|f_{ji}c_{ji\alpha}n_\alpha\right| + S_j}{\sum_{i=0, f_{ji}c_{ji\alpha}n_\alpha>0}^{i=26}\left|f_{ji}^{eq}(\rho_{jw}, u_\alpha)c_{ji\alpha}n_\alpha\right|}, \tag{4.7}$$

where n_α is the normal direction to the catalytic surface. ρ_{jw} is the species density at the catalytic wall, and S_j is the catalytic reaction rate calculated as $S_j = b_j M_j k C_{dw}$ for a first-order reaction. b_j refers to the stoichiometric coefficient and k is the reaction rate coefficient. C_{dw} is the concentration of the deficient species at the reactive wall. Since the concentrations of species are unknown at the catalytic wall, an iteration scheme is required; therein, a value is selected from the previous time step as a first guess and it is corrected after some iterations until convergence is reached.

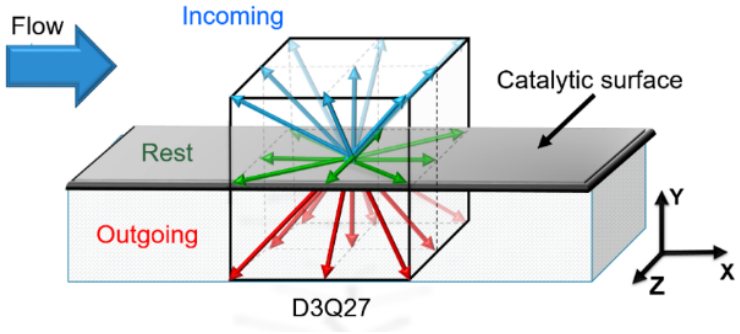

Fig. 4.13. Schematic of the catalytic boundary condition.

4.2.1.2 Development of the new catalytic reactive boundary condition

As the model of Eq. (4.7) is based on local quantities at the reactive wall, it suffers from issues of accuracy at very high reaction rates. This is manifested by a negative numerator in Eq. (4.7) when

$\sum_{i=0,f_{ji}c_{ji\alpha}n_\alpha<0}^{i=26}\left|f_{ji}c_{ji\alpha}n_\alpha\right| < S_j$, causing either divergence or incorrect mass production and consumption. To prevent any negative population, the grid size must be refined proportionally to the increased reaction rate (or Damköhler number). Furthermore, the reaction rate is different from $S_j = b_j M_j k C_{dw}$, especially at the initial time steps. Accordingly, the calculation should be performed in a consistent way by invoking the proper physics of non-local (i.e. from neighboring nodes) contributions into Eq. (4.7) to have a general form of boundary condition applicable to all reaction conditions.

In order to calculate the exact concentration on the reactive wall based on the reaction rate coefficient and the diffusion coefficient, macroscopic equations are employed as well as mass conservation. The mass conservation is already employed in Eq. (4.7), however, mass transfer is not satisfied explicitly by the previous equations. For this purpose, a discretized reaction-diffusion equation is used:

$$\frac{D_{dm}(C_{dn}-C_{dw})}{\delta y} = b_d k C_{dw}^n, \tag{4.8}$$

where n is the order of reaction, δy is the grid spacing, D_{dm} is the mixture diffusion coefficient of deficient reactant, and C_{dn} and C_{dw} are the concentrations of the deficient reactant at the neighbor node and reactive node, respectively. Equation (4.8) can be solved for different reaction orders. We consider here a first-order reaction. The explicit form of reaction rate as a function of neighboring node concentration is written as follows [17]:

$$S_j = \frac{b_j k M_j C_{dn}}{\frac{b_d k \delta y}{D_{dm}} + 1}. \tag{4.9}$$

The new boundary condition in Eq. (4.9), which is constructed by including the one-sided finite difference approximation of the normal concentration into a fully kinetically-consistent boundary condition for multicomponent reactive flows, is applicable for arbitrary $\mathrm{Da_s}$ (from zero to practically infinity).

A mass source term in the kinetic equation (4.5) typically modifies the zeroth, first, and second-order moments at a given node. Therefore, special consideration is required, especially for multicomponent gas mixtures. Although species properties such as velocity and partial pressure change during a reaction, the total mixture velocity, and pressure should remain constant. A constructed catalytic boundary condition based on mass flux density (ρU) is accurate, provided that the mixture density does not change due to catalytic reaction. This is valid for equimolar reactions such as the total oxidation of methane ($CH_4+2O_2 \rightarrow CO_2+2H_2O$). However, this definition of mass flux leads to a mixture velocity change for non-equimolar reactions. The change in total mixture density requires that the total mixture velocity at the boundary should vary accordingly, such that the mass flux of the mixture before and after the reaction remains constant. The conservation of mass flux is a basic requirement in catalytic systems where neither accumulation of species on the catalyst (deposition) nor consumption of the solid catalyst (etching) occurs.

Herein, we construct a boundary condition based on the mixture pressure. Since the total mixture pressure is constant at the gas-solid interface, the influence of the mass source/sink term should be evaluated. An effective reaction rate for species j ($S_{j,eff}$) is defined as follows [17]:

$$S_{j,eff} = S_j - \left(\frac{Y_j}{c_{js}}\right)\sum_{j=1}^{N} S_j c_{js}, \quad S_j = \frac{b_j k M_j C_{dn}}{\frac{b_d k \delta y}{D_{dm}} + 1} \tag{4.10}$$

Where c_{js} is the speed of sound corresponding to species j. The second term in Eq. (4.10) is a correction term to ensure constant pressure at the boundary. It can be shown that it is similar to the velocity correction term included in the common diffusion-reaction boundary condition in CFD methods. In other

words, the correction term considers different diffusion coefficients of species, which was previously neglected in Eq. (4.9).

The diffusive boundary condition is the only boundary condition that intrinsically has the potential to estimate slip velocity when the Knudsen number is relatively high. Figure 4.14 shows a schematic of the Knudsen layer and the velocity and concentration slips. As depicted in Fig. 4.14, the catalytic reaction occurs at the wall, while the diffusion flux equation is valid at the edge of the Knudsen layer and not inside the Knudsen layer. Therefore, the reaction-diffusion equation solved in the previous section should be modified accordingly to incorporate the effect of concentration and velocity jumps.

The slip velocity model proposed by Maxwell is adopted in this work. The isothermal form of the slip velocity model for small Knudsen numbers ($\mathrm{Kn} \ll 1$) is written as:

$$u_{js} = U_w + A_1 \sqrt{\frac{\gamma\pi}{2}} \left(\frac{\tau_j T c_{js}}{H}\right) \left(\frac{\partial u_{js}}{\partial n}\right), \tag{4.11}$$

where u_{js} is the species slip velocity at the wall. A_1 is the velocity slip coefficient and is equal to $\frac{2-\alpha_t}{\alpha_t}$, where α_t is the tangential momentum accommodation coefficient. A similar relation can be used for the concentration jump at the wall:

$$C_{js} = C_{jw} + A_2 \lambda_j \left(\frac{\partial C_{js}}{\partial n}\right), \tag{4.12}$$

where C_{js} is the concentration of species j at the wall, which differs from the concentration of the gas molecules near the surface due to the concentration jump. A_2 is a function of mass accommodation coefficient $\alpha_{m,j}$ as $A_2 = \frac{2-\alpha_{m,j}}{\alpha_{m,j}}$. In contrast to Eq. (4.10), the concentration jump in Eq. (4.12) cannot be implemented directly into the diffusive boundary condition (Eq. (4.7)).

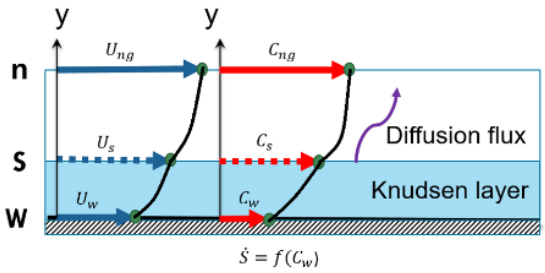

Fig. 4.14. Schematic of velocity and concentration slips in the presence of Knudsen layer.

In addition to the effect of velocity jump on the velocity field and of the temperature jump on the temperature field, both jumps theoretically affect the concentration jump as well. Therefore, a concentration jump model must include both velocity and temperature jumps (the latter for thermal flows). It has been shown that the effect of velocity slip on the concentration jump is negligible, hence it is not further discussed in this report. However, the effect of temperature jump on the concentration slip needs further investigation. Our model is derived in the presence of a temperature jump effect on the concentration slip, even though the current simulations are isothermal. The obtained equation gives a better insight into the impact of the concentration jump and the possible effect of the temperature jump on the reaction rate through the concentration jump.

To obtain an explicit equation for the reaction rate as a function of the aforementioned parameters, a similar approach to Khatoonabadi et al. [17] is followed. The difference with the no-slip boundary

condition is that the diffusion flux ($\rho D_{dm}\left(\frac{\partial Y_d}{\partial y}\right)$) is valid at the edge of the Knudsen layer and not at the reactive wall, while the reaction rate is a function of wall concentration/density. Using Eq. (4.8) at the edge of the diffusive layer and Eq. (4.12), and after some simplifications, the reaction rate of species can be obtained (Khatoonabadi et al. [18]) as follows:

$$S_j = \frac{b_j k M_j C_{dn}}{\sqrt{\frac{T_w}{T_s}} + \frac{b_d k \delta y}{D_{dm}} - A_2 Da_{ds} Kn_d}, \tag{4.13}$$

where T_s is the temperature slip at the wall for non-isothermal problems. Equation (4.13) can be utilized in the diffusive boundary condition (Eqs. (4.7) and (4.10)) instead of S_j. The main advantage of Eq. (4.13) over the previous implicit form (Eq. (4.12)) is that the impact of the controlling parameters can be theoretically evaluated to determine when the effect of concentration jump on the reaction rate is negligible. First, the temperature may modify the reaction rate depending on the ratio of wall-to-gas temperature. This influence is on top of the temperature jump and the dependence of the reaction rate constant (k) on temperature. When the wall temperature is higher than the inlet temperature in a channel configuration, the temperature jump has an adverse effect on the reaction rate. Second, Eq. (4.13) exemplifies the impact of the Knudsen number under particular conditions. There are two conditions under which the concentration jump plays a significant role on the reaction rate; the impact can be large due to either a high surface Damköhler number ($Da_{ds} \gg 1.0$) or a very low mass accommodation coefficient number ($\alpha_{mj} \ll 1.0$). Third, Eq. (4.13) can be reduced to Eq. (4.9) for isothermal flows and low Knudsen numbers.

Simulation results using the above-derived model are presented next.

4.2.1.3 Simulation results for a 3D polymer electrolyte membrane (PEM) micro fuel cell

This non-reactive simulation aims at demonstrating the LB model's capacity to handle complex 3D flows. PEFC fuel cells are electrochemical devices, converting hydrogen and oxygen (air) into electricity, heat and water. The gaseous reactants (hydrogen and oxygen) need to be distributed as uniformly as possible across the catalyst-coated electrodes in two separated compartments, while product water, heat and electrons need to be conducted as well. Two adjacent layers, the flow field (coarse distribution) and the porous GDL serve this purpose. A membrane, coated with electro catalyst on both sides is sandwiched between the GDLs (Fig. 4.15), completing the PEFC fuel cell. The geometry of the flow channels and the GDL influence the flow distribution and thus the utilization of reactants.

Since the product of the chemical reaction is water, formed at the electro-catalyst surface on the oxygen side (cathode), oversaturation and thus condensation can occur in the GDL and the flow channels (room temperature operation or high loads under isothermal conditions at elevated temperatures). This influences the reactant distribution. At the same time, adequate hydration is critical for the proton conductivity properties of the membrane. This dynamic situation requires an optimum balance of the water content across the membrane and the GDLs on both sides, usually done by controlling gas humidification and operating temperature. Nevertheless, there are certain regimes during operation where condensation cannot be completely avoided. Thus, the main requirement for GDL and the flow field is a uniform distribution at low-pressure drop and a good handling of liquid water. To understand the influence of channel, GDL and saturation on the gas distribution a micro fuel cell was studied (supplied by the Electrochemistry Laboratory of PSI). The results of this work have been published in Khatoonabadi et al. [19].

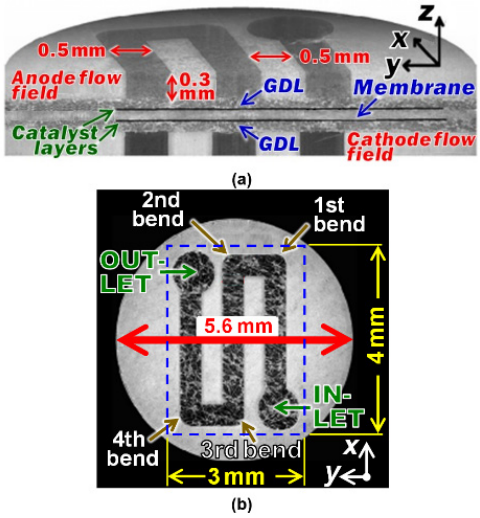

Fig. 4.15. (a) Cross-section of the micro fuel cell, representing the positions of the serpentine gas channel, GDL and catalyst layer, (b) top-view of the cell. Both pictures are reconstructed in 3D from the XTM images.

A combined experimental and numerical approach is adopted to study the flow field over a full-sized operating cell, where the gas is distributed via a single serpentine channel. As a result, numerical predictions of the magnitude and distribution of the cross flows are performed at the pore level, under different operating conditions. This is made possible by using the full structure of the fuel cell on the cathode side, obtained from Synchrotron X-ray Tomographic Microscopy (XTM) under wet as well as dry operating conditions. The flux and current boundary conditions chosen for this study are summarized in Table 4.3. For Case I with an air velocity in the cathode channel of 0.8 m/s (Re = 26), the gas phase gets saturated along the channel, while for Case II with a much higher velocity of 5.5 m/s (Re = 180) the calculated gas phase saturation stays well below 100% from inlet to outlet. In the present simulations, and to facilitate comparisons with the fully saturated Case I, the GDL and channel geometry in Case II are modeled without the presence of liquid water. An additional case is also investigated, having the same flow as Case I (Re = 26) but again without the presence of liquid water in the GDL and channel.

Table 4.3 Flux, current and flow conditions in the experimental setup (An: anode, Ca: cathode).

Case	Current density [A/cm^2]	Flowrate [NmL/min]		Gas Velocity [m/s]		Stoichiometry [-]		Re* [-]	Temperature [°C]
		An	Ca	An	Ca	An	Ca	Ca	Cell
I	0.32	14.5	7.2	1.6	0.8	27	27	26	30
II	-	100.0	50.0	11.0	5.5	-	-	180	30

*The Re number is based on the hydraulic diameter of the channel with respect to average width and height of the entire length of the serpentine path.

The XTM Synchrotron imaging conditions and the image processing required to extract the porous geometry have been detailed in [19]. The processing allowed assessment of all related phases: solid phase, liquid (water) phase for Case I, and void. High resolution XTM was applied, with each voxel side having a length of 2.9 μm. Mass transport simulations over the lower half of the measured geometry (cathode GDL and channel in Fig. 4.15(a)) were performed. Selected simulations over the full 5.6 mm cell diameter did not show appreciable differences with corresponding simulations over a smaller 3×4 mm^2 X-Y rectangular section (see Fig. 4.15(b)). The resulting computational domains are depicted in Fig. 4.16(a) for the dry Case II and in Fig. 4.16(b) for the wet Case I. The inlet and outlet cylindrical conduits in the model are extended in the Z direction 0.072 mm above the top channel surface (see Fig. 4.16) in order to properly capture the inlet/outlet flows. All domain external surfaces, apart from the inlet and outlet circular cross sections, are considered mass impermeable.

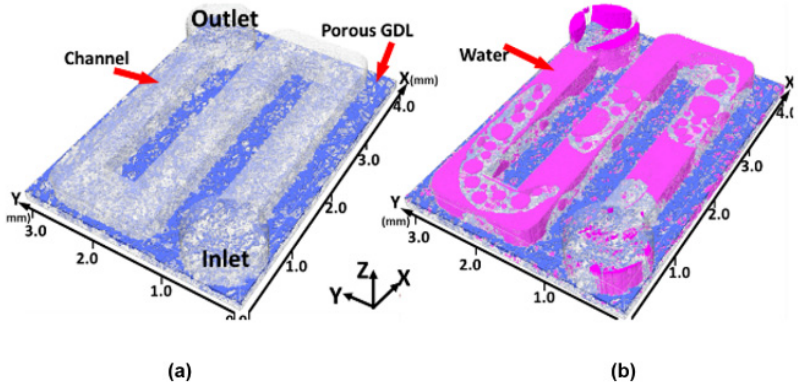

Fig. 4.16. Illustration of the porous GDL and the serpentine channel on the cathode side of the cell in (a) dry Case II and (b) wet Case I. Blue refers to solid fiber, purple refers to water clusters and gray represents the channel walls.

In order to accommodate the cell geometry (including the serpentine channel and the GDL in Fig. 4.15) into the computational resources and perform 3D LB simulations at the original XTM resolution of 2.9 μm, a computational domain with size 1440×1080×186 lattice nodes in X, Y and Z directions, respectively, is needed. Such dimensions lead to more than 270 million lattice nodes, while steady solutions are usually obtained over $\mathcal{O}(10^5)$ time steps.

To facilitate observation of the local magnitude of the shortcut cross-flows, Fig. 4.17(a, c) depicts 2D slices of velocity at the corresponding two critical X locations of the cell, where the shortcut region is enlarged in Fig. 4.17(b, d) to appreciate the true velocity levels. The larger pressure drop created due to the blockage by water clusters in the wet cell changes this general behavior to some extent. The condensed water accumulated inside of the channels forces the flow to enter the GDL which, contrary to the dry case, implies that strong cross-flows are not distributed under the entire length of the ribs but are rather limited to where the GDL pores are less clogged by water than the channel. In other words, water distribution strongly changes the cross-flow pattern in the wet case compared to the dry one.

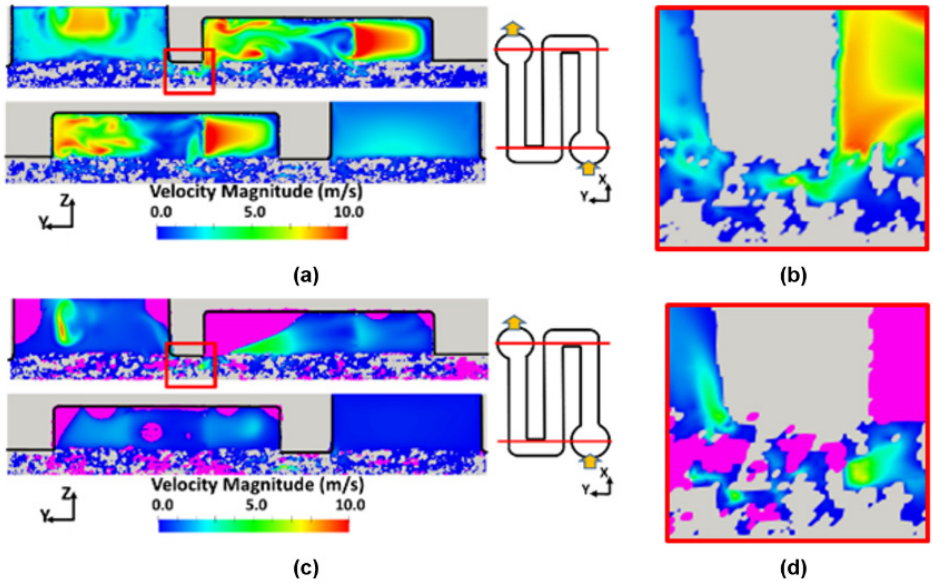

Fig. 4.17. 2D Y-Z slices of velocity magnitude made in two sections along the X-axis (see red lines crossing the cell), for (a) dry GDL in Case II and (c) wet GDL in Case I. The areas between channel and inlet/outlet are enlarged in (b) for dry and (d) for wet cell. Purple color refers to the water clusters and gray denotes the solid fibers.

In general, considerable parts of the flow are directed inside the GDL and across the cell in the Y direction, bypassing the channel in the dry cell. Having studied the gas flow patterns, the fraction of the flow bypassing the channels towards the porous substrate in different positions of the cell can be quantified. To this end, the mass fluxes of gas are measured at 22 positions along the channel as marked in Fig. 4.18(a) and the accumulated channel mass losses are plotted in Fig. 4.18(b). As expected, the high flow rate provided to the dry cell induces more cross-flow fluxes in the GDL compared to the wet case with low flow rate. Nevertheless, the relative magnitude of the cross-flows can be assessed by plotting the accumulated losses as a fraction of the total inlet flux for each case, as depicted in Fig. 4.18(c) and Fig. 4.18(d). Additionally, in order to study the effect of liquid water blockage on the cross flow magnitudes, simulations are shown for Re = 26 on a dry GDL as well, while the shortcut fluxes are added to the plots of Fig. 4.18.

Inspection of Figs. 4.18(c, d) reveals that in the case of the dry cell at the high Re = 180, more than 10% of the total flux is lost to the GDL in the first channel before reaching position A in the first bend. As the flow further proceeds along the first/second bends, the mass loss drops, i.e. the channel receives some gas from the GDL due to the low pressure created by the turning flow. After position C, the large shortcut cross-flows headed towards the outlet cause the mass loss to rapidly increase and reach a high plateau as seen in the enlarged view of Fig. 4.18(d). Interestingly, the flux in the second channel remains fairly constant, implying that the gain from the first channel through the first rib is nearly balanced by the loss to the last channel through the second rib. Upon reaching the third bend and from position D to F, the flow exhibits the same behavior as in the first bend. Recovering from the fourth bend, the channel loss increases by ~2% before entering the last channel, after which the channel starts regaining the lost mass through the second rib such that only 10% of the total flux remains to be delivered to the outlet by the GDL. Overall, under such a high Re number, the channel may not carry less than 85% of the total mass flux at the third/fourth bends. In contrast to the dry cell, Fig. 4.18(c) shows that a much larger fraction of the inlet mass (up to 46%) is lost to the GDL in the wet cell at Re = 26 and no overshoot of

the flux is detected around the bends. On the other hand, the flux trend from the dry GDL at Re = 26 shows very low levels of local mass loss (less than 11%) and similar trends to the dry cell at high Re number. This suggests that the large mass losses to the GDL in the wet case are indeed a result of the channel blockage by the large water clusters. Nevertheless, the shortcut flow between the bends and the inlet/outlets can still impose a considerable amount of loss or gain and play a significant role in distributing the cross flows. Further results can be found in the original published paper [19].

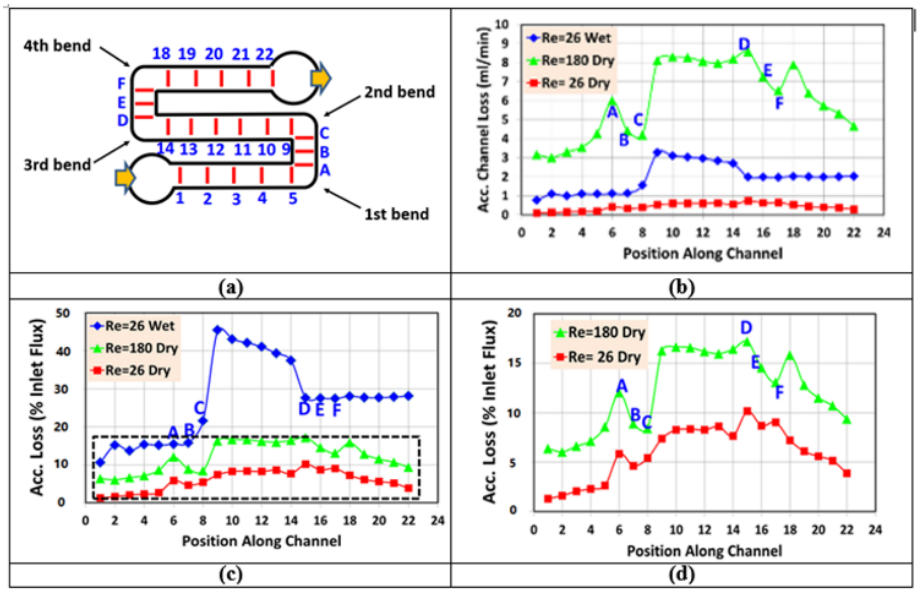

Fig. 4.18. (a) Positions of the flux measurement planes along the serpentine channel. (b) Accumulated loss along the serpentine gas channel in ml/min. (c) Accumulated mass loss as a fraction of the total inlet mass flux along the serpentine gas channel and (d) detail of (c) (from Khatoonabadi et al. [19]).

4.2.1.4 Simulation results for catalytic reactions at high Damköhler numbers

The employed CFD tool is a steady Navier-Stokes reactive in-house (LSM) code, where the governing set of equations are discretized using a finite volume approach. A SIMPLER method is employed for the pressure-velocity field and the solution is obtained iteratively using an ADI algorithm. An orthogonal staggered grid of 300 ×60 points (in x and y, respectively, for the 5 mm × 0.5 mm channel domain, with uniform x-spacing and finer y-spacing towards both walls), was sufficient to produce a grid-independent solution. The application of the catalytic boundary condition for the solution of the surface concentration of the deficient reactant was achieved with a modified Newton method using Surface-Chemkin. Local transport properties (species diffusivities and viscosities) were evaluated from the Chemkin transport package.

In order to have a meaningful comparison with previous studies, the total oxidation of methane is considered, as in [16], whereby CH_4 is the deficient reactant. Initial mole fractions in the domain are the same as the inlet values. The inlet velocity is uniform, equal to 7.2 m/s. The physical channel length (L) is 5 mm and the channel height (h) is 0.5 mm. The gas and wall temperatures are 1200 K and constant during simulation.

In the second comparison case, the reaction rate coefficient is increased such that $\mathrm{Da_s} = 2$. The results are plotted in Figs. 4.19(a, b). It is evident that there is a discrepancy between the original model results and the CFD simulations, which comes from the inaccurate calculation of the reaction rate. In fact, when the effect of diffusion is taken into account (in the new model) the denominator in Eq. (4.9) increases, hence, the reaction rate drops. When $\mathrm{Da_s} > 1.0$, one cannot neglect the effect of diffusion since the reaction rate calculated by Eq. (4.9) is different from the one obtained via the old iterative (old) approach. In contrast to the original model, the new reaction model guarantees a positive numerator at different grid sizes and time steps. If the reaction rate coefficient increases further, for example 5 times more, the original catalytic reactive boundary condition model fails, however, the new model still gives accurate results.

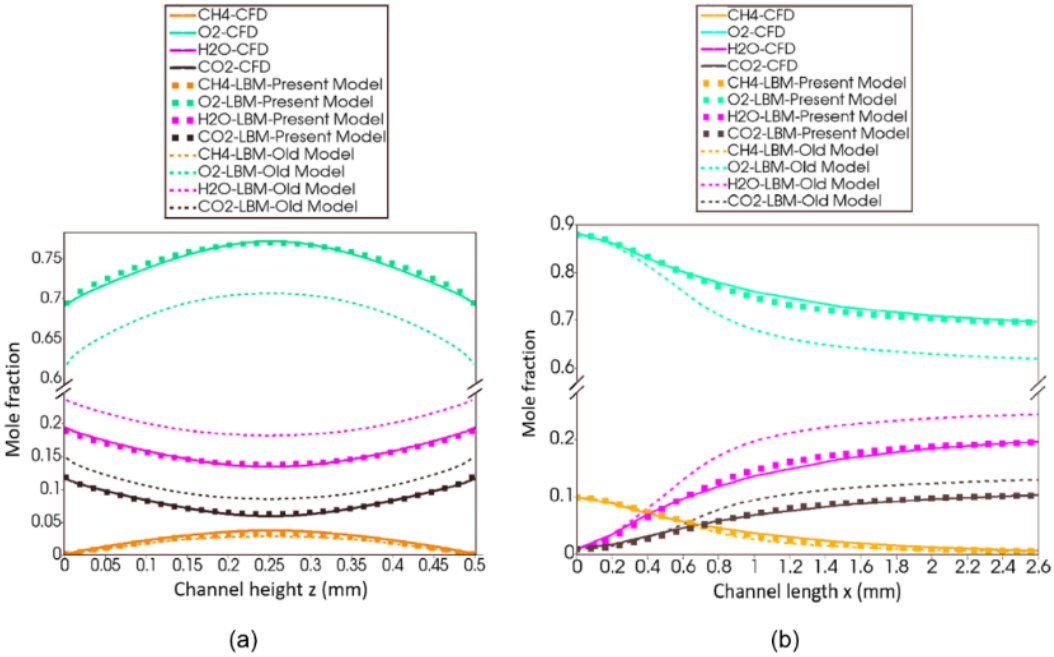

Fig. 4.19. (a) Comparison of mole fraction transverse profiles obtained from the old and present LB models as well as CFD results for $\mathrm{Da_s} = 2$ at x=2 mm. (b) Comparison of mole fraction axial profiles obtained from the old and present LB models as well as CFD results for $\mathrm{Da_s} = 2$ at the channel midplane (from Khatoonabadi et al. [17]).

4.2.1.5 Simulation results with the catalytic model for non-equimolar reactions

This example deals with simulations of non-equimolar reactions in straight channels. Considering CO methanation, the inlet mixture consists volumetrically of 83% hydrogen and 17% CO. CO is the deficient reactant, as the $\mathrm{H_2}$:CO ratio is larger than the stoichiometric 3:1 ratio. Molar ratios of $\mathrm{H_2}$ to CO between 3 to 6 are common in practical systems to avoid coking (carbon deposition). Needless to say, there is no limitation of any kind for the $\mathrm{H_2}$:CO molar ratio in the present model. The pressure is atmospheric, while the inlet temperature is the same as the wall temperature (T=1200 K) and they both remain constant during simulation. The channel length and height is 5 and 0.5 mm, respectively. The reaction rate follows the form of Eq. (4.13), being first order with respect to the deficient reactant CO. The surface Damköhler number based on the deficient CO reactant is 0.3, which is moderate and results in a mixed kinetics-transport controlled regime. The Knudsen number is very small ($\mathrm{Kn} \leq 0.001$) due to the large size of channel height, therefore, slip velocity is negligible in these simulations.

Numerical simulations are carried out for two grid resolutions, 50×500 and 10×100 (in X and Z). We focus on the results obtained with the coarser grid due to the significance of low resolution in the simulation of complex geometries such as reactive porous networks. While the fine grid requires 500,000 time steps to reach steady state, the coarse grid converges within 150000 time steps.

Figure 4.20 shows the mixture velocity contour in the channel using the newly developed reactive boundary condition of Eq. (4.10) in conjunction with Eq. (4.7) using 50× 500 grid points for both LB and CFD. As shown in the contour plot, the mixture velocity in the bulk of the channel starts increasing at the beginning of the channel due to wall friction and no-slip condition at the wall; in other words, the flow develops from uniform at X=0 towards a parabolic profile such that the midplane velocity initially increases. However, due to the volume-decreasing reaction, the mixture density increases with axial distance. Consequently, the velocity decreases, as more reactants are consumed at the catalytic wall.

The comparison between CFD and LB results at the midplane of the channel is presented in Fig. 4.21. The LB results are obtained for a coarse grid, where the channel height is discretized with 10 grid points. Generally, a very good agreement to the CFD simulation is achieved. The difference between the two simulation results at the outlet for mixture density and axial velocity is less than 2.9%. According to Fig. 4.21, the density increases around 50% along the channel. The variation of mixture density over the entire channel is illustrated in Fig. 4.22. The results show that the off-lattice multi-component gas mixture model with a species molar mass ratio as high as 14 gives quite accurate prediction. Using a finer LB grid (50×500) can improve the results modestly. The small difference between CFD and LB results may originate from the extrapolation due to different molar mass or different correction terms applied to calculate the reaction rate.

Figure 4.23 shows the mole fraction of species at the channel midplane with reduced grids (N_z=10). The LB simulation results match the CFD results very well. On one hand, the correction term defined in Eq. (4.10) will be more significant at larger reaction rates and/or higher differences among the species' diffusion coefficients. On the other hand, it will be negligible for equimolar reactions and/or when the mixture species have very similar transport properties.

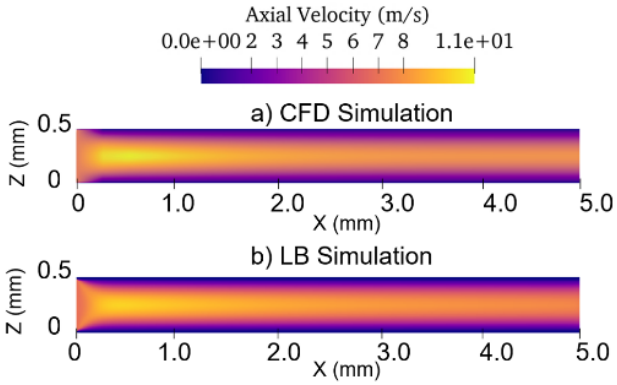

Fig. 4.20. Comparison of axial velocity contour obtained from CFD (top) and present Lattice Boltzmann (bottom) methods with the same resolution (50× 500); Kn=0.001, $\mathrm{Da_s} = 0.3$.

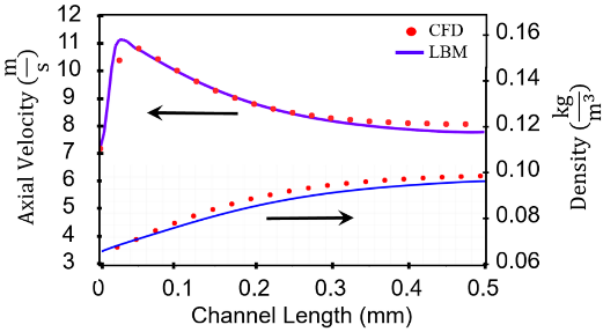

Fig. 4.21. Comparison of axial velocity and mixture density obtained from CFD and present Lattice Boltzmann methods; grid resolution: 10× 100 (LB) and 50× 500 (CFD); Kn=0.001, $\mathrm{Da_s} = 0.3$.

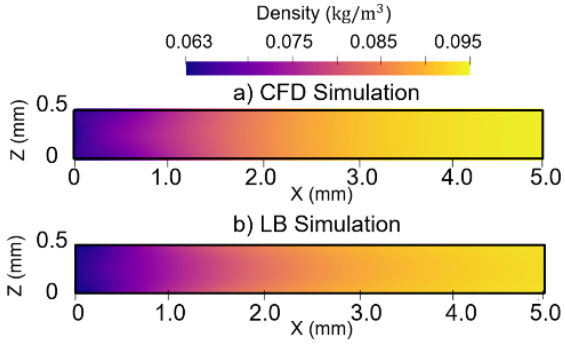

Fig. **4.22**. Comparison of mixture total density obtained from CFD (top) and present Lattice Boltzmann (bottom) methods with the same resolution (50× 500); Kn=0.001, $\mathrm{Da_s}$=0.3.

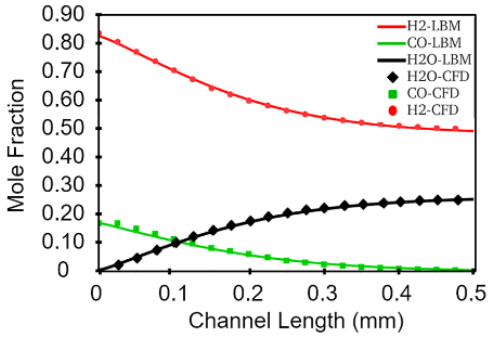

Fig. 4.23. Comparison of species mole fraction obtained from CFD and present Lattice Boltzmann methods; grid resolution: 10× 100 (LB) and 50× 500 (CFD); Kn=0.001, $\mathrm{Da_s} = 0.3$.

Hence, Task 5.1 (development of particle LB model) and Milestone 9 have been completed.

4.2.2 Task 5.2: Application of LB model to porous methanation particles up to 10 bar

4.2.2.1 LB model in real methanation porous particles

The results in this section have been published in Khatoonabadi et al. [25]. A resolution of 1 μm is used to simulate a porous particle, consistent with the resolution of X-ray tomography (TOMCAT synchrotron beamline at the Paul Scherrer Institute). The minimum pore size is 3 μm. The hybrid parallel code is developed based on a General Purpose Computation on Graphics Processing Unit (GPGPU) pipeline for the present computationally expensive simulations. The main calculations are performed on the GPU's processors simultaneously. The domain is decomposed in the direction of flow, and the communication between subdomains is handled by the Message Passing Interface (MPI). 400,000 time steps are required to reach steady-state conditions. The simulations are run on the GPU cluster (Piz Daint) of the Swiss national supercomputing center (CSCS).

A stationary particle is placed inside a channel where the no-slip boundary condition is applied at the channel walls. The physical parameters are chosen based on the operating conditions of a CO methanation fluidized bed. A constant velocity 0.8 m/s at the inlet and constant pressure equal to 1 bar at the outlet is applied. The stoichiometric molar ratio $\frac{X_{H_2}}{X_{CO}} = 3$ is considered at the inlet. Here, the inlet gas mixture consists of 25% CO and 75% H_2. The inlet, outlet, and channel wall temperatures are set to 600 K, which is typically the constant operating temperature in the methanation fluidized beds obtained by water cooling tubes along the bed [3], and it remains constant during simulation. Moreover, the transport properties at every node and every time step are calculated using the CHEMKIN transport package for all species.

According to the numerical code efficiency and the time limitation in using many GPUs, we conclude that the simulation of real porous particles require 16 GPU cards running 24 hours. The artificial spherical particle simulations that are shown later on take around 90 hours with four GPU cards.

The goal is to perform the pore-scale simulation under realistic operating conditions and with minimum assumptions. Therefore, it is crucial to study the particle's actual geometry. To this end, some samples are scanned by the PSI's TOMCAT beamline facility, and the high-resolution structure of porous particles is obtained. Figure 4.24(a) illustrates a phase-contrasted XTM image of a sample tube containing 11 porous particles. The obtained image has a voxel size of 0.162 μm with an optical zoom of 40X. Next, the gray-scale XTM images are converted into segmented binary images to reconstruct the full 3D porous structure in Fig. 4.24(b). The final 3D reconstructed 11 particles are shown in Fig. 4.24(b).

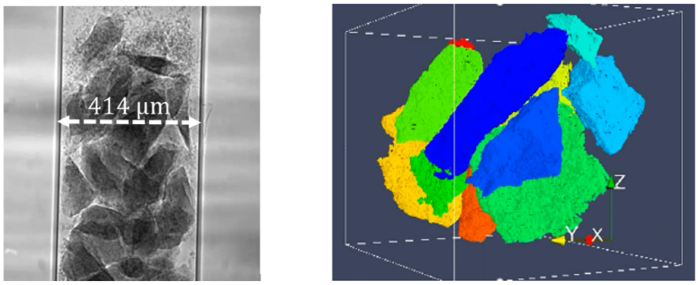

Fig. 4.24. a) gray-scale XTM image from a tube containing 11 catalytic porous particle, b) reconstruction of the porous particles after the segmentation of the raw XTM images.

We selected one of the smaller samples since it facilitates the pore-scale numerical simulation. Pores smaller than 1 μm are not resolved. The particle dimensions in X, Y, Z directions ($D_{px} \times D_{py} \times D_{pz}$) are $178 \times 126 \times 62\ mm^3$. Figure 4.25 shows the streamline colored by the velocity magnitude and CO mole fraction.

For all particle methanation simulations, the Langmuir-Hinshelwood mechanism for CO methanation reaction proposed by LBK (Kopyscinski et al. [2, 3]) for atmospheric pressure is adopted here to have a more accurate chemical reaction rate relation. The reaction rate is:

$$S_j = \frac{b_j k M_j K_1 X_{CO}^{0.5} X_{H_2}^{0.5}}{(1.0 + K_1 X_{CO}^{0.5} + K_2 X_{CO} X_{H_2}^{-0.5})^2}, \tag{4.14}$$

where K_1 and K_2 are adsorption constants and are set as 1.77 and 0.66, respectively [2, 3].

A large proportion of the gas flow hitting the porous catalytic particle crosses the particle without entering the inner pores since the friction (resistant force) inside the particle is much higher than that of the outside. In the real gas-solid fluidized beds, however, the resistant force outside the particle can be of the same order of magnitude due to the existence of other adjacent particles; consequently, more gas flow goes through the porous particle to react catalytically. Figure 4.25 illustrates an XY-plane cut from the 3D results, where the streamlines are colored by the CO mole fraction. It shows that even the fluid having the chance to enter the porous particle may leave it very quickly after passing a few pores. For example, in this particular sample, more macropores are located in front of the particle, and the streamlines show that a small percentage of the flow penetrated in the porous particle continues to reach the end of the particle. Therefore, the presence of macropores might change the flow's characteristics and the catalytic particle's reactivity. More importantly, there are few macropores that cannot be treated statically. The streamline inside the porous particle shows that the distribution of CO mole fraction around the particle varies significantly. Therefore, the common assumption in the continuum models regarding a constant distribution on the particle's outer surface is violated in real porous particles.

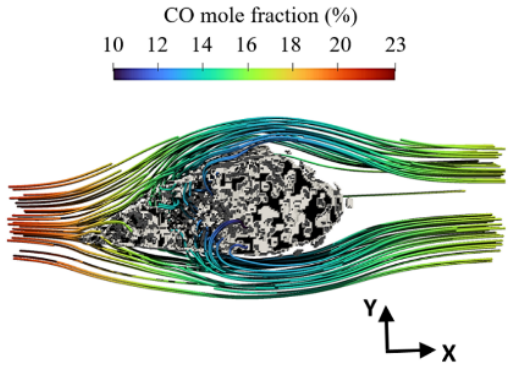

Fig. 4.25. Streamline around the catalytic particle for moderate reaction rate (A=1.28×10^6 cm/sec) colored by a) velocity magnitude and b) CO mole fraction.

2D velocity magnitude and species' mole fractions contours at the XY midplane of the domain are shown in Fig. 4.26. The velocity magnitude inside the particle's pores is miniscule due to very small pore sizes, except where the large pore connects the outside of the particle. This macropore helps the products to leave the inside of the particle faster. The molar fractions of hydrogen and carbon monoxide indicate

that CO is the deficient reactant that is consumed faster inside the tiny pores. In fact, the consumed H_2 can be replaced faster than CO due to a higher diffusivity. Accordingly, water and methane are produced and accumulate inside the particle. This multiscale phenomenon makes the numerical simulation more expensive since the mixture velocity inside small pores is several orders of magnitude smaller than that of the mainstream. Hence, a longer simulation (more time steps) is needed compared to the non-porous particle simulation.

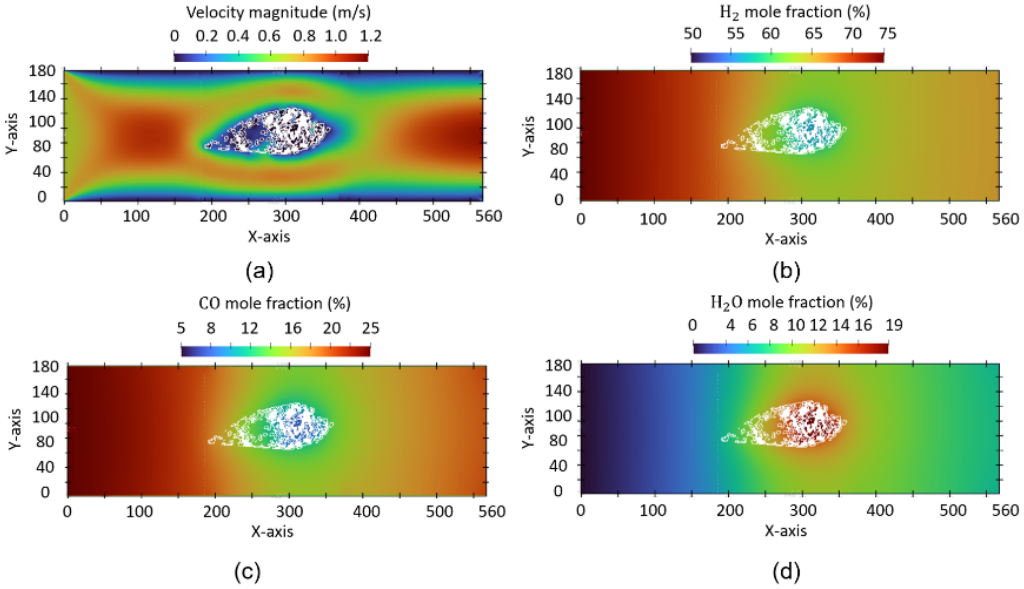

Fig. 4.26. Two-dimensional contour plots at the XY midplane of a channel containing a real methanation particle, a) velocity magnitude, b) X_{H_2}, c) X_{CO}, d) X_{H_2O}.

4.2.2.2 LB model in spherical methanation porous particles

This section addresses the variation mixture velocity and species mole fractions inside and around a catalytic porous particle at different Damköhler numbers, i.e., 0, 0.01, 0.05, 0.1, and 0.2. The reaction rate coefficient k is varied to alter the Damköhler number, while the other parameters are kept the same.

To show the variation of CO mole fraction inside the porous particle, the fluid nodes inside the particle are extracted, and the cross section of the particle is shown in Fig. 4.27. As shown in Fig. 4.27, the mole fraction of CO at $Da_s = 0.2$ approaches zero close to the center of the particle while the lower Damköhler numbers are not high enough to consume all CO. On the other hand, once the concentration of CO goes to zero, the reaction rate becomes very small; consequently, some parts of the porous particle (the area close to the center of the particle) do not participate in the conversion process.

Another important finding from the present results is that the minimum mole fraction is not observed exactly at the center. In other words, although the mole fraction distribution seems radial as the theoretical analysis predicts, it is shifted towards the direction of the flow (X direction). The main reason is that the actual mole fraction distribution around the particle is asymmetry, even for a symmetric particle. This is usually neglected in analytical models and continuum models. The difference between the mole fraction in front and behind the particle depends on the reaction rate (Damköhler number). While the maximum mole fraction difference on the surface of the particle in $Da_s = 0.01$ is only 1%, around 34% difference is observed in $Da_s = 0.2$. Table 4.4 compares the maximum and minimum CO mole fractions on the particle's surface for different Damköhler numbers.

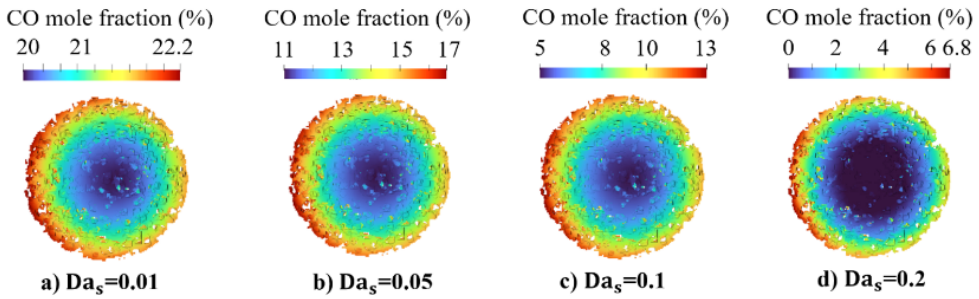

Fig. 4.27. Distribution of CO mole fraction inside porous particle for different Damköhler numbers: a) $\mathrm{Da_s} = 0.0.1$, b) $\mathrm{Da_s} = 0.0.5$, c) $\mathrm{Da_s} = 0.1$, d) $\mathrm{Da_s} = 0.2$.

Table 4.4. Maxima and minima mole fraction values on the outer surface of a porous particle in different Damköhler numbers.

$\mathrm{Da_s}$	0.01	0.05	0.1	0.2
Max. $\mathrm{X_{CO}}$	0.223	0.168	0.128	0.068
Min. $\mathrm{X_{CO}}$	0.217	0.148	0.103	0.045
$\frac{\mathrm{Max.\,(X_{CO})} - \mathrm{Min.\,(X_{CO})}}{\mathrm{Max.\,(X_{CO})}}$	0.027	0.119	0.195	0.338

The distribution of velocity magnitude inside the porous particle can reveal helpful information. Figure 4.28 shows the scatter plot of velocity magnitude as a function of particle radius. The velocity magnitude is much smaller than the free stream velocity when the reaction rate is meager ($\mathrm{Da_s} = 0.01$). The velocity drops suddenly at the beginning of the outer pores of the particles. However, the catalytic reaction causes a diffusion flow inside particles towards outside such that the higher the reaction rate, the stronger the diffusion flow. The velocity induced by diffusion is as large as the convective velocity. Therefore, it hinders flow from entering the pores from outside. This phenomenon is explained by Peclet (Pe) number considerations. Since the Pe number with regard to the particle diameter ($\mathrm{D_p}$) is the ratio of the convection rate to the diffusion rate, it determines the importance of one process over another. Although the particle Peclet number is 1.5 in this simulation, the convective flow is not dominant. It could be because of the effective velocity inside pores that is much smaller than the inlet velocity. Therefore, considering the Peclet number based on the mainstream velocity, a very high Pe number ($\mathrm{Pe} \ll 1.0$) is needed to observe the appreciable impact of the convection inside porous particle.

Another important conclusion from Fig. 4.28 is that some inner parts of the particle (around 35%) experience very low flow rates in the pores at Damköhler number $\mathrm{Da_s} = 0.2$. These simulations indicate that at very high Damköhler numbers ($\mathrm{Da_s} \gg 0.1$), all pores do not play a role in conversion anymore since the fuel is used up entirely before reaching the center of the porous catalytic particle. In other words, it seems that using porous particles for $\mathrm{Da_s} > 1$ is not beneficial. The core-shell particles are better options for the intermediate Damköhler numbers ($0.1 < \mathrm{Da_s} < 1.0$), where the core of the particle is non-porous, and the outer part has a porous structure.

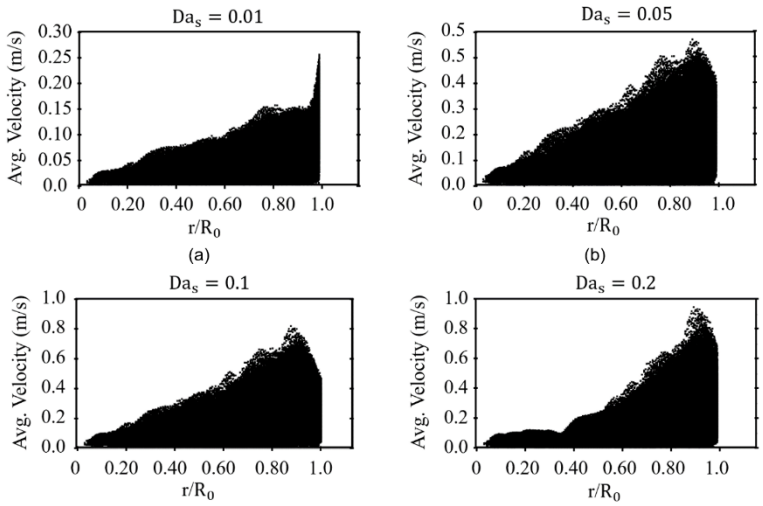

Fig. 4.28. Average velocity magnitude distribution of the gas mixture inside particle versus non-dimensional radius ($\bar{r}$) for different Damköhler numbers: a) $\mathrm{Da_s} = 0.0.1$, b) $\mathrm{Da_s} = 0.0.5$, c) $\mathrm{Da_s} = 0.1$, d) $\mathrm{Da_s} = 0.2$.

Table 4.5 shows the share of outer surface reaction compared to all catalytic reaction rates (outside and inside of the particle). By increasing the Damköhler number (or Thiele modulus), the reaction rate on the outside of the particle plays a more pivotal role. This observation can be explained based on the physics of the problem. The fuel gas is constantly consumed at the surface of pores, reaching the minimum value as it goes through more pores. Since the outer surface is catalytically reactive, it converts some part of fuel before entering the particle. This conversion is proportional to the reaction rate and the fluid particle resistance time. The former appears in the Damköhler number, and the latter can be a function of pore's Peclet number. As the velocity increases or the average pore size increases, the fuel has less time to react on the particle's surface. In these simulations, the whole catalytic surface is five times larger than the surface on the outer part. Consequently, we expect that the lower limit of the catalytic reaction at the outer surface to the entire surface reaction at a very small Damköhler number approaches 20% (same as the geometrical ratio).

The total CO catalytic conversion is also reported in Table 4.5 as the percentage of CO mass flow rate behind the particle over the inlet CO mass flow rate. It is worth mentioning that the exact value cannot be directly interpreted since it changes if the channel size varies. However, the comparison with other Damköhler numbers indicates that the intermediate Damköhler number $\mathcal{O}(0.1)$ is high enough to convert a considerable percentage of the inlet fuels.

Table 4.5. Maxima and minima mole fractions on the outer surface of a porous particle in different Damköhler numbers.

$\mathrm{Da_s}$	0.01	0.05	0.1	0.2
φ	0.37	0.84	1.18	1.68
$\frac{S_{out}}{S_{tot}}$ (%)	25.5	26.1	27.9	30.9
CO mass conversion rate (%)	7.5	22.8	35.7	48.4

4.2.2.3 Impact of macropores

The XTM images of actual porous particles reveal the presence of inhomogeneity in the porous structure. For example, small and large pores may be distributed unevenly throughout the porous particle. An artificial porous particle is considered to assess macropores' impact, and several macropore sizes are created to model the effect of macropores on the porous particles. Figure 4.29 shows a 3D spherical porous particle and an XZ plane from particles with and without the added macropore. This figure illustrates the size of pores (d_p) in comparison to the macropore (D_{mp}) and the particle's diameter (D_p). The average pore size is 6μm, and the pores are distributed homogeneously throughout the particle. Five different macropore sizes are simulated, i.e., 0, 10, 20, 30, 40μm. These values are the minimum macropore sizes, and the exact macropore diameter varies along the particle due to the connection to the micropores inside the particle.

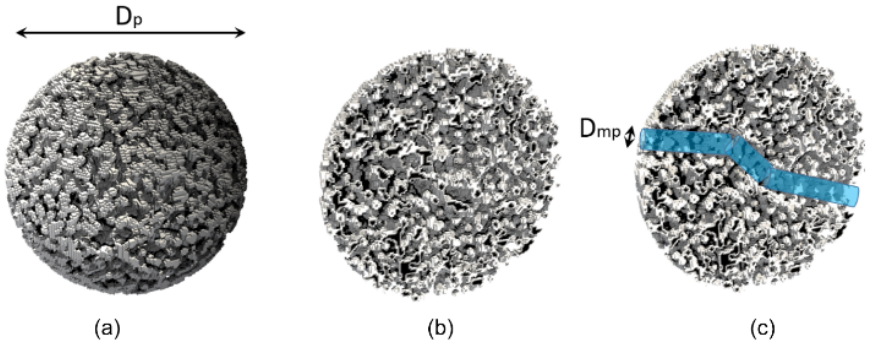

Fig. 4.29. Geometry of the artificial porous particle: a) a full particle, b) half a particle without macropore, c) half a particle with a macropore.

Figure 4.30 shows streamlines colored by the CO mole fraction. It stems from reducing the number of active pores. While the active pores with a specific flow rate are distributed almost randomly in porous particle without a macropore (Fig. 4.30(a)), the macropore becomes dominant and guides the main flow stream in porous particle outwards. This affects the flow rate in the small pores, where the friction is higher; and consequently, a very small proportion of the mass flow rate goes through such pores. Figure 4.30 also shows that the active pores in the porous particle with macropores are mostly located either close to the outer surface or near the macropore. Hence, many pores become practically inactive or their role in total catalytic conversion decreases noticeably. On the other hand, more flow rate with a higher fuel concentration can penetrate the particle, therefore, more catalytic surfaces have access to the fuel leading to a higher reaction rate. In conclusion, the total catalytic reaction does not change considerably. The drop in CO conversion is due to the higher porosity and lower surface-to-volume ratio.

A similar phenomenon was observed for other cases with different macropore sizes, leading to the conclusion that the convection to diffusion is minimal. The Peclet number calculated based on the macropore diameter ($\mathrm{Pe_{mp}}$) is zero and 0.3 for the particles without and with macropore ($D_{mp} = 30\ \mu\mathrm{m}$), respectively. Therefore, the macropore Peclet number ($\mathrm{Pe_{mp}}$) less than unity is not high enough to make a noticeable change in catalytic conversion inside a porous particle.

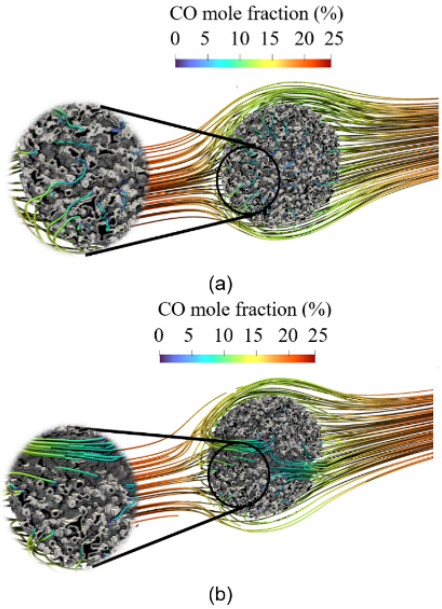

Fig. 4.30. Flow streamlines colored by the CO mole fraction: a) without a macropore $D_{mp} = 0$, b) with a macropore $D_{mp} = 30\mu m$.

4.2.2.4 Impact of pressure

All previous simulations are conducted at the same pressure (P=1 bar). To understand the effect of the operating pressure on the reactivity of catalytic porous particles, a new simulation is run at high pressure P=10 bar, while the other parameters remain constant. The surface Damköhler number is equal to 0.1 in both cases. Since the inlet velocity and particle diameter are the same in the two simulations, the Reynolds number is 10 times smaller at P=10 bar than that at P=1 bar. Figure 4.31 shows the streamlines around and inside particles colored by the CO mole fraction. In addition to the difference in the streamlines due to the Reynolds number, the catalytic conversion of the particle at higher pressure increases. In fact, high pressure enhance the reactivity of the particle by 18% compared to the case with lower pressure (P=1 bar).

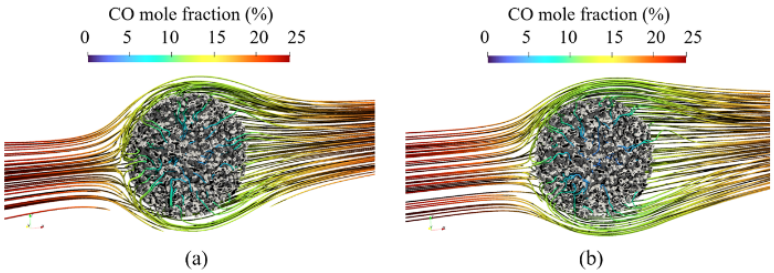

Fig. 4.31. Flow streamlines colored by the CO mole fraction at different operating pressures: a) P=1 bar, b) P=10 bar.

Hence, Task 5.2 (application of LB model up to 10 bar) and Milestone 10 have been completed.

4.3 WP 3 Task 3.1 GanyMeth commissioning

The construction and commissioning of the GanyMeth differed in many aspects from the ideal path of a project. Some of the reasons were the previous industrial partner and supplier of the pilot plant that lost the interest in the technology, job change of key persons on the supplier side, insolvency of the sub-supplier of the reactors and the skid, and incorrectly welded tubings at the plant. This lead to the decision to finalize the erection of the Pilot plant by PSI which covered the electric connections, insulation, all safety measures as well as building and programming of the control system.

Within the SCCER BIOSWEET funded activities, the plant was commissioned in two steps: a simplified preliminary control system enabled significant hydrodynamic work using cold pressurized air as fluid and inert aluminum oxide particles as bed material. In these measurements, radially movable optical probes at six different heights measured the rise velocity and pierced length of the “bubbles” (= catalyst free voids) that rise in the reactor and are responsible for good mixing and excellent heat removal performance of fluidized bed reactors with heat exchangers. A large range of pressure levels, gas velocities and two particle sizes were covered. From these measurements, one publication is already out and another one in preparation.

After cold experiments, the plant was refurbished to allow for hot experiments with reactive gases. This work was also delayed compared to planning, due to the passing of one control specialist and later the partial job change of the other control specialist (10-20% availability instead of 100% before). Moreover, to enable critical experiments for a PhD thesis to be conducted on time, experiments with the COSYMA set-up (cf. to the next two sections) were prioritized during seven months. Finally, all necessary work was finished in summer 2022, and the documentation of the plant including all safety documents were submitted to PSI internal authorities and to the TISG (Technisches Inspektorat der Gaswirtschaft) as external control body. A visit at the plant convinced the authorities, which gave the permission for operating the GanyMeth plant.

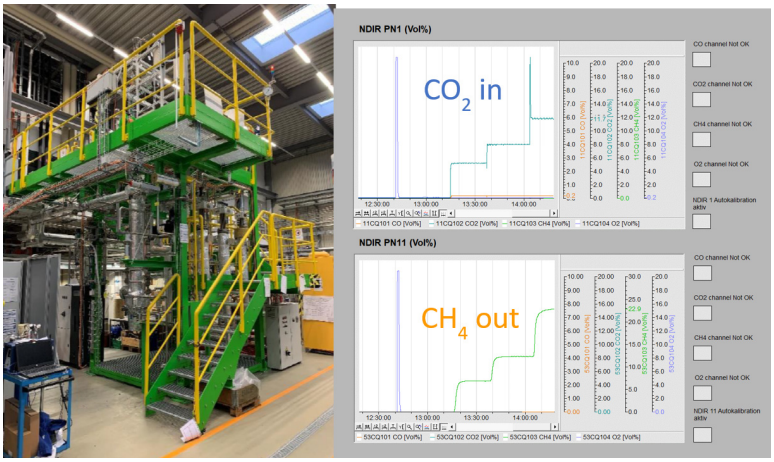

Fig. 4.32. Pilot plant GanyMeth and experimental data from the first reactive operation.

Fig. 4.32 above shows the result of the very first experiments where CO_2 was added with hydrogen in three steps of volumetric flow, and accordingly, the methane rises in the reactor outlet. While the flow rates and concentrations were not yet the maximum ones, all important subsystems, especially the cooling worked without problems. Thus milestone 5 was reached. The analytic system (sampling lines, valves and microGC analytics) have also been finalized. The campaigns conducted so far are reported in section 4.5.2.

All GanyMeth experimental campaigns have been planned in close collaboration with our new industrial Partner, AlphaSYNT GmbH, and funded partially by the Innosuisse Flagship Project DeCIRRA (Decarbonisation of Cities and Regions with Renewable Gases) and to larger extent by the SBFI within the European Union project HyFuelUp. In this project, a consortium of academic and industrial Partners from Portugal, Germany, Greece, Spain, the UK and Switzerland will develop and demonstrate until 2026 an advanced technology for gasification of biomass waste and subsequent methanation of the resulting gases, in a hybrid process with the addition of green hydrogen. The biomethane produced will then be liquefied and used in the decarbonization of the transport sector, particularly in long-distance road haulage and maritime transport, thus leading to a reduction in greenhouse gas emissions. For this, innovative gasification and methanation processes based on fluidized bed reactors will be first tested in TRL 6 pilot plants in Germany (Univ. Stuttgart) and at PSI (with AlphaSYNT), respectively. In Portugal, an existing gasifier will be adapted in collaboration with industry to operate as Dual Fluidised Bed gasifier and complemented by feedstock handling, gas cleaning, the methanation unit, gas upgrading and liquefaction.

The methanation unit (500 kW, TRL7) will be built by AlphaSYNT GmbH in Switzerland and then transported to Portugal. PSI will support the design of the plant as part of the agreed knowhow transfer and contribute to the gas cleaning activities as well as to the commissioning of the plant.

Hence, Task 3.1 and Milestone 5 (GanyMeth operation) have been fulfilled.

4.4 WP 4 (Pilot runs up to 10 bar)

4.4.1 Biogas tests

The future energy system will need balancing mechanisms on different time scales. Short-term fluctuations can be absorbed by batteries and pumped storage power plants, enabling hours to days of storage, which makes economic sense. For a longer storage up to the seasonal balance, the conversion into chemical energy carriers such as hydrogen and then methane is necessary. The interaction of components over the course of the year was simulated for a local energy system, which consists of photovoltaic modules, a battery, water electrolysis, a hydrogen tank and methanation, among other things. The battery stores the daily excess from the PV modules and gradually transfers it to the electrolyzer, which fills the H_2 tank. Depending on the consumption of the hydrogen for mobility and the desired filling level of the H_2 tank in order to get through bad weather phases, the methanation is not operated at all, at full load or at part load. In order to show that this flexibility is technically possible, experiments with the 10 KW methanation unit COSYMA (see Fig. 4.33) at the industrial biogas plant Swiss Farmer Power Inwil were conducted as part of the ReMaP project by means of data exchange with the electrolyzer of the ESI platform and the H_2 tank at PSI and a battery at Empa.

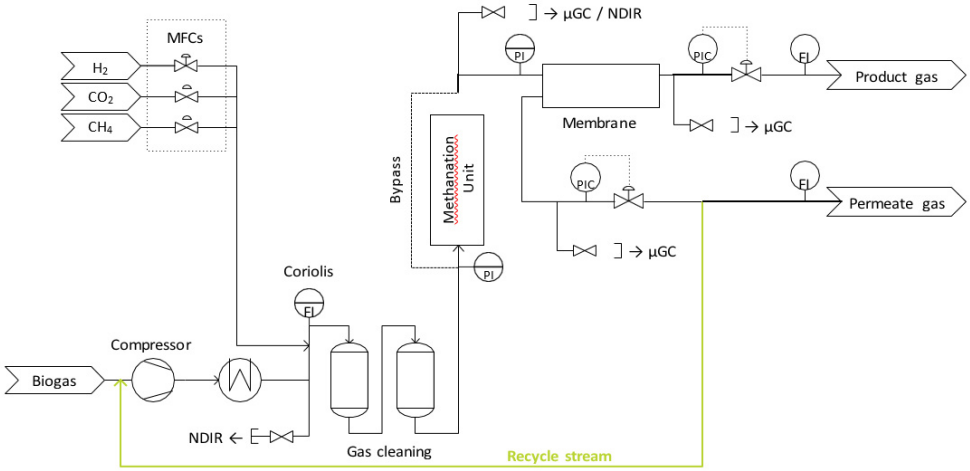

Fig. 4.33. Schematic of the COSYMA 10 kW methanation plant (TRL 5).

While these experiments were originally planned at the pilot plant GanyMeth, it was decided to use COSYMA to avoid undue delay of these experiments, which would have had a negative impact on a PhD thesis. **The biogas tests constituted a part of Andreas Gantenbein's PhD Thesis and have been published in [26].**

Hence, Task 4.1 and Milestone 6 (GanyMeth tests with biogas) have been completed.

4.4.2 Tests with wood and H_2/wood

The next campaign at GanyMeth, after the successful campaign reported in the coming section 4.5.2, will cover the conversion of simulated wood gasification gas that contains at least hydrogen and carbon monoxide, but also CO_2 and CH_4. These tests will take place in April 2024. During the preparation of this campaign in autumn 2023, it turned out that the gas supply for CO and methane had to be completely refurbished due to its age and to comply with the latest safety regulations. These works have been finalized in February 2024, such that March will be used for commissioning.

This experimental campaign will also cover the hydrogen-rich methanation of wood gas as to be expected in Power-to-gas applications.

Hence, Task 4.2 and Milestone M/ will be fulfilled in near future.

4.4.3 Benzene measurements

Due to the large experience with conversion of benzene in producer gas, collected in previous field campaigns (TRL 5 plant Cosyma and TRL 7 PDU connected to the gasifier in Güssing/Austria) as well as in systematic lab experiments, it was decided to omit the experiments with benzene at GanyMeth.

4.5 WP 7 (Process optimization, upscaling and cost assessment)

4.5.1 Optimization of operational limits

First, the complete operational field of Cosyma was tested to enable proper definition of full load and part load. As can be seen in Fig. 4.34, the white triangles show the lower operational limit of the main reactor, i.e. without recycle flow. As the minimum operational range depends on a certain effective gas velocity in the reactor to secure the mixing of the particles and the heat transfer, higher pressures allow for higher gas mass flows. The upper end of the reactor is given by the heat removal limit (red squares), i.e. the gas mass flows for which the heat of reaction still can be removed from the reactor. As visible, lower pressures lead to better heat removal, which is caused by the state of turbulence inside the system. Even higher gas velocities inside the reactor might lead to too strong catalyst particle attrition. It is well visible, that the reactor alone allows part load from 20% to 100%, i.e. a relatively large window of operation (milestone 15). As the cooling area per reactor volume are similar in COSYMA and GanyMeth, these results can be transferred also to large-scale plants.

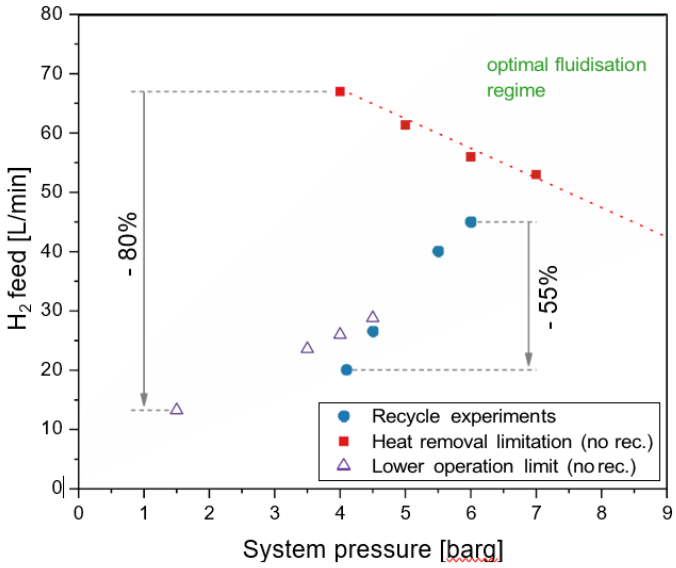

Fig. 4.34. Operational window of a fluidized bed reactor. The data points with recycle depend on the actual design of the plant, i.e. the ratio of reactor capacity and membrane area.

The picture is different for the complete set-up including the membrane separation and the recycle of its permeate (blue dots). In the COSYMA set-up, only one membrane unit is built in which narrows down the operational window. At too low pressures, the quality of the retentate (> 96% CH_4) could not be achieved due too low pressure differences in the membrane; at high pressures and accordingly high mass flow rates, the membrane area becomes limiting. Therefore, a complete methanation system will need some options to adapt the membrane area to allow for the full flexibility that is possible in the fluidized bed reactor.

As mentioned above, for the systemic experiment, the COSYMA setup was connected within the ReMaP experiments with the battery at EMPA and the electrolyzer at PSI. The hydrogen tank as well as the PV plant were modelled. Figure 4.35 shows the topology of the experiment. It can be seen that most of the

units needed some conversion factors to match the real size with the ones obtained during the Prosumer system modelling.

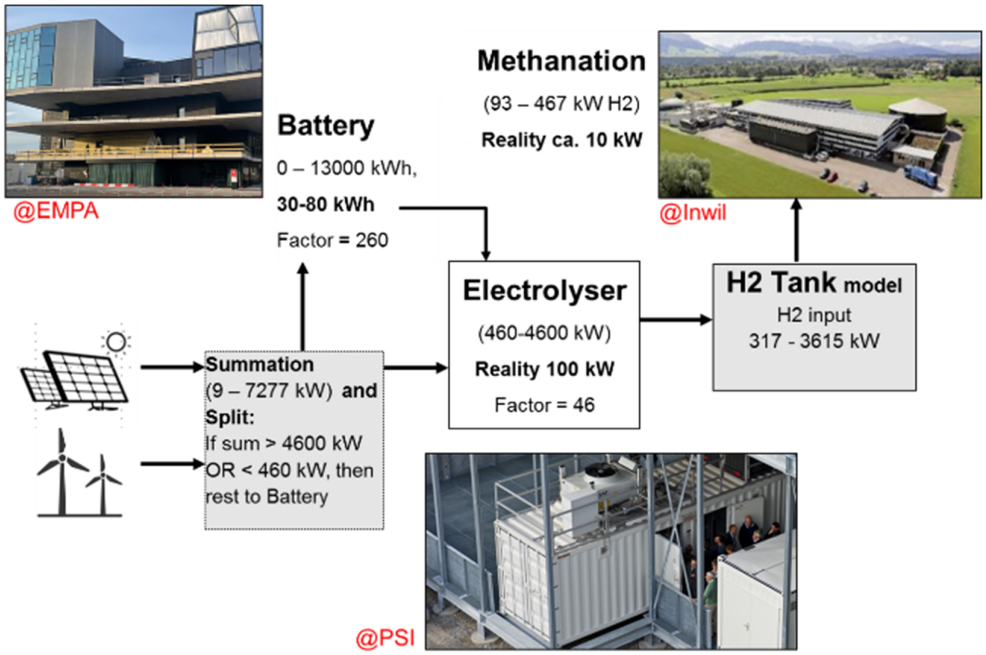

Fig. 4.35. Topology of the ReMaP experiment.

The methanation plant was operated including the complete hydrogen recycle. The simulated course of a PV profile required multiple changes in the methanation operation between 45% and 100% according to the experimental range for full and part load defined before. The task of the operators was to adapt the operation condition such that the fed-in gas quality (>96% methane, < 2% hydrogen) could be secured. As seen in Fig. 4.36, it was no problem to hold the 96% minimum methane content, while the upper limit of 2% hydrogen was only shortly violated. The main reason for this is the absence of a fast analytics for hydrogen: the used NDIRs see only methane, CO_2 and CO, while the micro-GC needs about 3 min for each analysis. A mass spectrometer, a NDIR also in the permeate or the gas quality sensors by MEMS GmbH are options to even avoid this very little hydrogen excess during injection.

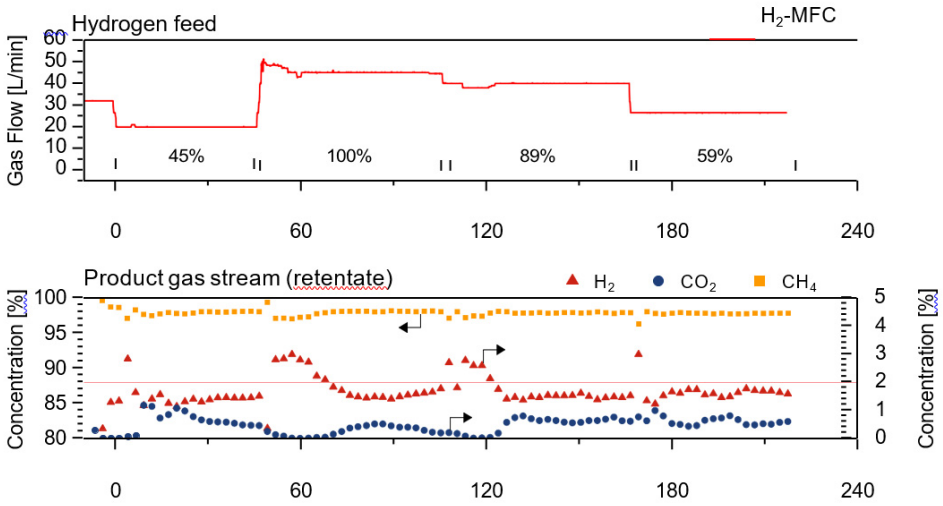

Fig. 4.36. Gas quality fed in at 40%-100% partial load in COSYMA during the ReMaP Experiment.

Hence, Task 7.1 and Milestone 15 (delineation of operational window for fluidized bed methanation) have been fulfilled.

4.5.2 Commercial issues and costs

Within the Innosuisse Flagship project DeCIRRA and supported by the European Union/SERI funded project HyFuelUp, it was possible to adapt the gas supply, the samplings system and to conduct a campaign of several days. Proper sampling of the gas at several heights of the reactor as well as many thermocouples inside allowed obtaining axial temperature and concentration profiles. The different sampling points in the plant were connected by 16 stainless steel capillaries with an air-conditioned room containing micro gas chromatographs (mGC) as analytical device. Drying tubes with hygroscopic salts were used to protect the analytical devices from condensates. In the analytical room, the flow of each individual sampling line can be controlled before the gas flows are distributed via a system of valves to the different mGCs. The micro gas chromatographs are regularly calibrated and can quantify the expectable species H_2, CO, CO_2, CH_4, and N_2, and also He, O_2, ethane, propane.

A wide range of operation conditions could be tested. 200 kW methane output was reached without issues; significantly more will be possible (only CO_2 supply is limiting right now due to a too narrow valve in the supply system), see Fig. 4.37.

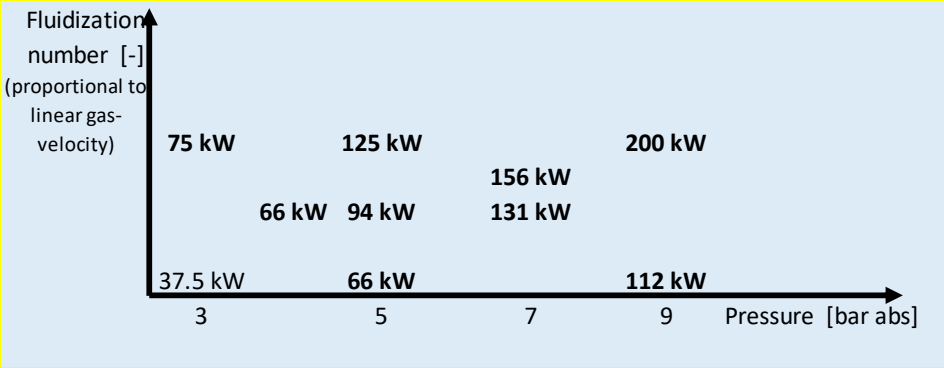

Fig. 4.37. Tested operational conditions.

The concentration profile of the 131 kW experiment in Fig. 4.38 shows that significant reactor volume is needed to convert the hydrogen and to form methane. The reaction progress of this volume contracting reaction system can also be followed by the concentration of the nitrogen (leaking in from a non-tight valve). Taking out the N_2 concentration (assuming a situation with a tight valve), one can see that very high methane concentration close to 90% can be easily reached due to the low stoichiometric excess of hydrogen (H_2/CO_2 = 4.07). According to the recent changes in injection specification Switzerland, this gas would be close to fit the specification for unlimited injection without any further upgrading (besides drying). This is even more the case when instead of pure CO_2, biogas (60% methane, 40% CO_2 is converted). Then, more than 95% methane could be reached, which is sufficient in many European countries for unlimited injection.

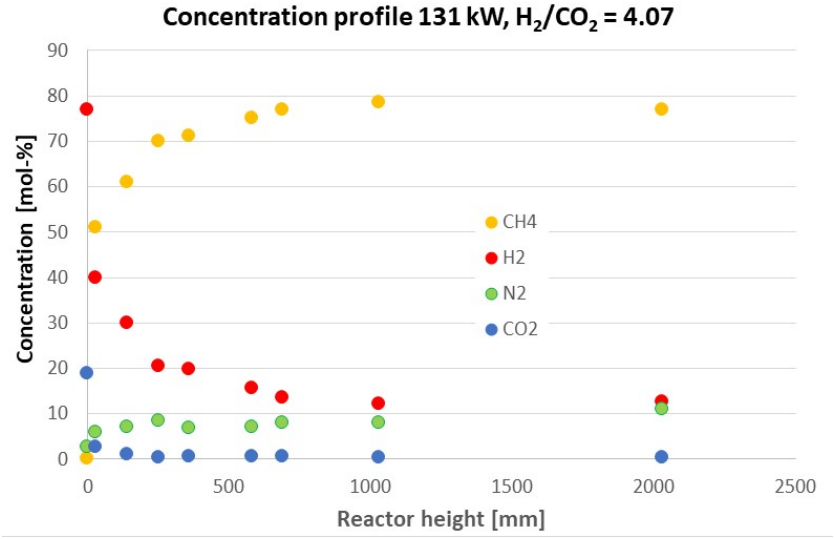

Fig. 4.38. Concentration profile for the of the 131 kW experiment.

The GanyMeth experiments support the finding with respect to part load operation of the COSYMA experiment shown in previous sections, i.e. part load and fast change between different load situations is no problem.

Further, based on previous results (from the past 12 years), GanyMeth was designed as a 200 kW SNG plant. As the recent results show, the reactor can reach this without any problems. This, together with the consistent part load findings in different plant scales, show that the design basis for this reactor type is sound, and can be considered as validated. Therefore, the cost calculations in recent publications (which are based on the so far used design knowhow) are realistic.

Most of the work on flexibility of methanation **plants as well as the techno-economic analysis of catalytic and biological methanation (contribution to milestones 16 and 17 see coming section) were conducted within the thesis of Andreas Gantenbein (see Refs. [27, 28])**, which was defended successfully at EPFL.

Hence, Tasks 7.2 and 7.3 with Milestones 16 and 17 (design, costs and performance of industrial reactors) have been fulfilled for the biogas.

4.6 WP 6 (Macroscopic model)

4.6.1 Inclusion of high-pressure methanation kinetics into macroscopic model

The kinetic scheme Witte-Schildhauer updated for the correct pressure dependencies (see Eqs. 4.2, 4.3 and 4.4) has been implemented in the two-fluid macroscopic model for the entire FB. The updated model is used in on-going work.

Hence, Task 6.1 and Milestone 11 (high-pressure kinetics implemented in macroscopic FB model) have been fulfilled.

4.6.2 Inclusion of benzene kinetics into macroscopic model

Due to the large experience with conversion of benzene in producer gas, collected in previous field campaigns (TRL 5 plant Cosyma and TRL 7 PDU connected to the gasifier in Güssing/Austria) as well as in systematic lab experiments, it was decided to omit the experiments with benzene at GanyMeth, cf. to section 4.4.3. In consequence, also the inclusion of benzene kinetics is omitted.

4.6.3 Inclusion of enhanced fluid-dynamics into macroscopic model

Due to late employment of co-workers, the improved representation of the fluid-dynamics in the macroscopic model is part of ongoing work.

Hence, Task 6.3 and Milestone 13 (enhance hydrodynamic part of macroscopic FB model) will be fulfilled in near future.

4.6.4 Validation of macroscopic FB model with GanyMeth experiments

Due to still ongoing preliminary subtasks, the model validation with GanyMeth data is still ongoing work. **Hence, Task 6.4 and Milestone 14 (validation of macroscopic FB model) will be fulfilled in the near future.**

5 Conclusions

This report covers the activities from a number of different projects (funded by SFOE, SNSF, Innosuisse, SBFI and the ETH foundation) and shows the knowhow on fluidized bed methanation technology ranging from fundamental lab research to pilot scale experiments at TRL 6.

The optically accessible test rig at PSI was modified for the methanation experiments to test FeCr-alloy plates coated with Ni/Al_2O_3 catalyst. In situ experiments of CO_2 methanation, involving Raman measurements of major gas-phase species concentrations, were conducted and 15 cases were analyzed by varying the H_2:CO_2 ratio and the pressure (up to 10 bar).

All methanation cases were simulated with a proprietary in-house code. A detailed literature mechanism was initially used and was then scaled to obtain good agreement at high pressures. Subsequently, a two-step methanation mechanism developed at PSI for atmospheric pressure was extended to provide good predictions at pressures up to 10 bar. Finally, a theoretical comparison of CO_2 methanation on Rh and Ni was performed and showed the superiority of Ni catalysts.

High-fidelity simulations were conducted using a Lattice Boltzmann (LB) solver to study the convection-diffusion-reaction processes inside and around catalytic porous particles used in methanation fluidized beds. A new catalytic LB model was developed, valid for arbitrary Damköhler numbers, for either equimolar or strongly non-equimolar reactions, and with the inclusion of velocity and concentration jumps (finite Knudsen number effects). The model was subsequently applied to a real porous particle whose geometry was reconstructed with the X-ray tomography images. The geometry of the porous particles and the numerical simulations indicated that the pore distribution is not spatially homogenous, in contrast to the common assumption used in up-scaled models. Finally, simulations were performed on spherical porous particles having an artificial macropore to evaluate the impact of spatial porosity inhomogeneity and Damköhler number.

Fields test with at transportable TRL 5 plant connected to a biogas plant allowed the extended testing of the operation window up to 10 bar and the part load behavior of the fluidized bed methanation reactor itself, but also within the interaction with the complete plant (comprising a membrane separation and a recycle) and the other units in the energy system such as electrolyzers and PV plants.

Important steps in the further development of fluidized bed methanation and the technology transfer to industry were achieved. The GanyMeth pilot plant (TRL 6) was successfully used for reactive experiments at up to 200 kW and confirmed the results of the TRL 4/5 plant, i.e. the technology can be scaled in a safe way. Within the European Union Project HyFuelUp, the industrial partner AlphaSYNT will design and build with support of PSI a 500 kW methanation unit to be integrated in a TRL 7 demonstrator in Portugal covering the value chain from low grade biomass via gasification, gas cleaning, methanation and liquefaction to Bio-LNG for heavy transport.

6 Outlook and next steps

GanyMeth campaign with simulated wood gas and hydrogen addition (PtG) will follow in near future. This activity, funded by SBFI within the European Union project HyFuelUp (www.hyfuelup.eu), will support the design of the reactor built by the industrial partner AlphaSYNT GmbH. Further, the generated concentration profiles will allow the validation of the macroscopic reactor model that was extended within the SOE funded activity reported above. Together with the pilot scale experiments, the collected know-how on different operation conditions and feed gas qualities represents a robust and reliable basis for the design and scale-up of fluidized bed methanation technology and thus strongly supports the market implementation together with the industrial partner.

Finally, the gained knowledge on fluidized bed reactors with vertical heat exchanger tubes can also be applied to other processes with endo- or exothermic reactions; for this however, specific additional research will be necessary.

7 National and international cooperation

With respect to the technology itself, intensive collaboration exists with the industrial partner AlphaSYNT GmbH, a Swiss SME. The involvement in the European Union project HyFuelUp also necessitates intensive discussion with the European partners in Portugal and Stuttgart to clarify the interfaces and to improve the process chain including the gas cleaning and gas upgrading to biomethane.

Further, in the Innosuisse Flagship project DeCIRRA, and to some extent in the SWEET project EDGE, we are in exchange with Swiss stakeholders and academic partners on the boundary conditions and the systemic aspects of applying such technologies.

8 Communication

Not applicable.

9 Publications

Scientific publications related to WP5 (SNSF-funded PhD Thesis Meysam Khatoonabadi)

1) **M. Khatoonabadi,** N. Prasianakis, J. Mantzaras, A pore-level 3D lattice Boltzmann simulation of mass transport and reaction in catalytic particles used for methane synthesis, *International Journal of Heat and Mass Transfer* 221, 125025, 2024.
https://doi.org/10.1016/j.ijheatmasstransfer.2023.125025

2) **M. Khatoonabadi,** N. Prasianakis, J. Mantzaras, Lattice Boltzmann modeling and simulation of velocity and concentration slip effects on the catalytic reaction rate of strongly non-equimolar reactions in microflows, *Physical Review E* 106, 065305, 2022.
https://journals.aps.org/pre/abstract/10.1103/PhysRevE.106.065305

3) **M. Khatoonabadi**, N. Prasianakis, J. Mantzaras, Lattice Boltzmann model with generalized wall boundary conditions for arbitrary catalytic reactivity, *Physical Review E* 103, 063303, 2021.
https://journals.aps.org/pre/abstract/10.1103/PhysRevE.103.063303

4) **M. Khatoonabadi,** M.A. Safi, N.I. Prasianakis, J. Roth, J. Mantzaras, N. Kirov, F. Buechi, Insights on the interaction of serpentine channels and gas diffusion layer in an operating polymer electrolyte fuel cell: numerical modeling across scales, *International Journal of Heat and Mass Transfer* 181, 121859, 2021.
https://doi.org/10.1016/j.ijheatmasstransfer.2021.121859

5) R. Sui, J. Mantzaras, R. Bombach, **M. Khatoonabadi**, High-pressure kinetic interactions between CO and H_2 during syngas catalytic combustion on PdO, *Proceedings of The Combustion Institute* 39, 5611–5619, 2023.
https://doi.org/10.1016/j.proci.2022.06.010

6) R. Sui, J. Mantzaras, C.K. Law, R. Bombach, **M. Khatoonabadi**, Homogeneous ignition of H_2/CO/O_2/N_2 mixtures over palladium at pressures up to 8 bar, *Proceedings Combustion Institute* 38, 6583-6591, 2021.
https://doi.org/10.1016/j.proci.2020.06.262

PhD Thesis:

M. Khatoonabadi, Three-dimensional lattice Boltzmann modeling and simulations of catalytic reactions, with applications to porous catalytic particles used for CO methanation, Dissertation No. 29499, ETH Zurich, 2023.
https://www.research-collection.ethz.ch/handle/20.500.11850/637847

Scientific publications related to WP2 and WP3 (main BfE work)

1) V.K. Arumugam, J. Mantzaras, A. Gantenbein, U. Doll, T. Schildhauer, Experimental and numerical investigation of high-pressure methane catalytic synthesis from H_2 and CO_2, *Proceedings of The Combustion Institute* 40, submitted 2023.

Scientific publications related to WP4 and WP7 (PhD Thesis Andreas Gantenbein)

1) **A. Gantenbein**, T.J. Schildhauer, Challenges in part load operation of biogas-based power-to-gas processes (part I), *Front. Energy Res*. 1049687, 2022.
https://doi.org/10.3389/fenrg.2022.1049687

2) **A. Gantenbein**, O. Kröcher, S.M.A. Biollaz and T.J. Schildhauer, Techno-economic evaluation of biological and fluidised-bed based methanation process chains for grid-ready biomethane production, *Front. Energy Res.* 775259, 2022.

https://doi.org/10.3389/fenrg.2021.775259

3) A. Gantenbein, J. Witte, S.M.A. Biollaz, O. Kröcher, T.J. Schildhauer. Flexible application of biogas upgrading membranes for hydrogen recycle in power-to-methane processes. *Chem. Eng. Sci.* 229 116012, 2020.
https://doi.org/10.1016/j.ces.2020.116012

PhD Thesis:

A. Gantenbein, Flexibilisation of Biogas-based Power-to-Gas Processes: A Techno-economic and Experimental Assessment (Thèse EPF Lausanne No° 10032, 2018-2022).
https://infoscience.epfl.ch/record/296480

10 References

[1] J. Kopyscinski, T.J. Schildhauer, S.M.A. Biollaz, Fluidized-bed methanation: interaction between kinetics and mass transfer, Ind. Eng. Chem. Res. 50 (2011) 2781-2790.
[2] J. Kopyscinski, T.J. Schildhauer, S.M.A. Biollaz, Methanation in a fluidized bed reactor with high initial CO partial pressure : Part II- Modeling and sensitivity study, Chem. Eng. Sci. 66 (2011) 1612-1621.
[3] J. Kopyscinski, T.J. Schildhauer, S.M.A. Biollaz, Methanation in a fluidized bed reactor with high initial CO partial pressure: Part I-Experimental investigation of hydrodynamics, mass transfer effects, and carbon deposition, Chem. Eng. Sci. 66 (2011) 924-934.
[4] M. Rudisuli, T.J. Schildhauer, S.M.A. Biollaz, J.R. van Ommen, Bubble characterization in a fluidized bed with vertical tubes, Ind. Eng. Chem. Res. 51 (2012) 4748-4758.
[5] V. Verma, T.W. Li, J.F. Dietiker, W.A. Rogers, Hydrodynamics of gas-solids flow in a bubbling fluidized bed with immersed vertical U-tube banks, Chem. Eng. J. 287 (2016) 727-743.
[6] J. Kopyscinski, T.J. Schildhauer, F. Vogel, S.M.A. Biollaz, A. Wokaun, Applying spatially resolved concentration and temperature measurements in a catalytic plate reactor for the kinetic study of CO methanation, J. Catal. 271 (2010) 262-279.
[7] R. Sui, E.T. Es-Sebbar, J. Mantzaras, R. Bombach, Homogeneous ignition during fuel-rich $H_2/O_2/N_2$ combustion in platinum-coated channels at elevated pressures, Combust. Flame 180 (2017) 184-195.
[8] J. Mantzaras, Progress in non-intrusive laser-based measurements of gas-phase thermoscalars and supporting modeling near catalytic interfaces, Prog. Energy Combust. Sci. 70 (2019) 169-211.
[9] S. Karagiannidis, J. Mantzaras, R. Bombach, S. Schenker, K. Boulouchos, Experimental and numerical investigation of the hetero-/homogeneous combustion of lean propane/air mixtures over platinum, Proc. Combust. Inst. 32 (2009) 1947-1955.
[10] M. Reinke, J. Mantzaras, R. Schaeren, R. Bombach, A. Inauen, S. Schenker, High-pressure catalytic combustion of methane over platinum: in situ experiments and detailed numerical predictions, Combust. Flame 136 (2004) 217-240.
[11] R. Sui, J. Mantzaras, R. Bombach, A. Denisov, Hetero-/homogeneous combustion of fuel-lean methane/oxygen/nitrogen mixtures over rhodium at pressures up to 12 bar, Proc. Combust. Inst. 36 (2017) 4321-4328.
[12] J. Mantzaras, R. Sui, C.K. Law, R. Bombach, Heterogeneous and homogeneous combustion of fuel-lean C3H8/O-2/N-2 mixtures over rhodium at pressures up to 6 bar, Proceedings of the Combustion Institute 38 (2021) 6473-6482.
[13] D. Schmider, L. Maier, O. Deutschmann, Reaction Kinetics of CO and CO_2 Methanation over Nickel, Ind. Eng. Chem. Res. 60 (2021) 5792-5805.
[14] R. Schwiedernoch, S. Tischer, C. Correa, O. Deutschmann, Experimental and numerical study on the transient behavior of partial oxidation of methane in a catalytic monolith, Chem. Eng. Sci. 58 (2003) 633-642.
[15] H.K. Moffat, R.J. Kee, J.F. Grcar, J.A. Miller, Surface PSR: A Fortran program for modeling well-stirred reactors with gas and surface reactions, Report No. SAND91-8001, Sandia National Laboratories, 1993.
[16] S. Arcidiacono, J. Mantzaras, I.V. Karlin, Lattice Boltzmann simulation of catalytic reactions, Phys. Rev. E 78 (2008) 046711.
[17] M. Khatoonabadi, N.I. Prasianakis, J. Mantzaras, Lattice Boltzmann model with generalized wall boundary conditions for arbitrary catalytic reactivity, Phys. Rev. E 103 (2021) 063303.
[18] M. Khatoonabadi, N.I. Prasianakis, J. Mantzaras, Lattice Boltzmann modeling and simulation of velocity and concentration slip effects on the catalytic reaction rate of strongly non-equimolar reactions in microflows, Phys. Rev. E in press (2022).
[19] M. Khatoonabadi, M.A. Safi, N.I. Prasianakis, J. Roth, J. Mantzaras, N. Kirov, F.N. Buchi, Insights on the interaction of serpentine channels and gas diffusion layer in an operating polymer electrolyte fuel cell: Numerical modeling across scales, Int. J. Heat Mass Transf. 181 (2021) 121859.

[20] M.E. Coltrin, R.J. Kee, F.M. Rupley, Surface Chemkin: A Fortran package for analyzing heterogeneous chemical kinetics at the solid surface-gas phase interface, Sandia National Laboratories, Report No. SAND90-8003C, 1996.
[21] R.J. Kee, G. Dixon-Lewis, J. Warnatz, M.E. Coltrin, J.A. Miller, A Fortran computer code package for the evaluation of gas-phase multicomponent transport properties, Sandia National Laboratories, Report No. SAND86-8246, 1996.
[22] J. Mantzaras, Progress in non-intrusive laser-based measurements of gas-phase thermoscalars and supporting modeling near catalytic interfaces, Prog. Energy Combust. Sci. 70 (2019) 169-211.
[23] J.H. Chiang, J.R. Hopper, Kinetics of the hydrogenation of carbon dioxide over supported nickel Ind. Eng. Chem. Prod. Res. Dev. 22 (1983) 225-228.
[24] J. Witte, J. Settino, S.M.A. Biollaz, T.J. Schildhauer, Direct catalytic methanation of biogas – Part I: New insights into biomethane production using rate-based modelling and detailed process analysis, Energy Conv. Manag. 171 (2018) 750-768.
[25] M. Khatoonabadi, N. Prasianakis, J. Mantzaras, A pore-level 3D lattice Boltzmann simulation of mass transport and reaction in catalytic particles used for methane synthesis, Int. J. Heat Mass Trans. 221 (2024) 125025.
[26] A. Gantenbein, T.J. Schildhauer, Challenges in part load operation of biogas-based power-to-gas processes (part I), Front. Energy Res (2022) 1049687
[27] A. Gantenbein, O. Kröcher, S.M.A. Biollaz and T.J. Schildhauer, Techno-economic evaluation of biological and fluidised-bed based methanation process chains for grid-ready biomethane production, Front. Energy Res. (2022) 775259.
[28] A. Gantenbein, J. Witte, S.M.A. Biollaz, O. Kröcher, T.J. Schildhauer. Flexible application of biogas upgrading membranes for hydrogen recycle in power-to-methane processes. Chem. Eng. Sci. 229 (2020) 116012.